

<b>REPORT DOCUMENTATION PAGE</b>			Form Approved OMB NO. 0704-0188		
<p>The public reporting burden for this collection of information is estimated to average 1 hour per response, including the time for reviewing instructions, searching existing data sources, gathering and maintaining the data needed, and completing and reviewing the collection of information. Send comments regarding this burden estimate or any other aspect of this collection of information, including suggestions for reducing this burden, to Washington Headquarters Services, Directorate for Information Operations and Reports, 1215 Jefferson Davis Highway, Suite 1204, Arlington VA, 22202-4302. Respondents should be aware that notwithstanding any other provision of law, no person shall be subject to any penalty for failing to comply with a collection of information if it does not display a currently valid OMB control number.</p> <p>PLEASE DO NOT RETURN YOUR FORM TO THE ABOVE ADDRESS.</p>					
1. REPORT DATE (DD-MM-YYYY) 13-05-2015		2. REPORT TYPE Final Report		3. DATES COVERED (From - To) 16-May-2011 - 31-Dec-2014	
4. TITLE AND SUBTITLE Final Report: Hypersonic Transition Along Curved Surfaces In The Presence Of Vortices And Their Control By Using Microtextured Surfaces			5a. CONTRACT NUMBER W911NF-11-1-0161		
			5b. GRANT NUMBER		
			5c. PROGRAM ELEMENT NUMBER 206022		
6. AUTHORS Charles Maldarelli			5d. PROJECT NUMBER		
			5e. TASK NUMBER		
			5f. WORK UNIT NUMBER		
7. PERFORMING ORGANIZATION NAMES AND ADDRESSES Research Foundation CUNY - The City Col 160 Convent Avenue  New York, NY 10031 -9101			8. PERFORMING ORGANIZATION REPORT NUMBER		
9. SPONSORING/MONITORING AGENCY NAME(S) AND ADDRESS (ES) U.S. Army Research Office P.O. Box 12211 Research Triangle Park, NC 27709-2211			10. SPONSOR/MONITOR'S ACRONYM(S) ARO		
			11. SPONSOR/MONITOR'S REPORT NUMBER(S) 58975-EG-REP.14		
12. DISTRIBUTION AVAILABILITY STATEMENT Approved for Public Release; Distribution Unlimited					
13. SUPPLEMENTARY NOTES The views, opinions and/or findings contained in this report are those of the author(s) and should not be construed as an official Department of the Army position, policy or decision, unless so designated by other documentation.					
14. ABSTRACT The hydrodynamics and applications of fluid flow over microtextured surfaces was studied: 1. The motion of a water droplet over a surface comprised of an array of hydrophobic microposts was examined. Water droplets do not penetrate into the texture, but glide over it, resulting in reduced friction and allowing the drops to collect contaminants so that the interface is self-cleaning. 2. The movement of water droplets immersed in oil along a surface microtextured with nanometer-sized hydrophobic particles was examined. The oil impregnates into the particle texture, and water droplets glide over the					
15. SUBJECT TERMS microtextured surfaces, hydrodynamic flow, slip, superhydrophobicity					
16. SECURITY CLASSIFICATION OF:			17. LIMITATION OF ABSTRACT UU	15. NUMBER OF PAGES	19a. NAME OF RESPONSIBLE PERSON Charles Maldarelli
a. REPORT UU	b. ABSTRACT UU	c. THIS PAGE UU			19b. TELEPHONE NUMBER 212-650-8160



## Report Title

Final Report: Hypersonic Transition Along Curved Surfaces In The Presence Of Vortices And Their Control By Using Microtextured Surfaces

### ABSTRACT

The hydrodynamics and applications of fluid flow over microtextured surfaces was studied:

1. The motion of a water droplet over a surface comprised of an array of hydrophobic microposts was examined. Water droplets do not penetrate into the texture, but glide over it, resulting in reduced friction and allowing the drops to collect contaminants so that the interface is self-cleaning.
2. The movement of water droplets immersed in oil along a surface microtextured with nanometer-sized hydrophobic particles was examined. The oil impregnates into the particle texture, and water droplets glide over the texture without becoming stuck, allowing resistance to corrosion.
3. The movement of an oil phase over a hydrophobic elastomeric polymer with high air solubility was studied, and slip, resulting in reduced drag at the oil/elastomer surface was measured by observing the motion of water droplets driven by electrical forces.
4. A microtextured surface consisting of an array of traps was constructed in a microfluidic cell to entrap and array microbeads in the cell as a prototype chip for screening biomolecular interactions.
5. In a technology transfer, the fluidics of electrically driven droplet motions is being adopted by ExxonMobil to study coalescence of water droplets in crude oil.

---

**Enter List of papers submitted or published that acknowledge ARO support from the start of the project to the date of this printing. List the papers, including journal references, in the following categories:**

**(a) Papers published in peer-reviewed journals (N/A for none)**

Received

Paper

01/02/2014	6.00	Xiaoxiao Chen, Shahab Shojaei-Zadeh, M. Lane Gilchrist, Charles Maldarelli. A lipobead microarray assembled by particle entrapment in a microfluidic obstacle course and used for the display of cell membrane receptors, Lab on a Chip, (07 2013): 0. doi: 10.1039/c3lc50083g
05/13/2015	13.00	Thomas F. Leary, Setareh Manafirasi, Charles Maldarelli. Mass transfer in the biomolecular binding of a target against probe molecules on the surface of microbeads sequestered in wells in a microfluidic cell, Lab Chip, (01 2015): 0. doi: 10.1039/C4LC01185F

**TOTAL: 2**

**Number of Papers published in peer-reviewed journals:**

---

**(b) Papers published in non-peer-reviewed journals (N/A for none)**

Received

Paper

**TOTAL:**

Number of Papers published in non peer-reviewed journals:

---

(c) Presentations

Enhanced Mass Transfer in the Capture of Targets to a Probe Library Consisting of Microbeads with Surface Capture Molecules and Confined in Wells at the Channel Floor of a Microfluidic Cell, Manafirasi, S. (speaker) , Leary, T. and Maldarelli, C., AIChE Annual Meeting, Nov., 2014

Number of Presentations: 1.00

---

Non Peer-Reviewed Conference Proceeding publications (other than abstracts):

<u>Received</u>	<u>Paper</u>
-----------------	--------------

TOTAL:

Number of Non Peer-Reviewed Conference Proceeding publications (other than abstracts):

---

Peer-Reviewed Conference Proceeding publications (other than abstracts):

<u>Received</u>	<u>Paper</u>
-----------------	--------------

TOTAL:

**Number of Peer-Reviewed Conference Proceeding publications (other than abstracts):**

---

**(d) Manuscripts**

<u>Received</u>	<u>Paper</u>
01/02/2014	8.00 Thomas Leary, Mohsen Yeganeh, Charles Maldarelli. Micron-size Hydrodynamic Slip at an Oil/Polydimethyl Siloxane Surface From Measurements of the Dielectrophoretic Motion of Water Droplets Along the Surface, PHYSICAL REVIEW LETTERS (08 2013)
08/30/2012	2.00 Thomas Leary , Charles Maldarelli, Mohsen Yeganeh. The Hydrodynamics of the Pairwise Dielectrophoretic Coalescence of Droplets in a Confining Microfluidic Channel, Physical Review Letters (08 2012)
08/30/2012	3.00 Shahab Shojaei-Zadeh, Charles Maldarelli. Microbead Arrays Assembled by Entrapment in a Microfluidics Obstacle Course, Physics of Fluids A (07 2012)
08/30/2012	5.00 Nikhil S. Bhole, Charles Maldarelli. Theory and Experiment on the Microhydrodynamics of Droplet Spreading on Superhydrophobic Surfaces, Journal of Fluid Mechanics (09 2012)
10/12/2014	11.00 Thomas F. Leary, Mohsen Yeganeh, Charles Maldarelli. Electrocoalescence of Water-in-Cude Oil Emulsions in Two Dimensions, Applied Physics Letters (07 2014)
10/12/2014	10.00 Xiaoxiao Chen, Setareh Manafi, Thomas F. Leary, M. Lane Gilchrist, Charles Maldarelli. Microfluidic Bead Array Libraries for Screening Biomolecular Binding Interactions, JOVE (08 2014)
10/12/2014	12.00 Xiaoxiao Chen, Thomas F. Leary, Charles Maldarelli. Mass Transfer of a Target to a Library of Probe Molecules Hosted on the Surface of Microbeads Arrayed in a Trapping Course in a Microfluidic Cell, Biomicrofluidics (08 2014)
<b>TOTAL:</b>	<b>7</b>

**Number of Manuscripts:**

---

**Books**

<u>Received</u>	<u>Book</u>
-----------------	-------------

**TOTAL:**

Received

Book Chapter

**TOTAL:**

---

**Patents Submitted**

---

**Patents Awarded**

---

**Awards**

---

**Graduate Students**

<u>NAME</u>	<u>PERCENT SUPPORTED</u>	Discipline
Setareh Manafirasi	1.00	
<b>FTE Equivalent:</b>	<b>1.00</b>	
<b>Total Number:</b>	<b>1</b>	

---

**Names of Post Doctorates**

<u>NAME</u>	<u>PERCENT SUPPORTED</u>
<b>FTE Equivalent:</b>	
<b>Total Number:</b>	

---

**Names of Faculty Supported**

<u>NAME</u>	<u>PERCENT SUPPORTED</u>
<b>FTE Equivalent:</b>	
<b>Total Number:</b>	

---

**Names of Under Graduate students supported**

<u>NAME</u>	<u>PERCENT SUPPORTED</u>	Discipline
Shelley Lim	1.00	High School
Ellie Buellesbach	1.00	High School
<b>FTE Equivalent:</b>	<b>2.00</b>	
<b>Total Number:</b>	<b>2</b>	

### Student Metrics

This section only applies to graduating undergraduates supported by this agreement in this reporting period

The number of undergraduates funded by this agreement who graduated during this period: ..... 0.00

The number of undergraduates funded by this agreement who graduated during this period with a degree in science, mathematics, engineering, or technology fields:..... 0.00

The number of undergraduates funded by your agreement who graduated during this period and will continue to pursue a graduate or Ph.D. degree in science, mathematics, engineering, or technology fields:..... 0.00

Number of graduating undergraduates who achieved a 3.5 GPA to 4.0 (4.0 max scale):..... 0.00

Number of graduating undergraduates funded by a DoD funded Center of Excellence grant for Education, Research and Engineering:..... 0.00

The number of undergraduates funded by your agreement who graduated during this period and intend to work for the Department of Defense ..... 0.00

The number of undergraduates funded by your agreement who graduated during this period and will receive scholarships or fellowships for further studies in science, mathematics, engineering or technology fields:..... 0.00

### Names of Personnel receiving masters degrees

NAME

**Total Number:**

### Names of personnel receiving PHDs

NAME

**Total Number:**

### Names of other research staff

NAME

PERCENT SUPPORTED

**FTE Equivalent:**

**Total Number:**

### Sub Contractors (DD882)

### Inventions (DD882)

### Scientific Progress

see attachment

## Technology Transfer

This research on microtextures has drawn the interest of ExxonMobil Research and Engineering Company in Clinton NJ, and we have together developed a microfluidic chip to study the process of electrocoalescence of water droplets in a crude oil. In the electrocoalescence process, an electric field is applied across an emulsion of water droplets in oil. The field polarizes the conducting water droplets in the insulating oil, creating dipole-dipole attractive forces which coalesce the droplets. This coalescence is used in the oil industry to remove water droplets from the oil. The microfluidic cell that was designed uses flow focusing to create a monodisperse emulsion of the droplets in an oil chamber in a transparent cell, and follows the electrocoalescence process visually, through optical microscopy in the chamber as a field is applied across the droplets by electrodes placed on opposite ends of the chamber. The microfluidic design allows a visual picture of the electrocoalescence process through the normally opaque crude oil because the height of the microfluidic chamber is small, of order 100 microns, and the monodisperse size distribution allows for a reproducible study. A model is constructed for the coalescence process, which solves the electrostatic field equations in the emulsion, to compute the instantaneous dipolar forces between the droplets. This computation is done directly on the configuration of the droplets in the emulsion as obtained from the optical micrographs. From a map of these forces, evaluated on a pairwise basis, predictions are made as to which droplets coalesce based on whether the force is attractive (relative alignment of the droplets along the field) or repulsive (side alignment relative to the field), and these predictions are shown to agree with the observed coalescence process. The cell can be used to identify field strength conditions necessary to electrocoalesce the water droplets in a particular crude, and to identify surfactant promoters for the particular crude which can accelerate the process. This research is described in the last chapter of the detailed progress report which is attached. ?



**Hydrodynamic Flow Over Microtextured  
Surfaces  
Final Report  
Agreement Number W911NF1110161**

**Charles Maldarelli**

Department of Chemical Engineering and  
Benjamin Levich Institute of Physicochemical Hydrodynamics,  
The City College of New York

May 13, 2015

# Contents

<b>1</b>	<b>Introduction</b>	<b>3</b>
1.1	Scope of Proposed Research . . . . .	3
1.2	Summary of Research . . . . .	5
<b>2</b>	<b>Hydrodynamics of Water Droplet Movement in Air Over Superhydrophobic Post Microtextures For Self-Cleaning</b>	<b>12</b>
2.1	Background . . . . .	12
2.2	Research Objectives . . . . .	16
2.3	Model Formulation . . . . .	19
2.3.1	Singularity at the contact point and slip velocity . . . . .	19
2.4	Numerical Solution . . . . .	21
2.4.1	Biharmonic Boundary Integral Method . . . . .	21
2.4.2	Implementation of Boundary Integral Method . . . . .	23
2.4.3	Code Validation . . . . .	26
2.5	Numerical Results and Discussion . . . . .	28
2.5.1	Static equilibrium shapes . . . . .	29
2.5.2	Spreading dynamics over a planar surface . . . . .	30
2.5.3	Spreading dynamics over topography . . . . .	33
2.6	Experimental Studies . . . . .	39
2.6.1	Microfabrication and Static Contact Angle Measurements . . . . .	41
2.6.2	Contact Angle Measurements . . . . .	45
2.6.3	Experimental Results of Droplet Spreading over a Superhydrophobic Surface . . . . .	47
2.7	Conclusion . . . . .	53
<b>3</b>	<b>Hydrodynamics of Water Droplet Movement in Oil over Particle Microtextures Impregnated With Oil to Reduce Droplet Adhesion</b>	<b>55</b>
3.1	Background . . . . .	55

3.2	Microtexture Fabrication Using Nanoparticles . . . . .	59
3.3	Equilibrium Contact Angles in Air and Under Oil . . . . .	60
<b>4</b>	<b>Hydrodynamics of Large Interfacial Slip at Porous (Air-Permeable) Polymer Surfaces For Drag Reduction</b>	<b>62</b>
4.1	Introduction . . . . .	62
4.2	Experimental Measurement of Droplet Approach . . . . .	64
4.3	Finite Element Simulations of the Droplet Hydrodynamics . . . . .	67
4.4	Conclusions . . . . .	69
4.5	Appendix A: Materials and Cell Fabrication . . . . .	71
4.6	Appendix B: Interpolating Functions and Validation Simulations of the Finite Element Calculations . . . . .	72
<b>5</b>	<b>Hydrodynamic Capture of Microbeads in Microtexture Obstacle Courses for Biomolecular Screening in Pathogen Sensing and Point of Care Diagnostics</b>	<b>74</b>
5.1	Introduction . . . . .	74
5.2	Hydrodynamic and Mass Transfer Numerical Simulations . . . . .	80
5.2.1	Formulation . . . . .	80
5.2.2	Hydrodynamic Flow Simulations . . . . .	84
5.2.3	Mass Transfer Simulations . . . . .	86
5.3	Experimental Binding Assay . . . . .	94
5.3.1	Materials and Methods . . . . .	94
5.3.2	Microbead Functionalization . . . . .	95
5.3.3	Device Design and Fabrication . . . . .	96
5.3.4	Microbead Arraying . . . . .	97
5.3.5	Screening Assay and Fluorescence Imaging of NeutrAvidin-FITC Binding to the Biotinylated Microbeads . . . . .	98
5.3.6	Comparison with Simulations . . . . .	100
5.3.7	Summary and Conclusions . . . . .	101
<b>6</b>	<b>Electrocoalescence of Water-in-Crude Oil Emulsions in Two Dimensions</b>	<b>105</b>
6.1	Introduction and Background . . . . .	105
6.2	Experimental . . . . .	107
6.3	Theoretical . . . . .	108
	<b>Bibliography</b>	<b>134</b>

# Chapter 1

## Introduction

### 1.1 Scope of Proposed Research

The overall goal of this research program is to study experimentally and theoretically the hydrodynamics of fluid flow along *microtextured* surfaces. In the context of this research, microtextured surfaces are broadly defined as interfaces with topological features of characteristic size of the order of hundreds of nanometers to tens of microns. The features in general are spatially distributed along the surface in either an irregular or organized pattern, and can be fabricated from hard or elastomeric (soft) materials. When fluid flows over a microtextured surface, the flow within the texture can dramatically affect the hydrodynamics above the surface relative to the case in which the surface is smooth, and as such can lead to innovative applications of interest to the Department of Defense (DOD).

The research proposal was originally submitted to the Air Force Office of Scientific Research (AFOSR) under a announcement for historically black colleges and universities and minority serving institutions (HDCU/MI) and with Professor Charles Maldarelli of the City College of the City University of New York (CCNY-CUNY, a HBCU/MI) as PI and Professor Philip Hall of Imperial College London as co-PI. The research program outlined in the proposal consisted of two parts: The first, under the direction of the PI with expertise in materials fabrication and microfluidics, proposed fabricating textured surfaces with a regular pillar (post) pattern using lithographic techniques, and soft elastomeric materials (soft photolithography), imaging the flow through the post array with particle image velocimetry, measuring flow parameters such as permeability through the surface with the surfaces assembled in microfluidic flow cells, and computational modeling the flow within and above the surface. The second, under the direction of the co-PI with expertise in theoretical hypersonics, examined the application of these surfaces as passive control elements to delay the transition to turbulence in the near wall laminar boundary layers of aerospace vehicles

in low hypersonic flow. Hypersonic boundary layer solutions for the flow over the surface were to be coupled to the flow solutions in the microtextures layer to examine the effect of the flow in the texture on altering surface vortices and the transition to turbulence. Upon the terms of the award of the grant (May, 2011), a three year effort, the proposal was moved to the Fluid Dynamics Program at the Army Research Office (ARO), and the support of the Co-PI was disallowed as the effort was intended to be focused at the HBCU/MI institution. In consultation with the ARO program manager (including a site visit in May 2012), in addition to the fabrication of the microtextures, and the study of their hydrodynamics, the application of the textured surfaces was directed to the following slower flow regimes of interest to the ARO:

1. Hydrodynamics of Water Droplet Movement in Air Over Superhydrophobic Micropost Textures For Self-Cleaning
2. Hydrodynamics of Water Droplet Movement in Oil over Particle Microtextures Impregnated With Oil For Reduced Droplet Adhesion
3. Hydrodynamics of Large Interfacial Slip at Porous (Air-Permeable) Polymer Surfaces For Drag Reduction
4. Hydrodynamic Capture of Microbeads in Microtexture Obstacle Courses for Biomolecular Screening in Pathogen Sensing and Point of Care Diagnostics

The research on these topics was undertaken for three and one/half years, and concluded in December of 2014, involving four graduate students (two fully supported by the research and two partially supported), two master's students (not supported by this grant), two undergraduates and two high school students supported by funds supplemented to the grant by the UA/HSAP program. Part of the research work on the use of dielectrophoretic forces to measure slip over a polymer surface in a polymer surface has been utilized at the ExxonMobil Research and Engineering Company (EMRE) in Annandale, New Jersey to study the process of electrocoalescence of droplets in an oil phase. This technology transfer arose as one of the graduate students participating in the ARO effort interned at ExxonMobil, and a collaborative study was undertaken.

This report is organized as follows. In the remainder of this Introduction, a brief summary is given on the results on each of the major topics studied, along with a report on the work on the technology transfer. The next five chapters describe the research on the hydrodynamics water droplet motion over superhydrophobic microtextures in air (Chapter 2), under oil (Chapter 3), large interfacial slip over porous polymer surfaces (Chapter 4), bead

array obstacle courses for biomolecular screening (Chapter 5), and the measurement of electrocoalescence of water droplets in oil in a microfluidic cell collaboration with ExxonMobil (Chapter 6).

## 1.2 Summary of Research

A brief summary of the results on each of the above topics, and a report on the technology transfer is provided below.

---

### HYDRODYNAMICS OF WATER DROPLET MOVEMENT IN AIR OVER SUPERHYDROPHOBIC MICROPOST TEXTURES FOR SELF-CLEANING

“Superhydrophobic” surfaces are microtextured, hydrophobic interfaces which do not allow water to penetrate into the texture. Water droplets easily glide over the texture since the liquid rides over a cushion of air in the texture. Contaminant particles on the “superhydrophobic” surface can be removed from the surface by the gliding motion of

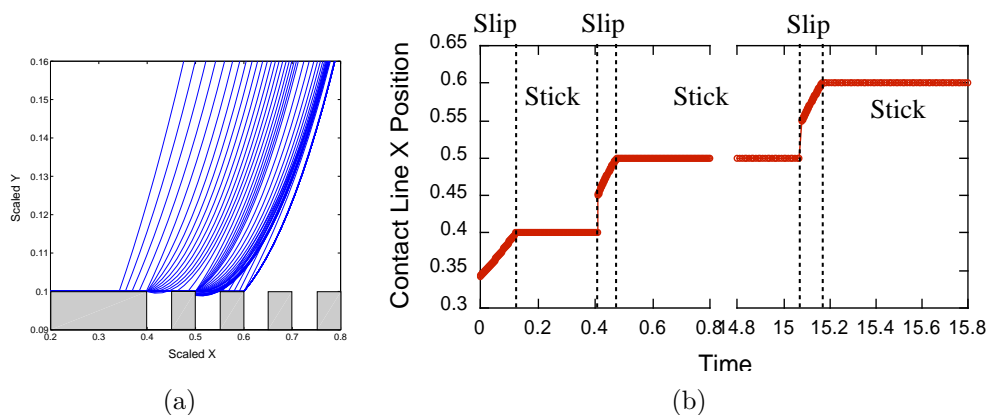


Figure 1.1: Droplet spreading dynamics over a topography composed of solid width = 0.05 and gap = 0.05 (relative to the drop radius) for advancing contact angle of  $90^\circ$ . (a) Time evolution of the droplet shape near the contact line region. Droplet achieves a final equilibrium shape at the pinning point located at  $X = 0.6$ . (b) Left hand side plot shows slip-stick-jump motion of the contact line, contact line slips on the horizontal surface, sticks after reaching the corner point and jumps from one pillar to the next. Corresponding dynamic contact angles are plotted on the right.

droplets as they pick-up the particles and remove them from the surface. To understand this motion, hydrodynamic solutions were obtained for the two dimensional spreading of a droplet over a microtextured surface consisting of a line of posts, as a model of a self-cleaning, superhydrophobic surface. The droplet is found to execute a slip-stick motion in which it

moves quickly over the tops of the pillars, but sticks at the edges of the pillar before jumping to the next pillar (Fig. 1.1). Time-lapse videos for forced movement of droplets placed on and moving over a two dimensional grooved surface fabricated by soft lithography confirmed this motion (Fig. 1.2).

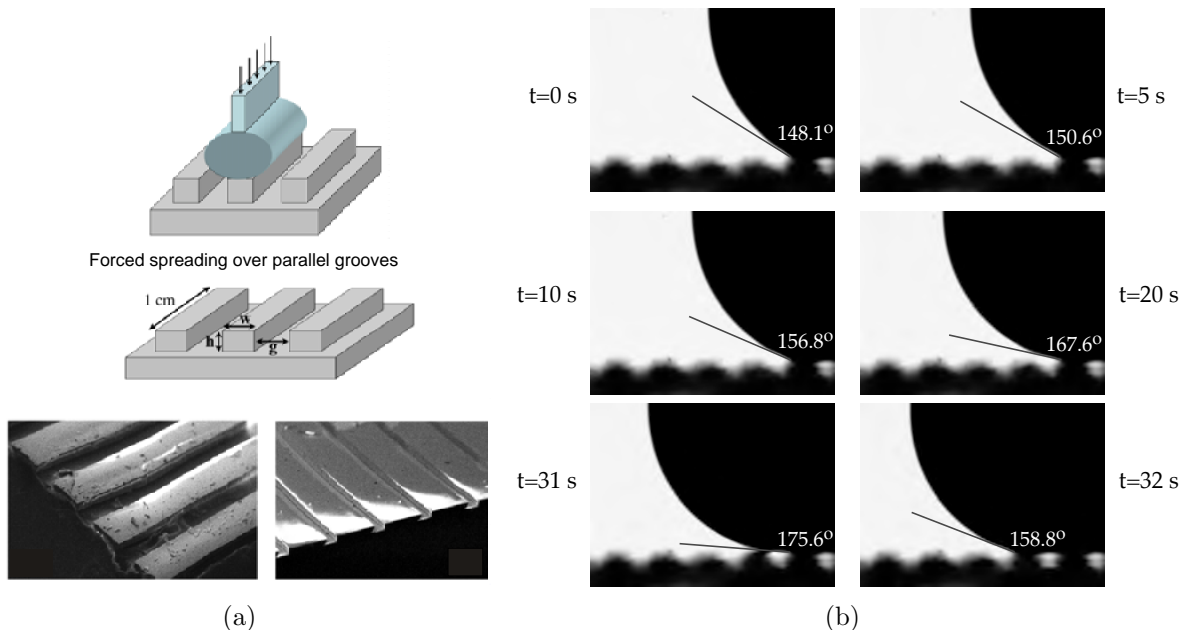


Figure 1.2: (a) 2-D anisotropic parallel grooved/stripped surfaces with width  $w$  of  $175 \mu\text{m}$  and  $375 \mu\text{m}$  respectively.  $g = 125 \mu\text{m}$  and  $h = 100 \mu\text{m}$  in both cases. (b) Controlled spreading of a 2-D droplet over a striped surface with  $w = 175 \mu\text{m}$ ,  $g = 125 \mu\text{m}$  and  $h = 100 \mu\text{m}$ . Flow rate through the slit =  $10 \mu\text{l/min}$ , frame capture rate = 1 frame/sec. Droplet shows pinning at the corner point while its contact angle increases till time  $t=31 \text{ sec}$  at which time the contact line jumps to the next pillar

---

## HYDRODYNAMICS OF WATER DROPLET MOVEMENT IN OIL OVER PARTICLE MICROTEXTURES IMPREGNATED WITH OIL FOR REDUCED DROPLET ADHESION

We have developed microtextured, hydrophobic surfaces which, when immersed in oil, allow water droplets to glide over the surface without sticking. The textured surfaces are constructed coating a nanoparticle/polymer resin suspension on a flat surface and curing the resin, which is scalable to texturizing large surface areas. The textures are functionalized to be very hydrophobic so that the oil saturates the texture. Water droplets under oil which become attached to the surface are nonadhesive in that they subtend large contact angles on the surface, and slide easily along the surface over a cushion of the saturating oil. We have measured static contact angles on these microtextured surfaces constructed from colloiddally which demonstrate that water droplets under oil on these surfaces retain large contact angles.

Water droplets drawn over the surface by gravity are observed to move with high mobility as the contact angle hysteresis is reduced. These surfaces address a longstanding problem of how to prohibit water droplets from sticking on surfaces under oils. Adhered droplets are the nucleating sites for corrosion and fouling in many applications involving oils on surfaces, and treatment with these microtextures can represent a means for maintaining water-droplet free surfaces under oil.

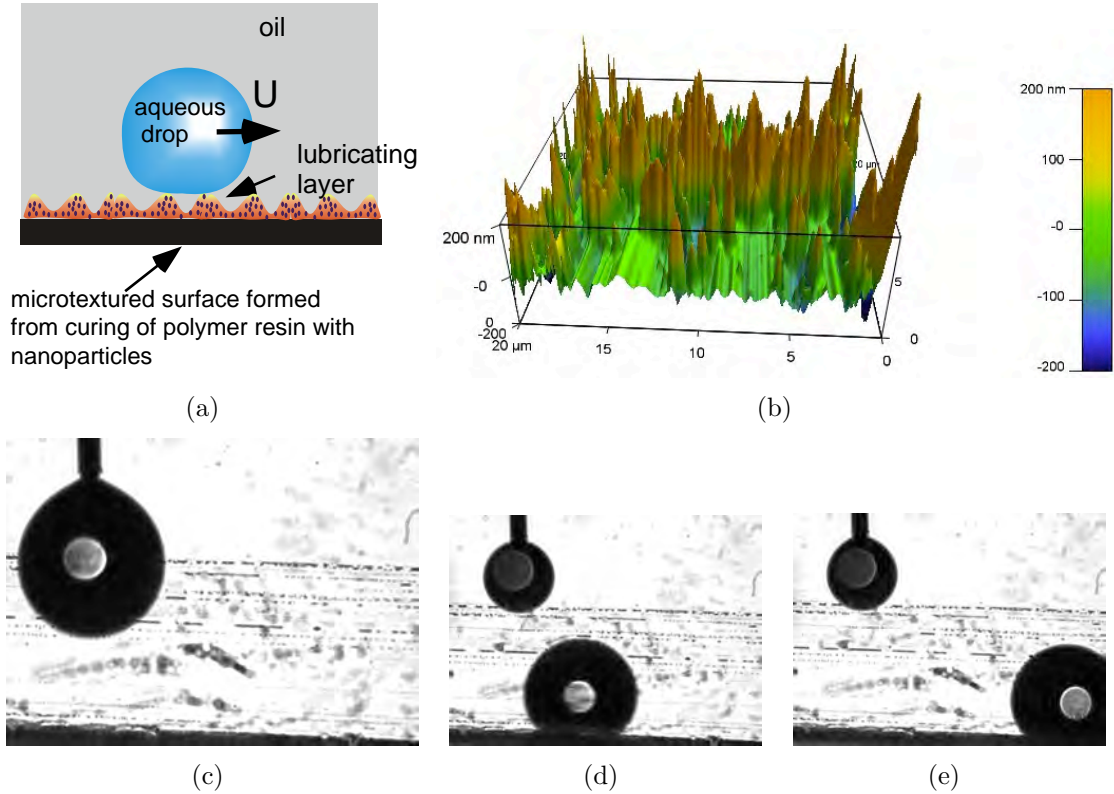


Figure 1.3: (a) A mixture of nanoparticles and binder cures to form a microtextured surface (b) Atomic force microscopy image of the particle surface in tapping mode. (c)-(e) A water droplet released onto the particle textured surface under oil glides over the surface

---

## HYDRODYNAMICS OF LARGE INTERFACIAL SLIP AT POROUS (AIR-PERMEABLE) POLYMER SURFACES FOR DRAG REDUCTION

Measurements are reported of “giant” hydrodynamic slip of the order of one micron at the interface between a viscous mineral oil and the elastomer polydimethylsiloxane (PDMS). The surface slip is quantified by a new, novel technique in which a train of monodispersely-sized aqueous droplets, approximately 100 microns in diameter, are formed in oil by flow



focusing, and are streamed through a wide microfluidic channel with a height only slightly larger than the droplets. The channel material is PDMS, as fabricated by molding over a lithography manufactured master. The droplets, heavier than the mineral oil, descend to the bottom channel wall. At a downstream location, a uniform electric field is applied in the flow direction to separated pairs of droplets, forcing the droplets towards each by a dielectrophoretic force, and the relative droplet velocity is measured by optical microscopy. The drag of the droplets against the channel floor (along with the droplet-droplet interaction) determines the relative velocity, and this drag is affected by the slip of the intervening oil film along the bottom surface of the channel. The distance between the wall and the droplet is determined from the transit time of the droplets to the point of application of the field. Measurements of the velocity are compared to finite element hydrodynamic solutions for the approach velocity to determine the wall slip coefficient. The large slip at the PDMS surface suggests that the air retained in PDMS because of its nanoporous hydrophobicity leads to a low friction layer of nanobubbles at the interface, and this represents a general means for generating large slip without (superhydrophobic) surface microtexturing. These results are particularly relevant to microfluidics where PDMS is the standard material, and the use of oil streams with reagent water droplets have become a dominant lab on a chip platforms.

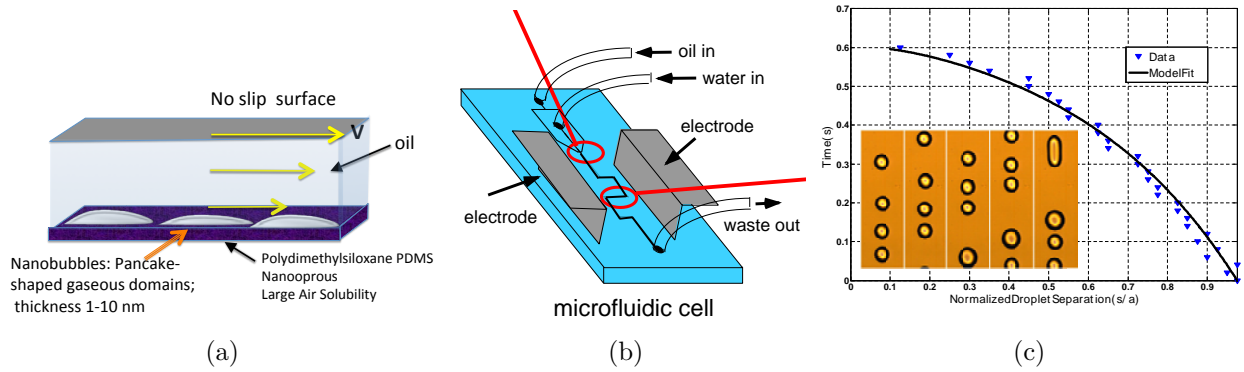


Figure 1.4: (a) Pancake-shaped air bubbles form at the oil/polydimethylsiloxane interface because of the large air solubility of PDMS (b) Flow-focusing produces a train of water droplets in oil (c) Application of an electric field parallel to the train creates a dielectrophoretic force which causes the droplets to merge and the slip on the surface to be measured.

## HYDRODYNAMIC CAPTURE OF MICROBEADS IN MICROTTEXTURE OBSTACLE COURSES FOR BIOMOLECULAR SCREENING IN PATHOGEN SENSING AND POINT OF CARE DIAGNOSTICS

We have constructed (Fig. 1.6(a)) a microtextured surface consisting of traps (“V” shaped open enclosures), integrated as the bottom surface of a microfluidic cell, to array

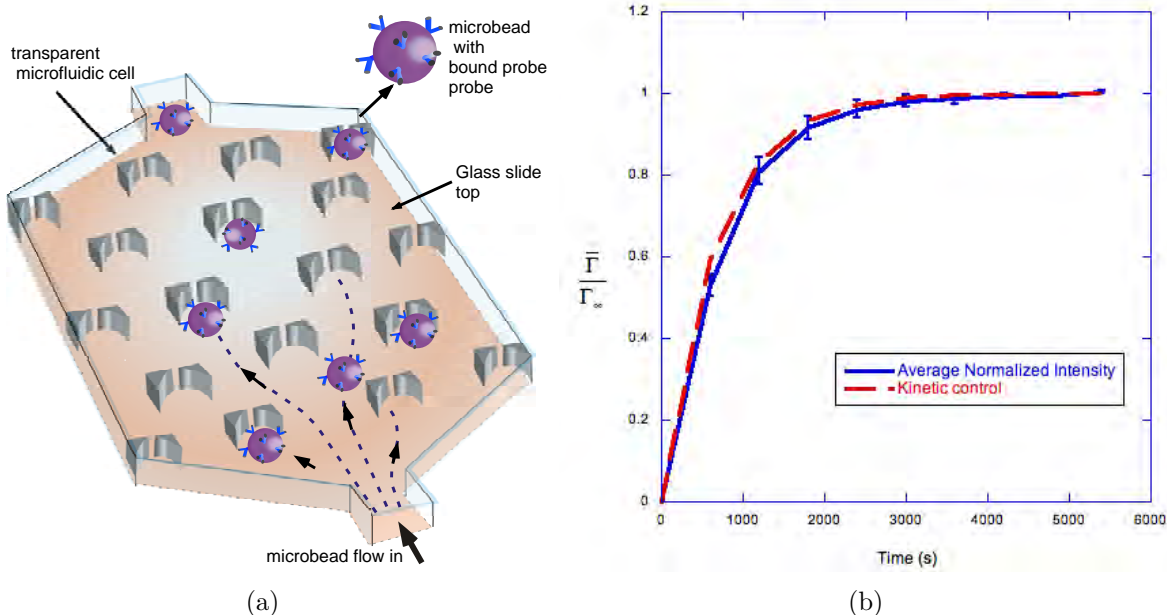


Figure 1.5: (a) Microbeads hosting surface probes arrayed in a microtexture of traps for screening biomolecular binding interactions. (b) A comparison of simulation data with experiment data for the dynamic response of the microbead array. The blue solid line with error bars shows the normalized intensity of the fluorescence of NeutrAvidin-FITC bound to 0.1 mol % NHS-PEG<sub>4</sub>-Biotin microbeads as a function of time for a solution concentration of 500 ng/ml and a flow rate of 100  $\mu\text{l}/\text{min}$ . The red line shows the simulation fit, for a value of  $k_a = 180 \text{ m}^3 \text{ mole}^{-1} \text{ sec}^{-1}$ , and the kinetic limit (red) overlies the finite element simulation.

microbeads, and demonstrated the use of the cell as a device for screening the binding interactions of a “target” biomolecule against a library of “probe” molecules. Sets of microbeads, with each set displaying a probe molecule attached to its surface, are streamed through the cell sequentially and entrapped by the microtextured surface to form the probe library. The screening step is undertaken by flowing an analyte target through the cell and over the microbeads, and identifying microbeads which bind the target, usually by fluorescently labelling the target and scanning for luminescent microbeads. The hydrodynamic flow of analyte through the microtexture is solved, and the solutions are used to simulate the mass transfer of the target to the microbead surface. Experiments are also undertaken using the binding of a target, fluorescently labeled NeutrAvidin, to its binding partner biotin, displayed on the microbead surface, to illustrate the use of the device as a screening tool (Fig. 1.6(b)).

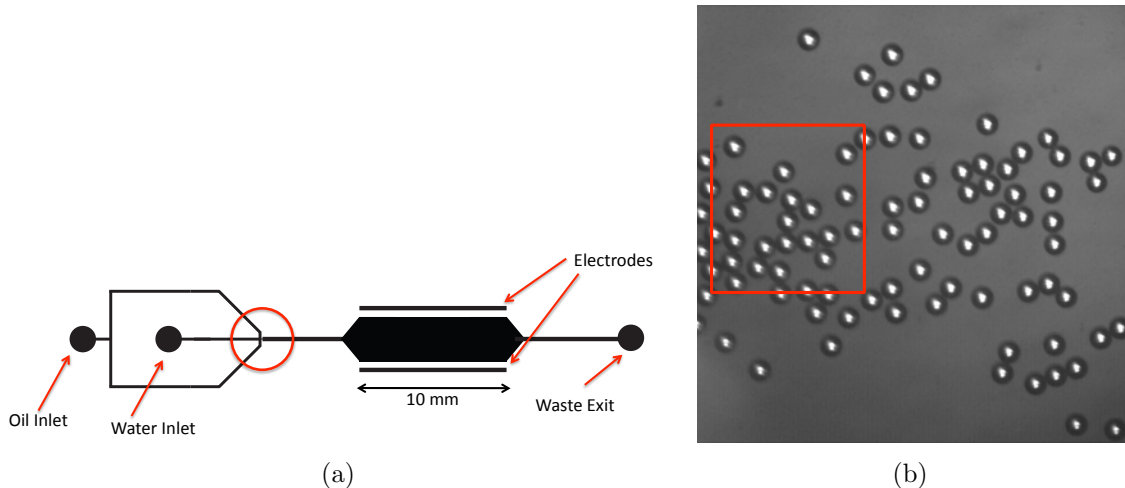


Figure 1.6: (a) Schematic of the microfluidic cell used to study electrocoalescence, and (b) a dispersion of monodisperse droplets of water in a crude oil.

---

#### ELECTROCOALESCENCE OF WATER-IN-CRUDE OIL EMULSIONS IN TWO DIMENSIONS: TECHNOLOGY TRANSFER WITH EXXONMOBIL

This study reports on the technology transfer on the research of this proposal with Exxon-Mobil. Using the microfluidic flow studies of Chapter 4 on dielectrophoretic coalescence of drops, we have examined the electrocoalescence of water droplets in crude oils using microfluidics. In the electrocoalescence process, an electric field is applied across an emulsion of water droplets in oil. The field polarizes the conducting water droplets in the insulating oil, creating dipole-dipole attractive forces which coalesce the droplets. This coalescence is used in the oil industry to remove water droplets from the oil. The microfluidic cell that was designed uses flow focusing to create a monodisperse emulsion of the droplets in an oil chamber in a transparent cell, and follows the electrocoalescence process visually, through optical microscopy in the chamber as a field is applied across the droplets by electrodes placed on opposite ends of

the chamber. The microfluidic design allows a visual picture of the electrocoalescence process through the normally opaque crude oil because the height of the microfluidic chamber is small, of order  $100\ \mu\text{m}$ , and the monodisperse size distribution allows for a reproducible study. A model is constructed for the coalescence process, which solves the electrostatic field equations in the emulsion, to compute the instantaneous dipolar forces between the droplets. This computation is done directly on the configuration of the droplets in the emulsion as obtained from the optical micrographs. From a map of these forces, evaluated on a pairwise basis, predictions are made as to which droplets coalesce based on whether the force is

attractive (relative alignment of the droplets along the field) or repulsive (side alignment relative to the field), and these predictions are shown to agree with the observed coalescence process (Fig. 1.6).

## Chapter 2

# Hydrodynamics of Water Droplet Movement in Air Over Superhydrophobic Post Microtextures For Self-Cleaning

### 2.1 Background

A microtextured interface presents topological features of elevations and depressions with length scales of the order of 100nm - 100 $\mu$ m in height and width. When the surface of the features is hydrophobic (nonpolar), water is unable to penetrate into the topology. From a materials viewpoint, surface textures which are hydrophobic can be fabricated by either texturing (lithographically, etching, etc.) nonpolar materials (e.g. hydrocarbon or fluorocarbon (teflon) polymers), layering hydrophobic particles or depositing polymers on flat surfaces, or coating already formed textures with nonpolar molecules (e.g. methyl- or fluoro-silanes) or polymers. The inability of water to penetrate into the texture leads to striking static and dynamic interfacial effects when an aqueous drop is placed on the surface: As shown in Fig. 2.1(a), when a water droplet is placed on a smooth flat surface either made of either the same material, or having the same surface coat as the microtexture, the droplet moves over the solid surface and comes to equilibrium. The contact angle  $\theta$  at equilibrium along the contact line is large (90° or larger) because of the surface hydrophobicity. For very hydrophobic materials or coatings (e.g. teflon),  $\theta$  can be as large as 120° (but no larger) and drops appear to bead-up on the surface. When a water droplet is placed upon and spreads along a hydrophobic microtexture in air (Fig. 2.1(a)), the droplet moves along elevations and above

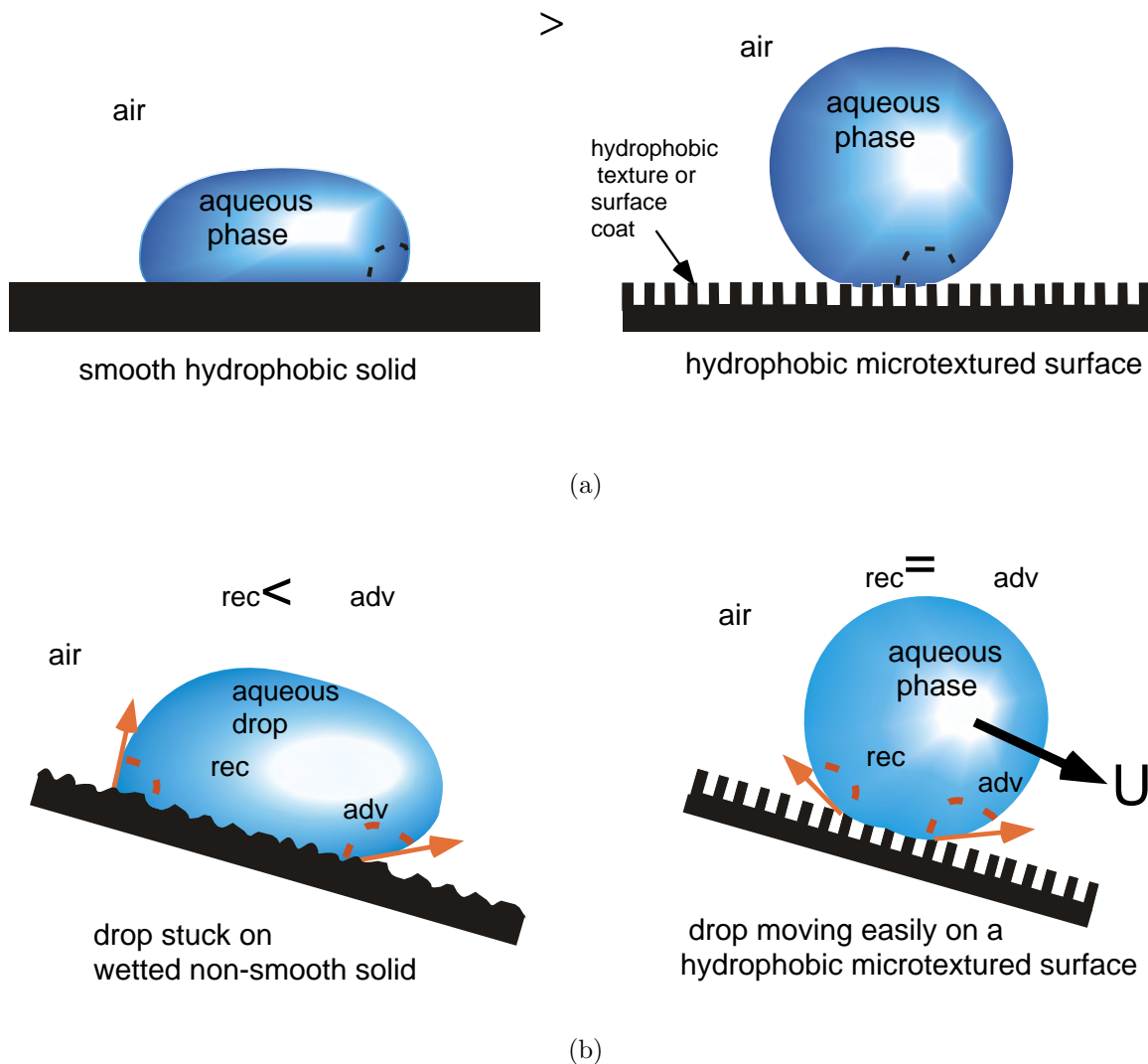


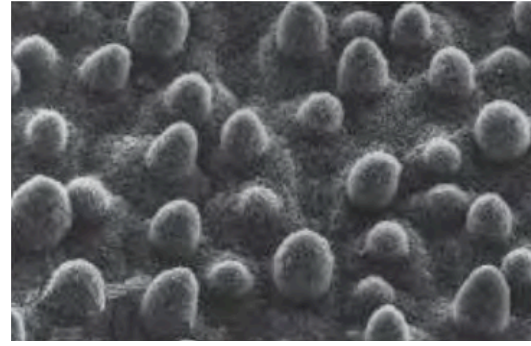
Figure 2.1: (a) Equilibrium configurations and contact angles of an aqueous drop on a flat, hydrophobic surface and a microtextured interface with a hydrophobic surface in which water does not wet into the texture (Cassie-Baxter wetting). (b) Contact angle hysteresis on a textured surface in which water wets into a texture not as hydrophobic or hydrophilic (Wenzel state), and gliding motion without hysteresis over a hydrophobic microtexture in the Cassie-Baxter state.

pockets of air in the microtexture, rather than saturating into the texture, and stops as the contact line becomes pinned on the edges of the texture. Because of the pinning, for droplets of equal volume as on the solid surface, the static equilibrium contact angle on the texture is much larger than that over the flat surface of the same hydrophobic material or surface coat, and the droplet appears to be nearly non-adherent, resembling pearls or marbles on a surface, as contact angles  $\theta^*$  approaching  $180^\circ$  can be achieved (Cassie-Baxter wetting and super-hydrophobic behavior)<sup>1-19</sup>. Droplet dynamics is also significantly different along hydrophobic microtextured surfaces relative to flat non-polar surfaces: On the flat surface, the drop drags along the surface with large surface friction to the liquid viscosity, while along the microtextured surface the air cushion significantly reduces the surface skin friction and droplets glide along the surface. Droplet movement is accompanied by the motion of the advancing and receding contact lines at the leading and trailing edge of the droplet surface. On an ideally flat surface which is perfectly smooth, the contact line advances with the equilibrium contact angle on both edges, the air/liquid interfacial tension force ( $\gamma$  on the droplet is equal on both edges and there is no net contact line resistance to the motion. But if the surface is textured, and the texture is not very hydrophobic (or is hydrophilic) so that the aqueous phase wets into the texture (Wenzel wetting), contact angles  $\theta_{wettexture}$  are much smaller than over the superhydrophobic surface, but the contact lines at the front and back of the drop impede the droplet motion (Fig. 2.1(b)). For the droplet to move, at the leading edge large contact angles ( $> \theta$ ) are necessary (relative to the mean plane) to move down an elevation, while small angles ( $\theta$ ) are necessary at the back end, leading to a net air/water interfacial tension force on the droplet retarding the forward motion (contact angle hysteresis)<sup>20-22</sup>. This resistance immobilizes droplets on tilted surfaces from moving downward due to gravity, and large tilt angles can be necessary for drop motion. Water droplets on superhydrophobic microtextured surfaces exhibit a reduced resistance to contact line motion as the liquid perimeter of the drop either at the forward or trailing edges of the drop jumps from one pinning point on the texture to the next (Fig. 2.1(b)). The advancing and receding contact angles are equal to  $\theta^*$ , and there is no resultant interfacial tension traction force<sup>23-28</sup>. Tilt angles of only a few degrees are necessary to make drops move over inclined superhydrophobic surfaces.

Nature provides several examples of water-repellant, superhydrophobic surfaces, among them the lotus leaf<sup>29,30</sup> (Fig. 2.2(a)) and the legs of a water strider<sup>31</sup> (Fig. 2.2(c)), where scanning electron microscopy (SEM) examinations detail a microstructure with waxy surface coats which create superhydrophobicity (2.2(b) and 2.2(d)). In the case of the water strider, the high contact angles due to the pinning allow the strider to support its weight on water. In the case of the lotus leaf, droplets glide over inclined leaf surfaces, collecting particles on



(a)



50  $\mu\text{m}$

(b)



(c)



(d)

Figure 2.2: Examples of superhydrophobic surfaces in Nature: (a) the lotus leaf and SEM of its hierarchical microtexture of posts (*papillae*) with nanoscale waxy tubules coating the projections and (b) the non-wetting legs of a water strider and an SEM of its elongated microstructures (*microsetae*).<sup>22</sup>



the surface and allowing the lotus leaf to be self-cleaning (2.3(a)) in removing dirt that can block sunlight and photosynthesis. Note that on flat surfaces in which liquid droplets drag over the surface, particles are redistributed by the droplet and do not self-clean (2.3(a)). The self-cleaning property of superhydrophobic surfaces can be used in many technologies such as self-cleaning coatings for satellite dishes, solar energy panels, photovoltaics and textiles<sup>32</sup>. As mentioned above, the reduced skin friction when a liquid flows over the surface suggests applications as drag reduction coatings for open and closed channels (pipeline) flows<sup>31,33–35</sup> (2.3(b)), and water vehicles such as ships and submersibles. In addition, because water at the interface with the microtexture only minimally contacts the solid part of the texture at the elevations, these microtextures are effective as interfaces which resist ice formation (icephobic surfaces) and the adsorption of biomolecules and retention of microorganisms such as algae (biofouling)<sup>36</sup>

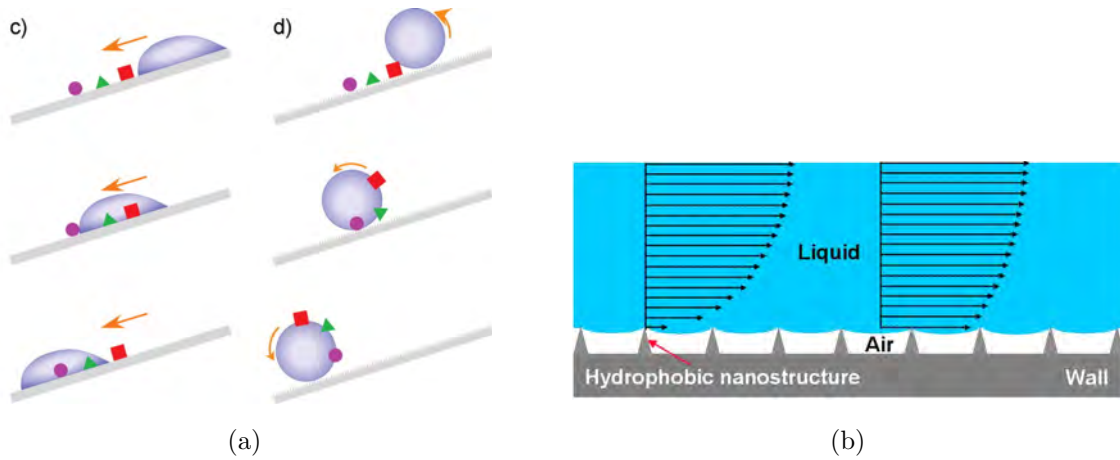


Figure 2.3: Applications of superhydrophobic surfaces: (a) Self-cleaning ability used by the lotus leaf. Particulates on the flat surface (c) are redistributed by a sliding drop, while (d) on a textured surface droplet rolls as opposed to slide and collects the particulates on its way. (b) Drag reduction: Air cushion on the textured surface of a wall reduces the fluid drag exerted on the wall since the fluid interface has zero shear stress.<sup>37</sup>

## 2.2 Research Objectives

Most of the research on superhydrophobicity has centered on the calculation of the equilibrium states of droplets resting on a surface. The initial studies of Cassie and Baxter<sup>38</sup> modeled the surface topology with elevations all of the same height with flat tops separated by air gaps and a solid area fraction given by  $\phi_s$  (see Fig. 2.4(a)). A variational approach

was used to compute the differential change in interfacial energy over this idealized surface as the drop contact line spreads over an area  $\delta a$  along the solid tops and across the air gaps, with  $\delta a$  assumed to be much larger than the sizes of the solid areas and the air gaps. Thus the contact line samples several microstructures, and the following macroscopic or “average” equilibrium contact angle  $\theta^*$  is obtained:

$$\cos \theta^* = -1 + \phi_s(\cos \theta_{planar} + 1) = \frac{\gamma_{SV} - \gamma_{SL}}{\gamma} \quad (2.1)$$

where  $\gamma_{SV}$  is surface energy of the dry solid,  $\gamma_{SL}$  is the surface energy of the wetted solid,  $\gamma$  is the surface tension of the liquid and  $\theta_{planar}$  is the (obtuse) contact angle the water makes on a planar surface of the (hydrophobic) texture material or a planar surface with the same surface coat. Since the surface is hydrophobic  $\gamma_{SV}$  is less than  $\gamma_{SL}$  and the contact angles on the microtextured surface are obtuse and approach  $180^\circ$  as the area fraction tends to zero. If the aqueous phase wets the topology (Wenzel wetting), i.e. the surface is hydrophilic or slightly hydrophobic, then using a similar derivation<sup>39</sup> (see Fig. 2.4(b)) the contact angle is given by

$$\cos \theta_{wetted}^* = r \cdot \cos \theta_{planar} = \frac{\gamma_{SV} - \gamma_{SL}}{\gamma} \quad (2.2)$$

where  $r$  is the surface roughness, defined as  $r = (\text{actual surface area})/(\text{geometric surface area})$

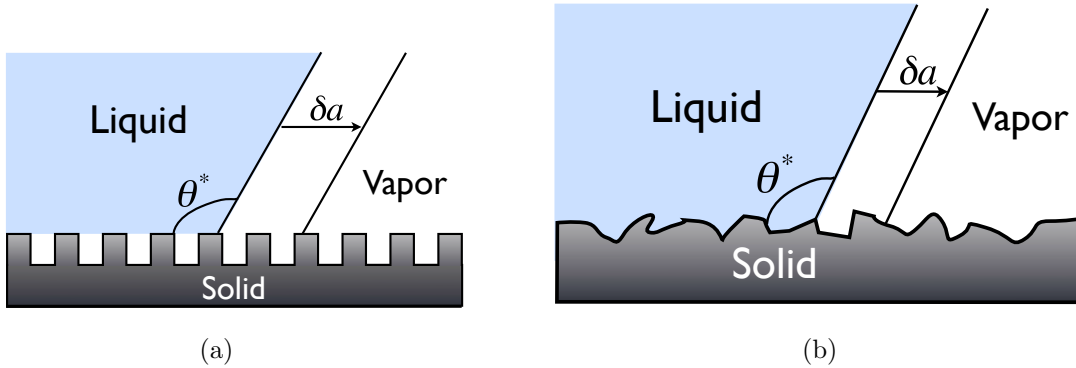


Figure 2.4: Variational approach for obtaining equilibrium contact angle for a water droplet spreading over (a) a microtextured surface in which the water does not wet the texture (Cassie-Baxter superhydrophobic regime) and (b) the water wets the texture (Wenzel state).

area) and  $\theta$  is the (acute) contact angle of water on the planar hydrophilic surface. Since the water wets the solid,  $\gamma_{SV}$  is greater than  $\gamma_{SL}$  and the angles on the wetted texture is acute and decrease as the roughness increases (see the discussion in<sup>40–42</sup>. More recent research on the calculation of the equilibrium states have obtained global free energy minima for a droplet on a given surface topography without averaging the texture properties. In these

procedures, the free energy of a given volume of a droplet in the form of a spherical-cap (gravity is ignored) is calculated for different contact angles corresponding to different wetting surface coverage. A global minimum is obtained in the free energy, corresponding to the equilibrium contact angle, and this angle was shown to be in close agreement with the predicted values from Wenzel and Cassie-Baxter equations<sup>3,43–45</sup>. The energetics of the transitions between the Wenzel wetting and Cassie-Baxter nonwetting states have also been studied both experimentally as well as theoretically<sup>7,43,46–48</sup>. Again free-energy minimization principles are used to describe which wetting state is favorable and phase diagrams are constructed based on the surface geometric properties.

Although the above theories based on thermodynamic grounds do elucidate the effect of the geometric properties of the texture on the achieved equilibrium contact angles, the dynamics of the spreading process and how the texture affects the rate of spreading - all important for applications in self-cleaning - have not been studied in detail. The aim of this study is to examine theoretically and experimentally the hydrodynamics of the spreading process as a water droplet spreads along a microtextured surface in superhydrophobic (Cassie-Baxter) wetting, and focus on the interaction of the fluid with the surface topology. Only a few articles have appeared in the literature studying the dynamics, and these have focused on theory and have used the Lattice-Boltzmann method to model the spreading<sup>48–51</sup>. Our modeling effort will focus on droplet motions in which the fluid inertia is negligible, and we will use a boundary integral method to solve the hydrodynamic equations for the gravity-driven motion of the fluid in the drop. Our simulations are two-dimensional, and model the surface topology as a regular pattern of microposts as in Fig. 2.4(a). In Section 2.3, the formulation of the problem is presented. Section 2.4 describes the numerical solution to the problem where we demonstrate the use of Biharmonic Boundary Integral Method along with the code validation, followed by numerical results and discussion in section 2.5. Following these calculations, we present a series of related experiments on visualizing the two dimensional motion of droplets across a topology of parallel grooves that are fabricated using soft lithography. The flow is visualized using photography and a high speed camera. In section 2.6.1 we review the soft lithography methods used for fabricating regular/periodic micron scale patterns on a surface. To demonstrate in general how surfaces with regularly arrayed features can be superhydrophobic, in the following section 2.6.2 we fabricate surfaces with two dimensional arrays of pillars and holes, and measure the equilibrium contact angles of aqueous droplets placed on the surface by imaging the droplets on the surfaces. This imaging also reveals the Cassie-Baxter wetting conditions on the surface. The measured contact angles are then compared with the Cassie-Baxter equation (2.1). In the next section 2.6.3, the experiments on the grooved surfaces are described, and compared to the results of the two

dimensional simulations of the previous section. Experimentally droplet dynamics is studied by two procedures: firstly under gravity driven spreading and secondly with controlled spreading, i.e. by increasing the volume of the droplet gradually with time.

## 2.3 Model Formulation

We study the gravity driven spreading motion of a two-dimensional aqueous droplet on a superhydrophobic surface in the inertialess Stokes flow regime. The time evolution of the droplet profile can be obtained by solving the Stokes equations and computing the drop shape quasi-statically. Consider a fluid droplet on a surface with a viscous fluid region ( $\Omega$ ) separated from an inviscid air overlayer by a boundary ( $\partial\Omega$ ). The Stokes equations obeyed by the fluid are,

$$\begin{aligned}\nabla P &= \mu \nabla^2 \mathbf{u} + \rho \mathbf{g} \\ \nabla \cdot \mathbf{u} &= 0\end{aligned}\tag{2.3}$$

where  $\mathbf{u}(x,y)$  is the fluid velocity,  $P(x,y)$  is the pressure,  $\rho$  and  $\mu$  are the density and the viscosity of the fluid, and  $\mathbf{g}$  is the gravitational acceleration. Boundary conditions on the air/fluid interface are normal and tangential stress balances. The inviscid phase is assumed to be passive, hence zero tangential stress is exerted on the droplet surface, and the normal stress exerted by the droplet liquid is balanced by the surface tension (Laplace pressure) and the constant pressure in the inviscid phase.

$$\mathbf{t} \cdot \boldsymbol{\sigma} \cdot \mathbf{n} = 0\tag{2.4}$$

$$\mathbf{n} \cdot \boldsymbol{\sigma} \cdot \mathbf{n} = -\gamma \kappa\tag{2.5}$$

where  $\gamma$  is the surface tension of the liquid and  $\kappa$  is the curvature defined as positive if the center lies within the liquid,  $\mathbf{t}$  and  $\mathbf{n}$  are counter-clockwise tangential and outward normal unit vectors and  $\boldsymbol{\sigma}$  is the stress tensor

$$\boldsymbol{\sigma} = -P\mathbf{I} + \mu (\nabla \mathbf{u} + (\nabla \mathbf{u})^T).$$

On the solid wall the classical no-slip boundary condition is applied,  $\mathbf{u}(x, y) = 0$ .

### 2.3.1 Singularity at the contact point and slip velocity

As the droplet spreads, the contact line has to move or slide along the surface. One common problem associated with the hydrodynamic solution of problems with a contact line move-

ment is the singularity that arises due to the discontinuity in the boundary conditions at the contact point. On the free air/water interface we have a finite velocity but on the solid wall the fluid velocity is zero due to the no-slip condition. This gives rise to an unrealistic infinite force at the contact line<sup>52</sup>. As a consequence, although the solid surface remains at rest, fluid in contact with it has to move violating the no-slip boundary condition. For highly wetting fluids, to eliminate this singularity, a precursor film models have been used widely, where it is assumed that a thin layer of liquid (precursor film) is present ahead of the contact line and the free fluid-fluid interface then merges smoothly with the precursor film at the contact line<sup>53,54</sup>. For partially wetting fluids, this stress singularity can be avoided by relaxing traditional no-slip boundary condition, i.e. by allowing some finite slip velocity at the contact line or by not-so-realistic approach of setting the contact angle to  $\pi$  (rolling motion instead of sliding)<sup>55</sup>. Slip velocity at the contact line can be imposed in several ways. Navier-type slip model is based on the concept of finite slip-length,  $b$ , (distance beyond liquid-solid interface in a direction perpendicular to the wall where velocity approaches zero), where slip velocity at a wall is proportional to the wall shear stress with proportionality constant as  $b$ . Greenspan used Navier-type slip model near the contact line while smoothly reverting to no-slip condition outside the contact line region<sup>56</sup>. More simplified approach is using a numerical slip as demonstrated by Mazouchi et al<sup>57</sup>, where slip at the contact point is implemented implicitly by discretizing domain with grid points around the contact point but not including the contact point. The governing equations are then solved with traditional no-slip condition at all grid points along the solid substrate and the position of the new contact line is determined by extending the calculated fluid-fluid interface till the solid surface with independently prescribed contact angle. In this work Mazouchi et al have assumed the prescribed contact angle is constant during the simulations and is equal to the static advancing contact angle, independent of the contact line velocity.

We use a slightly modified slip model than Mazouchi et al, where we compute slip velocity by taking into account dynamic contact angles and contact angle hysteresis. Contact angle hysteresis is a phenomena during which contact line remains fixed at a position (zero slip velocity) for a range of contact angles,  $\theta_{rec} \leq \theta \leq \theta_{adv}$ , where  $\theta_{rec}$  and  $\theta_{adv}$  are the static receding and static advancing contact angles respectively. When there is a relative motion between a contact line and solid surface, the contact angle liquid makes with the solid,  $\theta_{dyn}$ , is a function of the relative velocity. This contact angle hysteresis and a relationship between dynamic contact angle and slip velocity is shown in Fig. 2.5. Only when the dynamic contact angle  $\theta_{dyn}$  becomes larger than  $\theta_{adv}$ , droplet interface slips forward with a velocity  $V > 0$  and similar way when  $\theta_{dyn} < \theta_{rec}$ , the interface recedes, i.e.  $V < 0$ . There is a body of literature where experimentally measured dynamic contact angles for different slip velocities are fitted

to an empirical relation, one such relationship is the Hoffman-Jiang correlation<sup>58</sup>:

$$\frac{\cos \theta_{adv} - \cos \theta_{dyn}}{\cos \theta_{adv} + 1} = \tanh(4.96Ca^{0.702}) \quad (2.6)$$

where  $Ca$  is a capillary number,  $Ca = \mu V / \gamma$ ,  $V$  is the slip velocity. We use numerical slip model where new contact line position is obtained iteratively till above relation is satisfied for the contact angle and slip velocity.

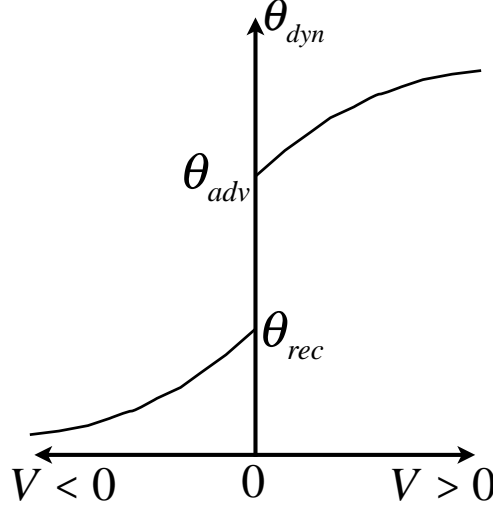


Figure 2.5: Relationship between dynamic contact angle and slip velocity.

## 2.4 Numerical Solution

### 2.4.1 Biharmonic Boundary Integral Method

We use the Boundary Integral Method for solving this problem.<sup>59 60</sup>. The advantage of using the Boundary Integral Method is that we reduce the dimensionality of the problem by one, by making use of Green's second identity; i.e. transforming the Stokes equations which are valid on the entire fluid domain to integral equations which contain only information from the boundaries. It is convenient to use, as flow variables, the streamfunction  $\Psi$  and vorticity  $\omega$  defined as follows.

$$u_x = \frac{\partial \Psi}{\partial y}, \quad u_y = -\frac{\partial \Psi}{\partial x}, \quad (2.7)$$

$$\omega = -\nabla \times \mathbf{u} \quad (2.8)$$

Then the Stokes equations in terms of these new flow variables can be written as a biharmonic,

$$\nabla^4 \Psi = 0$$

or in split form,

$$\nabla^2 \Psi = \omega, \quad \nabla^2 \omega = 0 \quad (2.9)$$

Now applying Green's identity to these biharmonics, the streamfunction and vorticity at any arbitrary point  $p$  can be written in terms of information only from the boundary points  $q \in \partial\Omega$ .

$$\begin{aligned} \eta(p) \cdot \Psi(p) &= \int_{\partial\Omega} \left( \Psi(q) \cdot \frac{\partial G_1}{\partial n} - \frac{\partial \Psi(q)}{\partial n} \cdot G_1 \right) \cdot \partial \tilde{\Omega}(q) \\ &\quad + \frac{1}{4} \int_{\partial\Omega} \left( \omega(q) \cdot \frac{\partial G_2}{\partial n} - \frac{\partial \omega(q)}{\partial n} \cdot G_2 \right) \cdot \partial \tilde{\Omega}(q) \end{aligned} \quad (2.10)$$

$$\eta(p) \cdot \omega(p) = \int_{\partial\Omega} \left( \omega(q) \cdot \frac{\partial G_1}{\partial n} - \frac{\partial \omega(q)}{\partial n} \cdot G_1 \right) \cdot \partial \tilde{\Omega}(q) \quad (2.11)$$

where  $\tilde{\Omega}(q)$  is a differential increment along the boundary at  $q$ ,  $\eta(p)$  and is given by

$$\begin{aligned} \eta(p) &= 0, \quad \text{if } p \notin \Omega + \partial\Omega, \\ &= \varphi, \quad \text{if } p \in \partial\Omega, \\ &= 2\pi, \quad \text{if } p \in \Omega. \end{aligned} \quad (2.12)$$

and where,  $\varphi$  is the angle between the two tangents on either side of the point  $p$ .  $G_1$  and  $G_2$  are the fundamental solutions of

$$\nabla^2 G_1 = \delta(|p - q|), \quad \text{and} \quad \nabla^4 G_2 = \delta(|p - q|)$$

which gives,

$$G_1 = \log |p - q|, \quad \text{and} \quad G_2 = |p - q|^2 (\log |p - q| - 1) \quad (2.13)$$

We have four variables  $\psi$ ,  $\omega$  and their normal derivatives involved in the governing equations (2.10) and (2.11). Thus we have to write boundary conditions in terms of these four variables. Rigorous manipulation starting from Eq. (5.5) yields the tangential stress balance as

$$-\omega + 2 \frac{\partial^2 \Psi}{\partial s^2} + 2\kappa \frac{\partial \Psi}{\partial n} = 0 \quad (2.14)$$

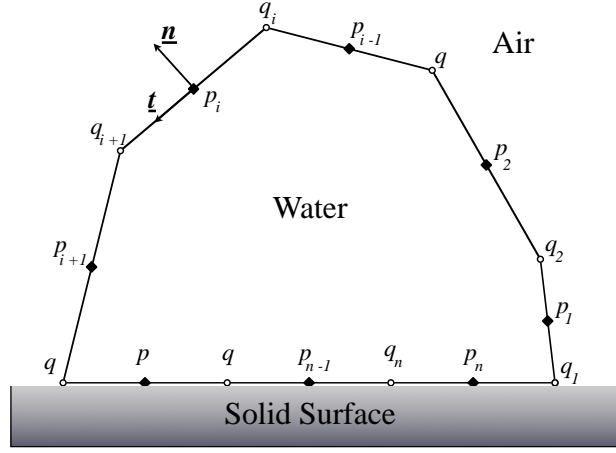


Figure 2.6: Schematic of approximating droplet with a polygon.

and eliminating the pressure term from equations (2.3) and (5.6) we get the normal stress balance condition as,

$$\frac{\partial \omega}{\partial n} + 2 \frac{\partial^2}{\partial s^2} \left( \frac{\partial \Psi}{\partial n} \right) - 2 \frac{\partial}{\partial s} \left( \kappa \frac{\partial \Psi}{\partial s} \right) = -\frac{\gamma}{\mu} \frac{\partial \kappa}{\partial s} - \frac{\rho}{\mu} g t_y, \quad (2.15)$$

where  $s$  is the arc-length. The no-slip condition at the solid surface can be written as  $\Psi = 0$  and  $\frac{\partial \Psi}{\partial n} = 0$ . These boundary conditions and the two biharmonic boundary integral equations are need to be solved simultaneously to obtain  $\Psi$  and  $\omega$  for the boundary points.

## 2.4.2 Implementation of Boundary Integral Method

As an analytical solution of this problem is not feasible, a numerical approach has to be adopted. We approximate the drop boundary by a polygon with  $N$  linear segments such that flow variables have constant values over each segment. As mentioned earlier, we employ a modified numerical slip model to solve this problem. In this model we do not evaluate flow variables exactly at the contact-line but at the midpoints of each segments as shown in the Fig. (2.6), where  $q_j$ 's are the vertices of the polygon and midpoints  $p_i$ 's are the collocation points or nodes, where we evaluate the flow variables. Hence, we apply the stress balance conditions on every node at the air/water interface and the no-slip condition is applied to the nodes which are on the solid-surface. By avoiding solving equations at the contact-point we naturally avoid the singularity.



The governing equations in discrete form can be written as,

$$\eta_i \Psi_i = \sum_{j=1}^N \left( \Psi_j \int_{\partial\Omega_j} \frac{\partial G_1}{\partial n} \partial\tilde{\Omega} - \frac{\partial \Psi_j}{\partial n} \int_{\partial\Omega_j} G_1 \partial\tilde{\Omega} + \frac{1}{4} \omega_j \int_{\partial\Omega_j} \frac{\partial G_2}{\partial n} \partial\tilde{\Omega} - \frac{1}{4} \frac{\partial \omega_j}{\partial n} \int_{\partial\Omega_j} G_2 \partial\tilde{\Omega} \right) \quad (2.16)$$

$$\eta_i \omega_i = \sum_{j=1}^N \left( \omega_j \int_{\partial\Omega_j} \frac{\partial G_1}{\partial n} \partial\tilde{\Omega} - \frac{\partial \omega_j}{\partial n} \int_{\partial\Omega_j} G_1 \partial\tilde{\Omega} \right) \quad (2.17)$$

which can be written in matrix form as

$$\mathbf{A}\Psi + \mathbf{B}\frac{\partial \Psi}{\partial n} + \mathbf{C}\omega + \mathbf{D}\frac{\partial \omega}{\partial n} = 0 \quad (2.18)$$

$$\mathbf{A}\omega + \mathbf{B}\frac{\partial \omega}{\partial n} = 0 \quad (2.19)$$

where,

$$A_{ij} = \int_{q \in \partial\Omega_j} \frac{\partial}{\partial n} \log |p_i - q| \partial\tilde{\Omega}(q) - \eta_i \delta_{ij}, \quad (2.20)$$

$$B_{ij} = - \int_{q \in \partial\Omega_j} \log |p_i - q| \partial\tilde{\Omega}(q), \quad (2.21)$$

$$C_{ij} = \frac{1}{4} \int_{q \in \partial\Omega_j} \frac{\partial}{\partial n} [ |p_i - q|^2 (\log |p_i - q| - 1) ] \partial\tilde{\Omega}(q), \quad (2.22)$$

$$D_{ij} = -\frac{1}{4} \int_{q \in \partial\Omega_j} |p_i - q|^2 (\log |p_i - q| - 1) \partial\tilde{\Omega}(q). \quad (2.23)$$

Taking advantage of the polygonal geometry, we evaluate these integrals analytically following Kelmanson's approach. Consider a triangle formed by node  $p_i$  and endpoints  $q_j$  and  $q_{j+1}$  of any boundary  $\partial\Omega_j$ , as shown in the Fig. (2.7) where,

$$\begin{aligned} a &= |p_i - q_j|, & b &= |p_i - q_{j+1}|, & h &= |q_j - q_{j+1}|, \\ \beta &= \angle p_i q_j q_{j+1}, & \text{and} & & \zeta &= \angle q_j p_i q_{j+1}. \end{aligned} \quad (2.24)$$

Using these notations, we can evaluate integrals in Eqs. (2.20)–(2.23) exactly as,

$$\int_{q \in \partial\Omega_j} \frac{\partial}{\partial n} \log |p_i - q| \partial\tilde{\Omega}(q) = \zeta, \quad (2.25)$$

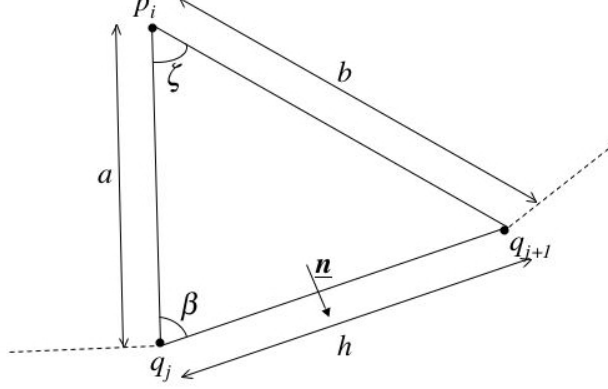


Figure 2.7: Triangle geometry for evaluating integrals in eqns. (2.20)–(2.23).

$$\int_{q \in \partial\Omega_j} \log |p_i - q| \partial\tilde{\Omega}(q) = a(\log a - \log b) \cos \beta + h \log b - h + a\zeta \sin \beta \equiv I, \text{ say,} \quad (2.26)$$

$$\int_{q \in \partial\Omega_j} \frac{\partial}{\partial n} [|p_i - q|^2 (\log |p_i - q| - 1)] \partial\tilde{\Omega}(q) = a(2I - h) \sin \beta, \quad (2.27)$$

$$\begin{aligned} \int_{q \in \partial\Omega_j} [|p_i - q|^2 (\log |p_i - q| - 1)] \partial\tilde{\Omega}(q) &= (a \sin \beta)^2 \left\{ I - \frac{2}{3}h - \frac{1}{3}a\zeta \sin \beta \right\} \\ &+ \frac{1}{3} \left\{ (h - a \cos \beta)^3 \left( \log b - \frac{4}{3} \right) + (a \cos \beta)^3 \left( \log a - \frac{4}{3} \right) \right\}. \end{aligned} \quad (2.28)$$

Also we discretize the tangential and normal stress balances, Eqs (2.14) and (2.15), along the arc-length. The calculations of the curvature, and the central difference scheme used for discretization are described in Appendices. Making use of the symmetry of the problem, we solve for only half of the droplet ( $x > 0$ ). On the axis of symmetry we provide boundary conditions as  $\psi = 0$  and  $\omega = 0$ . Then for a given initial shape we solve the following matrix system of  $4N$  unknowns and  $4N$  equations to obtain the flow variables.

$$\begin{pmatrix} \mathbf{A} & \mathbf{B} & \mathbf{C} & \mathbf{D} \\ \mathbf{0} & \mathbf{0} & \mathbf{A} & \mathbf{B} \\ \mathbf{R} & \mathbf{S} & \mathbf{T} & \mathbf{0} \\ \mathbf{U} & \mathbf{V} & \mathbf{0} & \mathbf{W} \end{pmatrix} \cdot \begin{pmatrix} \Psi \\ \partial\Psi/\partial n \\ \omega \\ \partial\omega/\partial n \end{pmatrix} = \begin{pmatrix} \mathbf{0} \\ \mathbf{0} \\ \mathbf{0} \\ \mathbf{b} \end{pmatrix} \quad (2.29)$$

$\mathbf{A}$ ,  $\mathbf{B}$ ,  $\mathbf{C}$  and  $\mathbf{D}$  are dense matrices and  $\mathbf{R}$ ,  $\mathbf{U}$ ,  $\mathbf{V}$  are tri-diagonal and  $\mathbf{S}$ ,  $\mathbf{T}$  and  $\mathbf{W}$  are diagonal matrices at the free surface. At the solid wall,  $R_{ij} = V_{ij} = \delta_{ij}$  and  $S_{ij} = T_{ij} = U_{ij} = W_{ij} = 0$ . The matrix system is then solved with LU decomposition to obtain the streamfunction

and its normal derivative at each boundary node, which is used to compute the velocities. Instantaneous velocities obtained are then used for generation of a new droplet profile by marching in time with the help of the kinematic condition,

$$x(t + \Delta t) = x(t) + u_x \Delta t, \quad \text{and} \quad y(t + \Delta t) = y(t) + u_y \Delta t, \quad (2.30)$$

where,  $u_x$  and  $u_y$  are the components of velocity  $\mathbf{u}$  in  $x$  and  $y$  direction. To get a position of the new contact line, the calculated new interface is made to intersect the solid surface at a position where dynamic contact angle-velocity correlation (Eq. 2.6) is satisfied.

During the time evolution of the droplet, boundary nodes may get convected along the surface and thus distribution of the nodes is no longer uniform. To avoid crowding/piling of nodes in some region as opposed to other, a cubic spline is fitted after every time iteration to the advanced droplet profile and boundary nodes are again redistributed. Also, often a high curvature region is obtained near the contact line during the spreading process, especially during the droplet spreading over a topography due to very large contact angles. In such cases, the air/fluid interface is smoothed out by fitting a cubic polynomial for the first few nodes from the contact line.

To summarize, a FORTRAN code is developed, which uses only an initial shape of a droplet. From this initial shape, using Boundary Integral Method, it computes matrix elements of Eq. 2.29. Matrix system is solved with LU decomposition to obtain flow variables. Using flow variables boundary nodes are advanced in time to get the new droplet profile. Contact point is moved with a slip velocity, dependent upon the dynamic contact angle. Boundary nodes are re-meshed and the process is repeated to obtain the time evolution.

### 2.4.3 Code Validation

The developed fortran code is validated by comparing calculated instantaneous flow variables with those obtained from an exact analytical solution of a simpler problem. Eq. (2.9), i.e.  $\nabla^4 \psi = 0$ , has a separable solution in polar co-ordinates

$$\psi(r, \theta) = r^{\lambda+1} f_\lambda(\theta), \quad (2.31)$$

where,  $\lambda$  is any constant (real or imaginary) and the general form of  $f_\lambda(\theta)$  is given by,

$$f_\lambda(\theta) = A_1 \cos [(\lambda + 1)\theta] + A_2 \sin [(\lambda + 1)\theta] + A_3 \cos [(\lambda - 1)\theta] + A_4 \sin [(\lambda - 1)\theta], \quad (2.32)$$

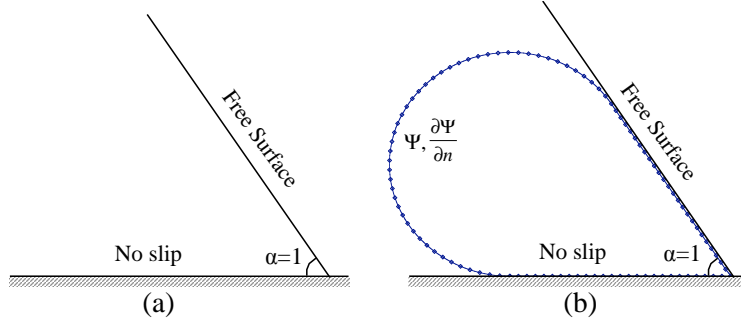


Figure 2.8: (a) Schematic of flow in a corner between a free and a no-slip surface. (b) Numerical grid employed to solve this problem using the Boundary Integral Method

$A_1$ ,  $A_2$ ,  $A_3$ , and  $A_4$  are constants to be evaluated from boundary conditions. We consider a problem of flow in a corner, formed by a no-slip surface and a free surface (Fig. 2.8), for which an analytical solution can be obtained. Normal and tangential stresses are applied on the free boundary and a no-slip condition at the solid surface, which are written as,

$$\begin{aligned}
 \text{No - slip} & : f(0) = f'(0) = 0, \\
 \text{Tangential Stress Balance} & : f''(\alpha) - f(\alpha)(\lambda^2 - 1) = 0, \\
 \text{Normal Stress Balance} & : f'''(\alpha) + (3\lambda^2 + 1)f'(\alpha) = 0.
 \end{aligned} \tag{2.33}$$

$\lambda(\alpha)$  can be obtained from the normal stress balance condition. We use  $\alpha = 1$ , for which  $\lambda = 0.814$ . Now we have three boundary conditions and four unknown constants. Thus, we arbitrarily fix  $A_1$  and evaluate the other constants as,

$$\begin{aligned}
 A_2 &= \frac{A_1}{\lambda + 1} \frac{(\lambda + 1) \cos [(\lambda + 1)\alpha] - (\lambda - 1) \cos [(\lambda - 1)\alpha]}{\sin [(\lambda - 1)\alpha] - \sin [(\lambda + 1)\alpha]}, \\
 A_3 &= -A_1, \quad \text{and} \quad A_4 = -\frac{(\lambda + 1)}{(\lambda - 1)} A_2.
 \end{aligned} \tag{2.34}$$

For solving this problem numerically using the boundary integral method, we have to have a closed calculation domain which is achieved by joining the two surfaces smoothly with a circular arc. As boundary conditions on the curved surface, we use the actual  $\psi$  and  $\frac{\partial \Psi}{\partial n}$  from the known theoretical solution. The matrix system in Eq. 2.29 is then solved with appropriate boundary conditions to obtain  $\psi$ ,  $\omega$  and their normal derivatives. Fig. 2.9 compares the flow variables obtained from the code with analytical values, and a very good agreement between the two is observed. The singularity at the apex (in between 26<sup>th</sup> and 27<sup>th</sup> node) has been handled well by the numerical method.

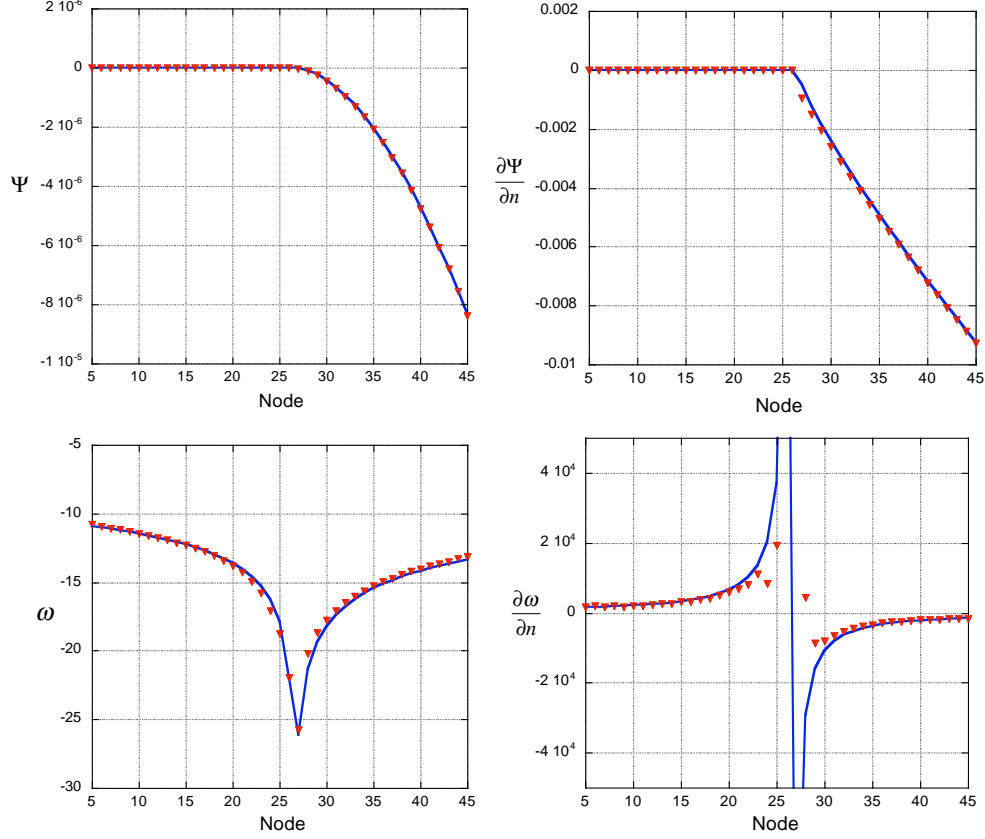


Figure 2.9: Comparison of numerical results (symbols) with analytical solution (solid line) for flow in a corner problem.

## 2.5 Numerical Results and Discussion

The first step in understanding the dynamics of the spreading of a droplet over a surface with topology is to study the equilibrium shapes of the drops after they have come to rest. These equilibrium shapes represent the final resting states of the trajectory of drops advancing over a surface. As such, in what will become clear further on, these shapes are important in constructing a correlation between the initial shape and location of a drop placed on a surface with topology, and its final position on that surface. The static equilibrium shapes are discussed in Section 2.5.1. Once we know all the possible equilibrium shapes for a droplet of a given volume, from integration of Young-Laplace equation, we consider the dynamics of the spreading motion over surfaces and we expect that the equilibrium shape obtained at the end of the dynamic process should correspond to one of the equilibrium shape predicted by the above procedure. Numerical results for the spreading dynamics are obtained from the Boundary Integral Method. In all simulations presented in further sections, we use the

representative case of a 2 mm in radius (circular) water droplet. The initial shape of the droplet is assumed to be section of a circle with radius  $a$ , and the droplet is symmetric about Y-axis. Time evolution is obtained by solving the Stokes equations by using the Boundary Integral Method. Equations are non-dimensionalized with initial drop radius,  $a$ , and the characteristic time and velocity are given by;

$$\tau' = \frac{\mu}{\rho g a}, \quad V' = \frac{\rho g a^2}{\mu}. \quad (2.35)$$

Thus, by writing the governing equations and boundary conditions in dimensionless form, the only parameter which remains is the Bond number,  $Bo = \rho g a^2 / \gamma$ , which is a ratio of the body forces to the surface tension forces. For a water droplet of radius  $a = 2mm$ , density  $\rho = 1000kg/m^3$  and with gravitational acceleration  $g = 9.81m/s^2$ , the Bond number is  $Bo = 0.545$  and this value is used in the simulations. First, we will describe the numerical results on a planar hydrophobic surface (without topography, Section 2.5.2), to provide base cases to compare with spreading over a surface which has topology. We then describe the spreading dynamics of a droplet over a superhydrophobic surface consisting of regular patterns of rectangular elevations separated by rectangular valleys (Section 2.5.3).

### 2.5.1 Static equilibrium shapes

Consider a 2-dimensional droplet of liquid with surface tension  $\gamma$  and density  $\rho$  resting on a surface in a gravitational field of  $g$ . The forces acting on the droplet are the gravitational or body force, and an interfacial or capillary force due to the surface tension of the liquid. On a planar surface, which is perpendicular to gravity, and of infinite extent, the equilibrium shape of the droplet on the surface is uniquely defined if two parameters are specified: volume of the droplet and a contact angle it makes with a surface. These are the familiar "sessile" forms. Thus for a given volume and contact angle, the droplet interface has a unique shape as described by the Young-Laplace equation,

$$\Delta P = \gamma \kappa = \frac{\gamma}{R} \quad (2.36)$$

where  $\Delta P$  is the pressure difference across the interface, which is balanced by the surface tension times the curvature  $\kappa$  of the interface, where  $R$  is the radius of curvature. This Young-Laplace equation can be integrated to obtain the interfacial shape at the equilibrium. Details of the procedure are provided in the Appendix C.

For a planar surface, for a given volume  $V$ , by changing the contact angle we can obtain different equilibrium shapes, which intersect the solid surface at different  $X$  positions. From

this exercise, we can obtain the extent of spreading on a flat surface, presumed to be infinite in extent, as shown in Fig. 2.10 for two different volumes ( $V_1$  and  $V_2$ ,  $V_2 > V_1$ ), where equilibrium contact angles are plotted against equilibrium  $X$  positions for contact angles (as measured through the liquid phase) up to  $180^\circ$ . Figure 2.10 shows that on a flat surface, as expected, a droplet which makes a larger contact angle on a flat surface spreads to a lesser extent as compared to a droplet which makes a smaller contact angle. The reason for this is the larger static contact angle generates very large curvatures and capillary pressures at the air/water interface near the contact line, which can support the weight of the droplet and restrict its spreading extent. Also, as shown in the figure, for the same contact angle a droplet with a larger volume spreads to greater extent as the curvature forces are not sufficient to support the larger weight of the droplet. Fig. 2.10 also presents the equilibrium shapes obtained by integrating the Young-Laplace equation for different equilibrium contact angles, namely  $100^\circ$ ,  $150^\circ$  for the volume  $V_1$ . It is clear from the interfacial loci depicted in the figure that the larger the contact angle the smaller the radius of curvature at the apex of the sessile drop.

In the context of the study of the droplet spreading dynamics on surfaces with topography, the final resting shapes of drops placed on the surface contact the surface on sharp  $90^\circ$  edges or corners where they become pinned. These final states represent sessile drops on finite planar surfaces in which the droplet hangs freely over the edge of the surface. They can be computed by integrating the Young-Laplace equation through the point at which the tangent to the surface becomes parallel to gravity and the shape becomes multi-valued in the coordinate  $x$ . For a fixed volume of droplet  $V$ , as the equilibrium  $X$  (edge or corner) position of these hanging shapes decreases from the  $X$  position of the droplet (with volume  $V$ ) with a contact angle of  $180^\circ$ , the hanging contact angle increases above  $180^\circ$  as shown in Figure 2.10. The shape for a hanging contact angle equal to  $192.5^\circ$  is shown, and the radius of curvature at the apex is larger than that of the droplet which intersects the surface at  $180^\circ$ .

### 2.5.2 Spreading dynamics over a planar surface

Here we present numerical results for a droplet spreading on a planar surface, i.e. without topography. As mentioned before, a singularity is associated with the three-phase contact line sliding over the surface. The first case we consider here is when the prescribed contact angle that the liquid makes with the solid is equal to  $\pi$  or  $180^\circ$ . In this case the droplet rolls over the surface (tank-treading motion) as opposed to sliding and thus the contact line singularity is absent. Fig. 2.11(a) shows the time evolution of a droplet. Initially, the

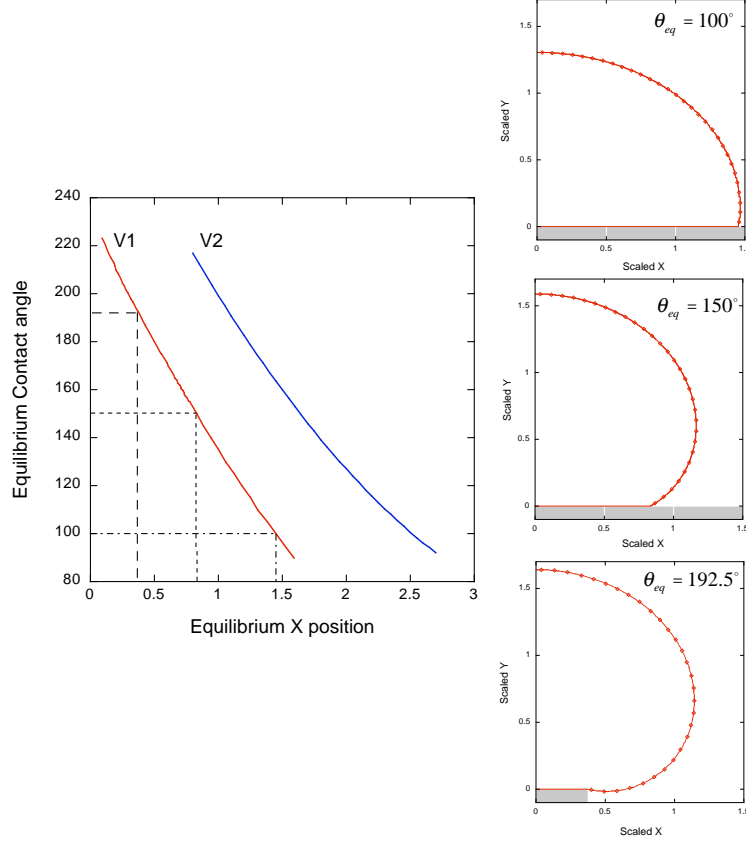
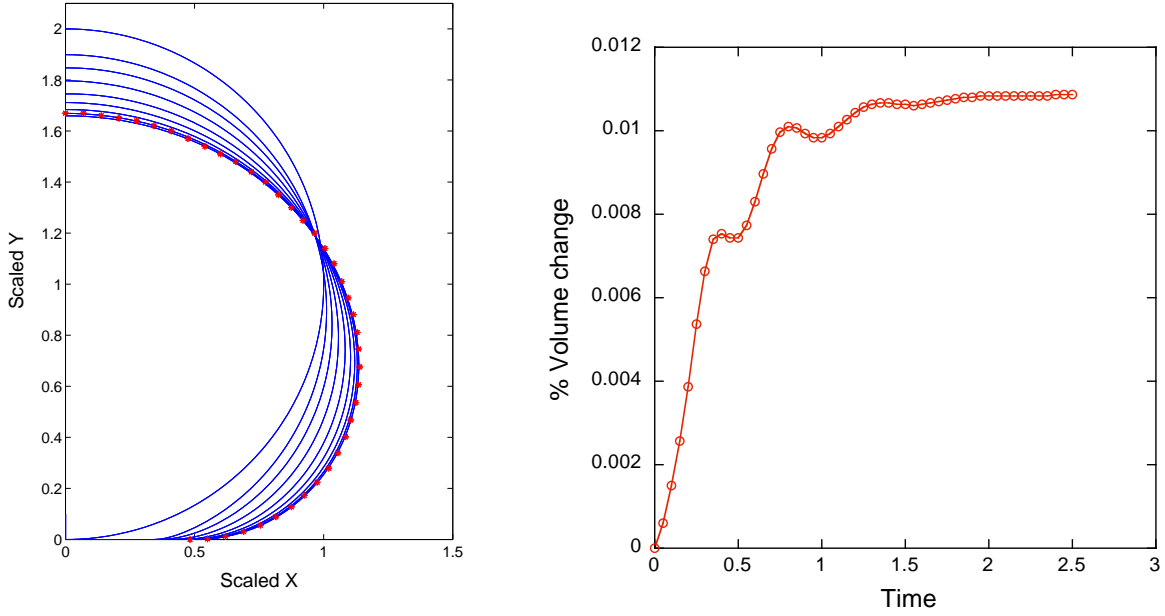


Figure 2.10: Graph on the left shows extent of spreading on a flat surface obtained from integration of the Young-Laplace equation for two different volumes  $V_2 > V_1$ ,  $V_1 = 12.46 \text{ mm}^2$  and  $V_2 = 28.11 \text{ mm}^2$ . Plots on the right show different equilibrium shapes obtained for same volume  $V_1$  at different equilibrium contact angles on a flat surface (shaded in grey). These three equilibrium points are also marked on the extent of spreading curve for volume  $V_1$ . Equilibrium angles larger than  $180^\circ$  are obtained if droplet is pinned indefinitely at a corner point. Droplets are symmetrical about Y axis.

shape of a droplet is prescribed to be a perfect circle (of radius  $a = 2\text{mm}$ ) just touching the flat solid surface only at a point. For a water droplet of radius  $a = 2\text{mm}$ , density  $\rho = 1000\text{kg/m}^3$  and with gravitational acceleration  $g = 9.81\text{m/s}^2$ , the Bond number is  $Bo = 0.545$  and this value is used in the simulations. The initial shape of the droplet is approximated by a polygon of  $N = 280$  sides. The matrix system generated by boundary integral code ( $1120 \times 1120$ ) is solved in a loop to obtain the time evolution of the droplet. The contact line is advanced by making the air/water interface to intersect the solid surface at the constant contact angle of  $180^\circ$ , which achieved by fitting a parabola through the last three points. As a function of time, under the action of gravity the droplet spreads on the flat surface with tank-treading motion until the equilibrium is reached, where gravitational



forces are balanced by the curvature and surface tension as shown in the Fig.2.11(a). At this



(a) Droplet shape evolution with time, solid lines represents numerical simulations at dimensionless time,  $\tau = 0, 0.05, 0.15, 0.3, 0.5, 0.75, 1.05, 1.4, 1.8$ , and symbols represents equilibrium shape obtained from integration of Young-Laplace equation. Excellent agreement between the two equilibrium shape is observed.

(b) Droplet volume change during the spreading dynamic simulations.

Figure 2.11: Droplet spreading over a flat surface with constant contact angle of  $180^\circ$ . Droplet rolls as opposed to sliding.

equilibrium shape, Young-Laplace equation is satisfied at every point on the boundary, i.e. pressure drop across the interface is equal to the surface tension times the curvature. This predicted Young-Laplace equilibrium shape is also plotted in the Fig.2.11(a), and excellent agreement between the two equilibrium shapes is obtained. This agreement validates our time dependent code. As a check on the incompressibility, the volume change during the spreading process is also plotted in Fig.2.11(b) and a negligible volume change is observed (about 0.01%).

However, as mentioned before, on a flat surface a water droplet cannot achieve a contact angle larger than  $120^\circ$ . Thus, this tank-treading motion is not possible for such a low contact angles and the droplet rather slides or slips on the flat surface. Fig.2.12 shows spreading dynamics of a droplet with specified static advancing contact angle of  $120^\circ$ . The drop initial shape prescribed to be a section of circle with initial contact angle of  $160^\circ$ . To provide slip at

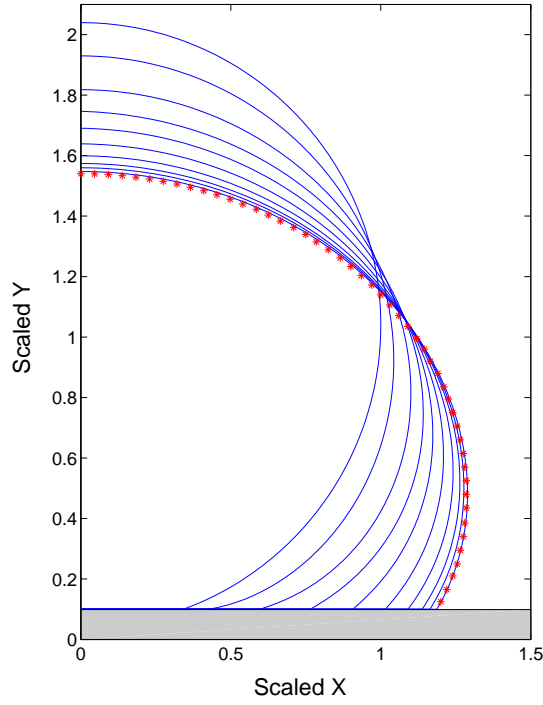


Figure 2.12: Droplet spreading over a flat surface (shaded in gray) with static advancing contact angle of  $120^\circ$ . Numerical results are shown with solid line at dimensionless time  $\tau = 0, 0.21, 0.67, 1.49, 2.8, 4.8, 7.73, 11.87, 1757$ , and  $30$ . Symbols represents equilibrium shape obtained from integration of Young-Laplace equation. Excellent agreement between the two equilibrium shape is observed.

the contact line Hoffman-Jiang correlation (Eq. 2.6) is used, which is solved iteratively during each time-step. Again the final equilibrium shape obtained by the simulations matches very well with the predicted Young-Laplace shape; in particular the final position of the contact line is predicted from Figure 2.10.

### 2.5.3 Spreading dynamics over topography

#### Modeling the Hydrodynamic Movement of a Contact Line Over a Surface Topography of Pillars

For studying the spreading dynamics of a droplet over a topography, we need to consider the interaction of the fluid flow with the surface microstructures from a hydrodynamic point of view. The droplet interface interacts with the surface through the contact angle hysteresis, and velocity dependent dynamic contact angles. Fig. 2.13 demonstrates pictorially these

interactions with different surfaces. Consider first a flat surface, Fig. 2.13(a). It is well known that in order for the liquid to spread on the flat surface, the liquid-air interface has to exceed a minimum critical contact angle, which is the static advancing contact angle ( $\theta_{adv}$ ) measured through the liquid till the solid surface. This  $\theta_{adv}$  is an intrinsic property of the liquid-solid system in consideration and is independent of the orientation of the flat surface. That is, if the liquid is spreading downwards on a vertical surface, Fig. 2.13(b), the minimum critical contact angle required for the on-set of the downward spreading motion is still  $\theta_{adv}$  but measured with respect to the vertical wall. To extend this concept of the static advancing contact angle to the surface with a topography in the form of pillars, consider a case in Fig. 2.13(c) where liquid spreads on the top horizontal surface of a pillar with minimum critical advancing angle of  $\theta_{crit,H}(=\theta_{adv})$ . But when droplet reaches the sharp corner point of this pillar, the contact line can slip vertically downwards only if it exceeds  $\theta_{crit,V}(=\theta_{adv} + 90^\circ)$  measured with respect to the horizontal surface. Thus, for all dynamic contact angles in the range  $\theta_{crit,H} \leq \theta_{dyn} \leq \theta_{crit,V}$  the contact line does not move, when at the corner, even though interface makes contact angle larger than  $\theta_{adv}$  with the horizontal plane. In other words, these sharp corner points act as pinning points – they pin the contact line at the corner – and offers multiple static contact angles. The rest of the droplet, however, is free to move, and if the droplet can come to an equilibrium shape with a contact angle within the above mentioned limits then further droplet spreading motion is arrested. On the other hand, if such an equilibrium shape does not exist for a given volume of the drop at a given pinning position, then dynamic contact angle exceeds  $\theta_{crit,V}$  and the contact line begins its motion again. In this process, the free interface of the droplet bends so much that it is possible for the interface to touch the neighboring post/pillar and then that touching point becomes the new contact line. The droplet then spreads further on the top horizontal surface of the next pillar.

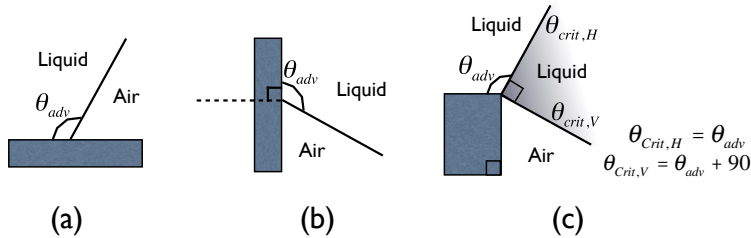


Figure 2.13: Minimum critical contact angles for the on-set of droplet contact line motion: (a) forward on a horizontal surface, (b) downward on a vertical surface, and (c) horizontal till the corner and downward after pinning at the corner for contact angles in the range  $\theta_{crit,H} \leq \theta_{dyn} \leq \theta_{crit,V}$

## The Indefinite Pinning of an Advancing Droplet At a Corner

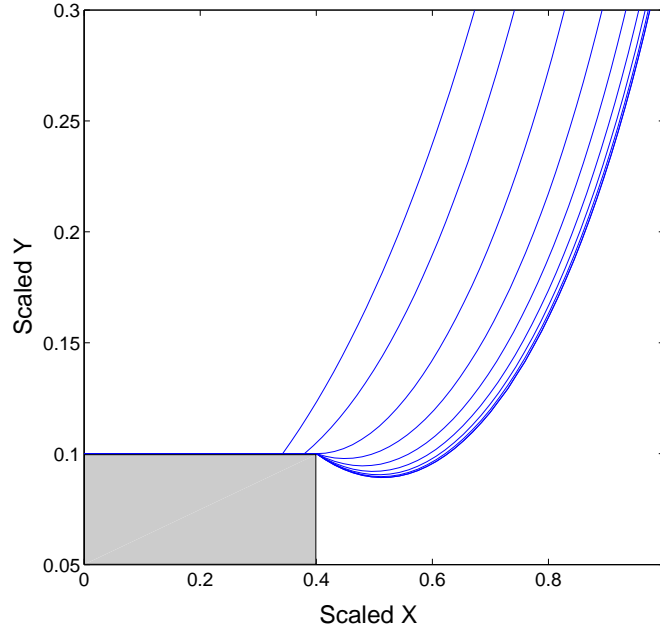


Figure 2.14: Droplet initially spreads over a flat surface (shaded in gray) with static advancing contact angle of  $120^\circ$  and suddenly gets pinned at a corner point located at  $X = 0.4$ . Numerical results are shown at dimensionless time  $\tau = 0, 0.1, 0.3, 0.6, 1, 1.5, 2.1, 2.8, 10.25$  and  $28.25$ . Apparent equilibrium contact angle observed was  $\theta_{eq}^* = 189.98^\circ$ , which can be located on extent of spreading curve (Fig. 2.10) for volume  $V1$  at pinning position of  $X = 0.4$

As an illustration of the pinning of the droplet contact line at a corner, we choose the same initial shape for the droplet, a section of a circle with a contact angle of  $160^\circ$  and a volume  $V=V1$  (from Figure 2.10)  $=12.46 \text{ mm}^2$ , and an advancing contact angle ( $120^\circ$ ) as the previous simulation on a flat surface (Figure 2.12). However, an edge is located at a distance of  $X = 0.4$  from the centerline of the drop. We choose this value for the edge location because it is clear from Figure 2.10 that for this volume a hanging drop pinned at  $X = 0.4$  can exist at equilibrium with a hanging angle of approximately  $190^\circ$ . Importantly this angle is smaller than the angle ( $\theta_{crit,V} = \theta_{adv} + 90 = 210^\circ$ ) required for the drop to slide down the vertical surface. Hence we anticipate the drop to move first, and subsequently get pinned at the corner until equilibrium. Incorporating the interaction between the topography and the fluid flow over a textured surface as described above, Fig. 2.14 shows the numerical results for a droplet spreading on a flat surface up to the distance of  $X = 0.4$  where it encounters the corner or pinning point. As the simulation begins, the droplet initially spreads on the flat surface as the dynamic contact angle is larger than  $\theta_{adv}$ . At time  $\tau = 0.1455$  the contact

line reaches the corner point (at  $X = 0.4$ ) and the contact line gets pinned indefinitely at this point. But as the rest of the droplet shape is still not an equilibrium shape, the interfacial nodes continue to move. The interface bends over while remaining pinned at the corner point until finally an equilibrium configuration is reached where all the forces are balanced. The final equilibrium shape is realized at the corner point with the equilibrium contact angle of about  $189.98^\circ$  in agreement with Fig. 2.14. This very large contact angle is possible because it still lies in the range of  $\theta_{crit,H} \leq \theta_{eq} \leq \theta_{crit,V}$ . The contact line position and the contact angle as a function of time indicate that the contact line slips until it reaches the corner point, where it sticks until equilibrium. Similarly, the contact angle increases monotonically when the contact line is pinned at the corner and reaches an equilibrium value of  $189.98^\circ$ .

### The Spreading Dynamics of Droplets Over Consecutive Pillars

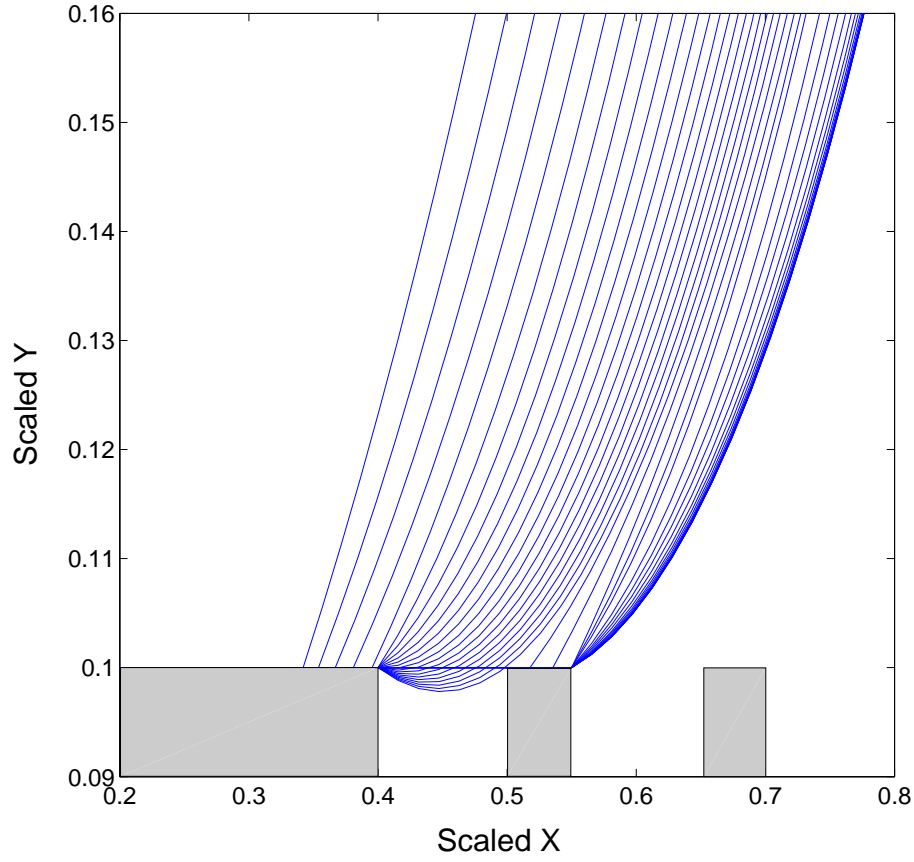
With reference to the previous simulation of movement over an isolated pillar and pinning at the downstream edge, advancement over a microtextured surface of pillars involves the fundamental steps of movement over the horizontal surface of the pillar to the corner edge to form a hanging drop, followed by attachment of part of the meniscus to the next pillar. For this attachment to occur, the next pillar must be close enough (that is the gap small enough) so that the hanging drop – as it evolves over the edge – contacts the next pillar with its hanging interface before coming to an equilibrium or, if it cannot reach equilibrium, develop a contact angle with respect to the vertical larger than the advancing angle so it moves down the vertical wall of the pillar. (In the latter case, attachment can still occur as the movement down the vertical wall allows the meniscus to come in contact with the next pillar.) Fig. 2.15(a) shows droplet spreading motion over a surface composed of a topography in the form of a width of the pillar = 0.05 and gap = 0.1. Initial shape is similar as before but the prescribed advancing contact angle is  $100^\circ$ . Droplet spreads initially on the flat surface till the corner at  $X = 0.4$  and contact line remains pinned while the interface bends over. And before it can come to an equilibrium, contact line touches the neighboring pillar at  $X = 0.5$  and begins its spreading motion till it is pinned at the next pinning corner at  $X = 0.55$  and finally comes to an equilibrium as all the external forces and the contact angle boundary conditions are satisfied. We see distinct slip-stick-jump motion of the contact line over the topography while trapping an air underneath the droplet. Slipping over the horizontal surface, sticking to the corner point and jumping from one pillar to the next. Fig. 2.15(b) shows this motion when we plot the contact line X position as a function of a time and contact angle also varies accordingly. Thus, just by prescribing an intrinsic angle of only  $100^\circ$  and having a topography on the surface, we see that the final equilibrium angle reached by the droplet is very large (about  $174.3^\circ$ ). This large equilibrium angle is possible because

the multiple contact angles offered by the sharp pinning point. Final equilibrium position of the contact line and the contact angle can be located on the extent of spreading curve generated before.

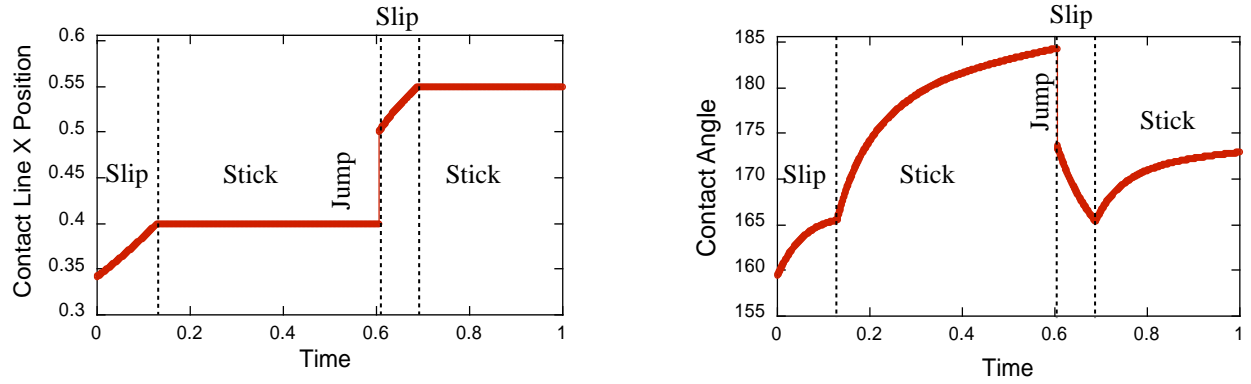
Note that in these simulations, after droplet contact line jumps to the next pillar, liquid-air meniscus in between the two pillar is considered to be flat. That is, although zero tangential stress condition is applied on the free air-water interface riding over trapped air pocket, normal-stress balance is not solved for. Instead,  $\psi = 0$  is specified on the flat interface. This simplification is valid, as long as the radius of curvature of the free interface is much larger than the distance between the two pillars, which is usually the case. We have also investigated the spreading dynamics while considering the curvature of the interface, and found that the curvature is indeed small and the final equilibrium shape and overall dynamics of the droplet is not affected. Spreading dynamics of the droplet is dominated by the contact line motion and free interface above the solid but it is unaffected by solid topography or shape of the liquid menisci in the interior of the droplet. Some of the numerical results capturing dynamics of the liquid meniscus can be found in Appendix D at the end of the chapter.

For the topography considered in our simulation, if we compute the average solid area fraction ( $\phi_s$ ) available for a droplet to spread on a composite surface made of pillar width = 0.05 and gap = 0.1, we get  $\phi_s = 0.333$  and corresponding predicted contact angle by Cassie-Baxter relation (Eq. ??) is  $136.43^\circ$ . There is clearly a mismatch between the two equilibrium contact angle on a similar surface topography. But the equilibrium shape we obtained by our simulation is a perfectly valid shape for a given volume and it falls exactly on the straight line predicted by integrating Young-Laplace equation (Fig. 2.10). That is, in the equilibrium shape obtained in our simulation the pressure difference across the interface is exactly equal to the curvature times the surface tension at every single point on the interface. Reason behind this discrepancy is that the relations based on variational energy principles consider the surface is composed of micro-structures so small that surface is assumed to have some average properties, i.e. effective solid-vapor surface energy ( $\gamma_{SV}^*$ ) and effective solid-liquid surface tension ( $\gamma_{SL}^*$ ), as mentioned before. And droplet is assumed to be spreading over a macroscopically flat, but with an average lower energy surface. This variational energy approach clearly does not account for interaction of the flow with the topography. This interaction, as described earlier, can result in any equilibrium contact angle if  $\theta_{crit,H} \leq \theta_{eq}^* \leq \theta_{crit,V}$  inequality is satisfied. And final equilibrium contact angle achieved depends on the history of the droplet.

In simulation presented in Fig. 2.15(a) droplet never feels the presence of the second pillar situated at  $X = 0.65$ . However, if we push the droplet down forcefully – on the



(a) Time evolution of the droplet shape near the contact line region. Droplet achieves a final equilibrium shape at the pinning point located at  $X = 0.55$ .



(b) Left hand side plot shows slip-stick-jump motion of the contact line, contact line slips on the horizontal surface, sticks after reaching the corner point and jumps from one pillar to the next. Corresponding dynamic contact angles are plotted on the right.

Figure 2.15: Droplet spreading dynamics over a topography composed of solid width = 0.05 and gap = 0.1 for advancing contact angle of  $100^\circ$ .

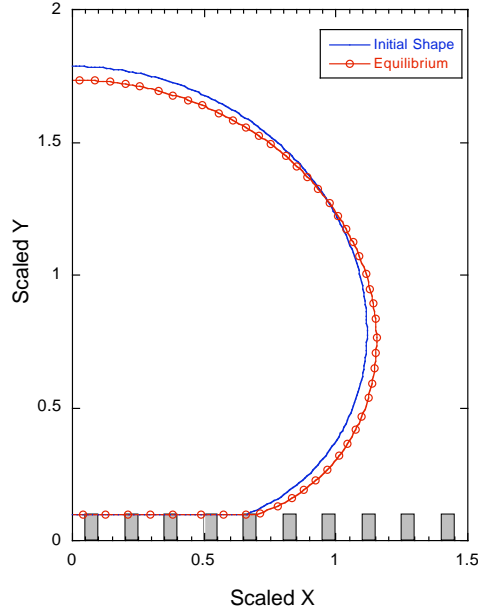
same textured surface as above – it sees or explores the pillars located at farther distances. For example, in Fig 2.16(a), Fig 2.16(b), Fig 2.16(c) and Fig. 2.16(d) where droplet initial shape itself has a contact line already located on more distant pillars. In such cases droplet still spreads ahead as the contact angle it makes with the horizontal surface is larger than  $\theta_{adv} = 100^\circ$  and comes to an equilibrium at the next available pinning point. Thus, depending upon where the final pinning point is located, the apparent equilibrium contact angle varies. Figures show that for pinning points located at  $X = 0.7$ ,  $X = 0.85$ ,  $X = 1.0$  and  $X = 1.15$ , apparent equilibrium contact angles obtained on the exactly same textured surface, for the same volume droplet, are  $161.98^\circ$ ,  $148.29^\circ$ ,  $135.23^\circ$  and  $122.57^\circ$  respectively. And all these equilibrium shapes fall on the extent of spreading curve, as shown in Fig. 2.17. Fig. 2.17 also plots the Cassie-Baxter equation predicted angle on the curve and we see that contact angles larger or smaller than Cassie-Baxter prediction are possible, provided they are within the range  $\theta_{crit,H} \leq \theta_{eq}^* \leq \theta_{crit,V}$  and we have pinning points at respective locations. In other words, for a textured surface, there is no one single apparent equilibrium contact angle (like obtained from global energy minimization or Cassie-Baxter relation) that describes the surface fully.

In above simulations, droplet contact line never starts its downward motion once it is pinned. In order to see this penetrating motion, contact angle has to exceed the critical angle of  $\theta_{crit,V}$ . To demonstrate this behavior we consider a case where intrinsic advancing contact angle is  $90^\circ$ . Therefore, when contact angle exceeds  $180^\circ$ , contact line will resume its downward motion and equilibrium angles larger than  $180^\circ$  cannot be realized as in the case of Fig. 2.14. Fig.2.18 and Fig 2.19 shows slip-stick-penetration-jump behavior for two different pillar densities, where contact line after sticking penetrates down the pillar before the interface touches the next surface. Extent of downward penetration is not significant but can be seen in the simulations. And again, final equilibrium position and the contact angle can be located on the extent of spreading curve.

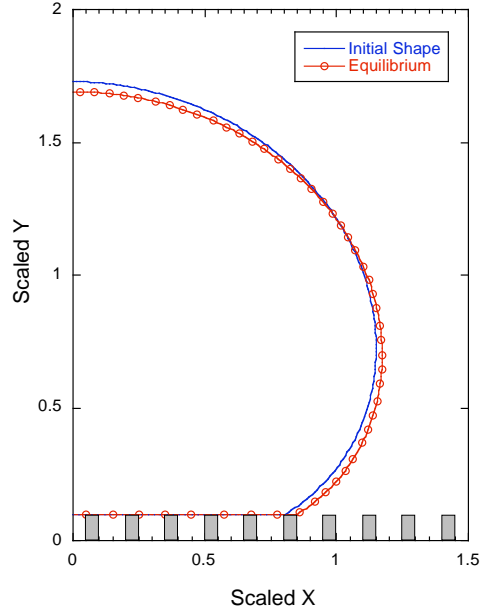
## 2.6 Experimental Studies

This section presents experimental investigations of superhydrophobic surfaces. In section 2.6.1 we demonstrate techniques used for fabricating regular/periodic patterns on the surface, which are of the micron-scale, and characterizing these surfaces for their micro-structures as well as static equilibrium contact angles. In section 2.6.3, dynamics of a droplet spreading over a micro-textured surface is presented while maintaining conditions somewhat similar to the numerical section so that a qualitative comparison could be made between the two. Experimentally droplet dynamics is studied by two procedures: firstly under gravity driven

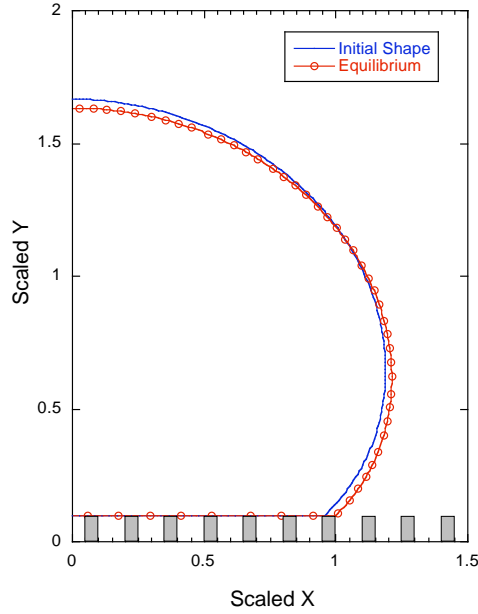




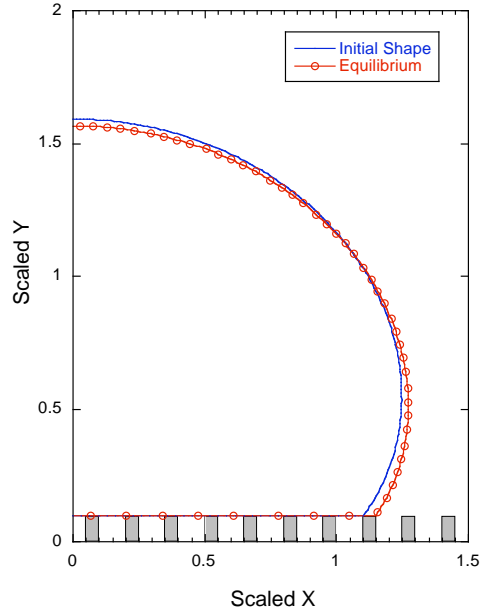
(a) Droplet pins at  $X = 0.7$   $\theta_{eq}^* = 161.98^\circ$



(b) Droplet pins at  $X = 0.85$   $\theta_{eq}^* = 148.29^\circ$



(c) Droplet pins at  $X = 1.0$   $\theta_{eq}^* = 135.23^\circ$



(d) Droplet pins at  $X = 1.15$   $\theta_{eq}^* = 122.57^\circ$

Figure 2.16: Droplet spreading on a topography of pillar width = 0.05 and gap = 0.1 with different initial shape, shows different apparent equilibrium contact angels.

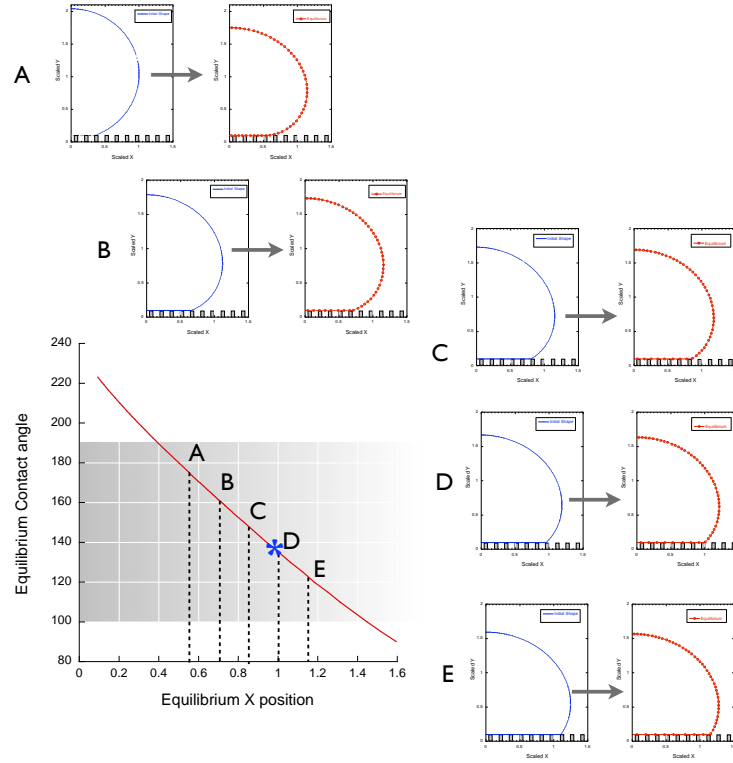


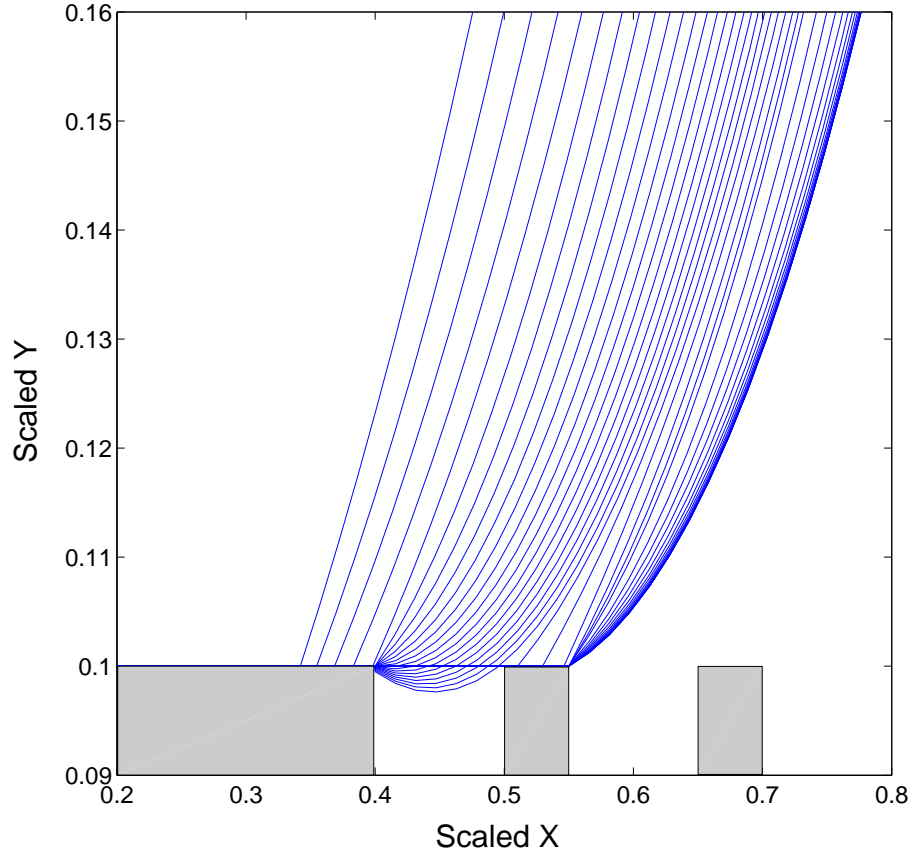
Figure 2.17: Extent of spreading curve for volume  $V_1$ , on which different equilibrium points are plotted for a given surface texture obtained from the dynamics of the spreading problem with different initial shapes. Shaded area shows the range of contact angles possible ( $\theta_{crit,H} \leq \theta_{eq}^* \leq \theta_{crit,V}$ ) for the prescribed intrinsic surface energy of the liquid-solid system  $\theta_{adv}$ . '\*' is the Cassie-Baxter relation predicted apparent contact angle.

spreading and secondly with controlled spreading, i.e. by increasing volume of the droplet gradually with time.

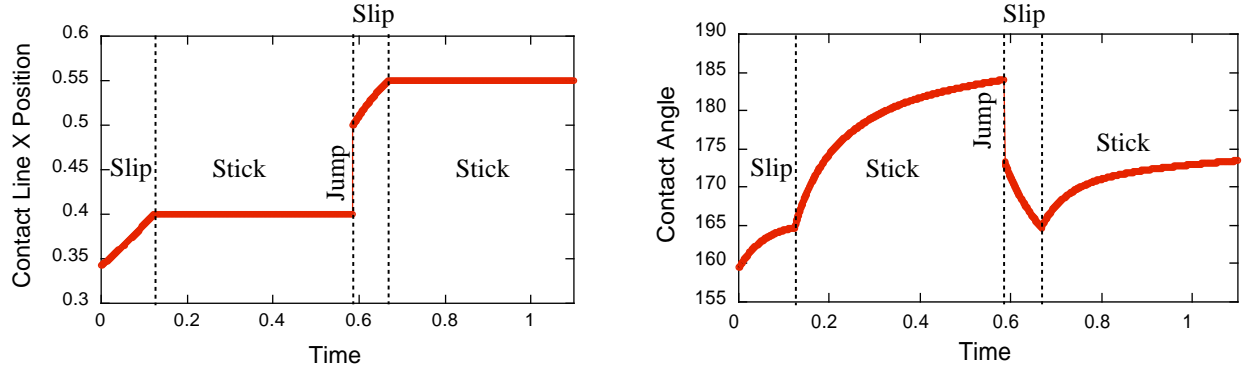
## 2.6.1 Microfabrication and Static Contact Angle Measurements

### Fabrication of Patterned Surfaces

Soft-lithographic technique was used for fabricating superhydrophobic surfaces from PDMS, i.e. poly (dimethylsiloxane). Fig. (2.20) illustrates the major fabrication steps. Microstructures were imposed onto the PDMS by casting it over a master. For preparation of the master from silicon wafer we first clean the wafer with standard technique of series of chemical washes, acetone, iso-propyl alcohol and de-ionized water and blow dried with nitrogen gas. We spin-coated a thin layer of negative-toned photoresist (SU-8 2050, MicroChem Cor-

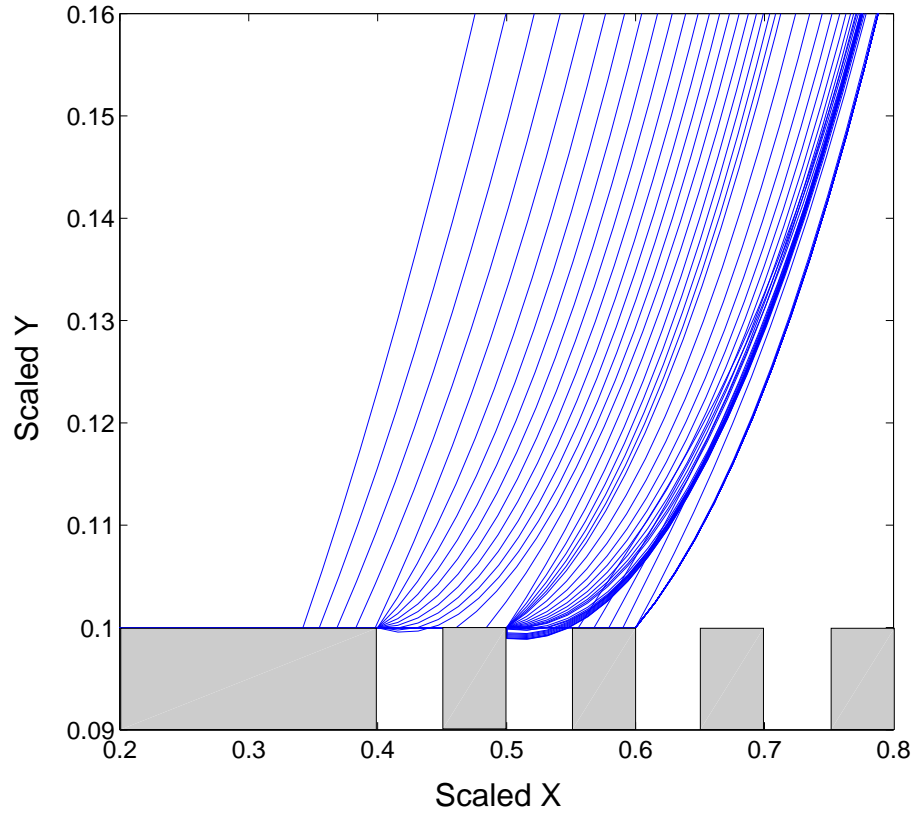


(a) Time evolution of the droplet shape near the contact line region. Droplet achieves a final equilibrium shape at the pinning point located at  $X = 0.55$ .

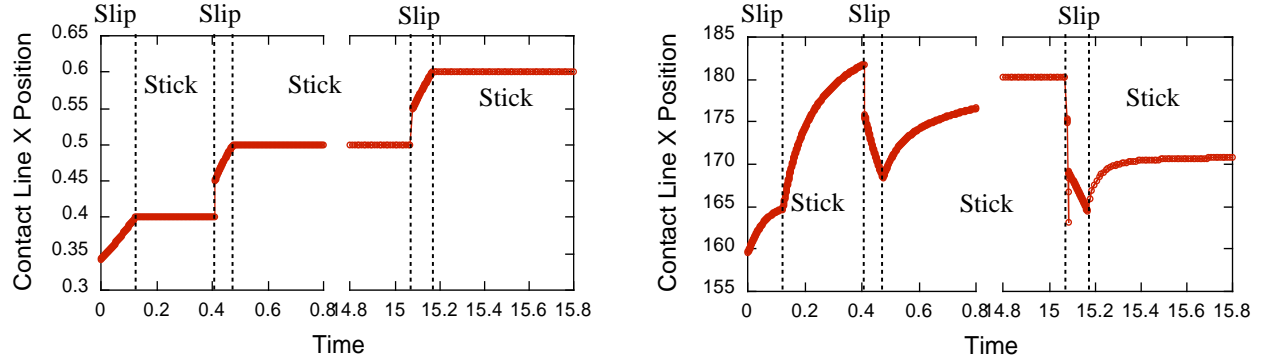


(b) Left hand side plot shows slip-stick-jump motion of the contact line, contact line slips on the horizontal surface, sticks after reaching the corner point and jumps from one pillar to the next. Corresponding dynamic contact angles are plotted on the right.

Figure 2.18: Droplet spreading dynamics over a topography composed of solid width = 0.05 and gap = 0.1 for advancing contact angle of  $90^\circ$ . Liquid starts its downward motion on the first corner point before the interface touches the adjacent pillar.



(a) Time evolution of the droplet shape near the contact line region. Droplet achieves a final equilibrium shape at the pinning point located at  $X = 0.6$ .



(b) Left hand side plot shows slip-stick-jump motion of the contact line, contact line slips on the horizontal surface, sticks after reaching the corner point and jumps from one pillar to the next. Corresponding dynamic contact angles are plotted on the right.

Figure 2.19: Droplet spreading dynamics over a topography composed of solid width = 0.05 and gap = 0.05 for advancing contact angle of  $90^\circ$ . Downward motion of the interface on the second pillar is more clearly seen before the interface touches the adjacent pillar.

poration, Newton, MA) onto a cleaned silicon wafer. The desired film thickness is achieved by tuning the spinning conditions such as rpm, acceleration and spinning time. The silicon wafer along with the SU-8 layer is then baked (pre-exposure bake) over a hot plate before exposing to UV light (at 365 nm) through a transparency mask. High resolution transparency mask were printed from Pageworks, Cambridge, MA, which consist of the negatives of required designs to be patterned on the PDMS surface. Exposing the SU-8 layer, on silicon wafer substrate, to UV light at prescribed exposure energy causes the photoinduced cross-linking reaction and only part of the SU-8 which is exposed through the transparency gets cross-linked. After UV exposure the photoresist layer is baked again on a hot plate (post-exposure bake). Patterns were developed on the master by immersing the wafer in

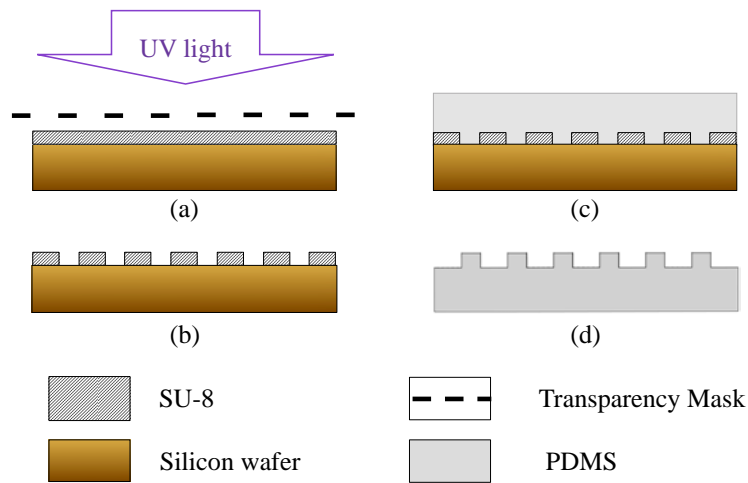


Figure 2.20: Fabrication of patterned PDMS surface: (a) UV-exposure of SU-8 resist through transparency mask, (b) Master prepared after washing off unpolymerized SU-8, (c) PDMS-prepolymer mixture poured over the master and cured in oven, (d) PDMS surface with micro-patterns is obtained after peeling-off from the master.

the developing solution (SU-8 developer, MicroChem Corporation, Newton, MA), to remove uncross-linked SU-8 from the wafer. Optimum parameters for the SU-8 fabrication process (including spin-coating rpm, baking times, UV light exposure energy) are obtained from the datasheet provided by MicroChem corporation<sup>61</sup>. To make the PDMS peel-off easy, the exposed silicon wafer on the master was made hydrophobic by reacting it with perfluorosilane. The surface modification reaction was carried out by dissolving 10 $\mu$ l of (Heptadecafluoro-1,1,2,2-tetrahydrodecyl)trichlorosilane (Gelest Inc, Morrisville, PA)) into 25ml of chloroform and then the master was immersed into the solution. After 2 hours, the master was removed, blow dried with N<sub>2</sub> and heat treated for 20 min at 115°C.

For the the fabrication of the PDMS surface, the PDMS prepolymer mixture is prepared

by mixing the prepolymer with a curing agent (Sylgard 184 Silicone Elastomer Kit, Dow Corning, Midland, MI) in a 10:1 weight ratio. The prepolymer mixture was then thoroughly mixed and defoamed in a centrifugal Thinky Mixer (AR-100, Thinky Corporation, Tokyo, Japan). The PDMS prepolymer mixture was then poured onto the master and trapped air in the patterns was removed by applying vacuum for 30 min. The PDMS mixture was then cured in an oven at 65°C for 2 hours. The PDMS replica was then gently peeled off from the master.

Different structured patterns of PDMS surfaces were prepared like a regular array of square pillars, square holes, and circular pillars. SEM images of the patterned PDMS surfaces were taken (Fig. 2.21) with a Zeiss Evo 40 operated at 10kV. Images were recorded under variable pressure (VP) mode at 40 Pa. Samples were also characterized under an optical microscope to get quantitative data about the structures.

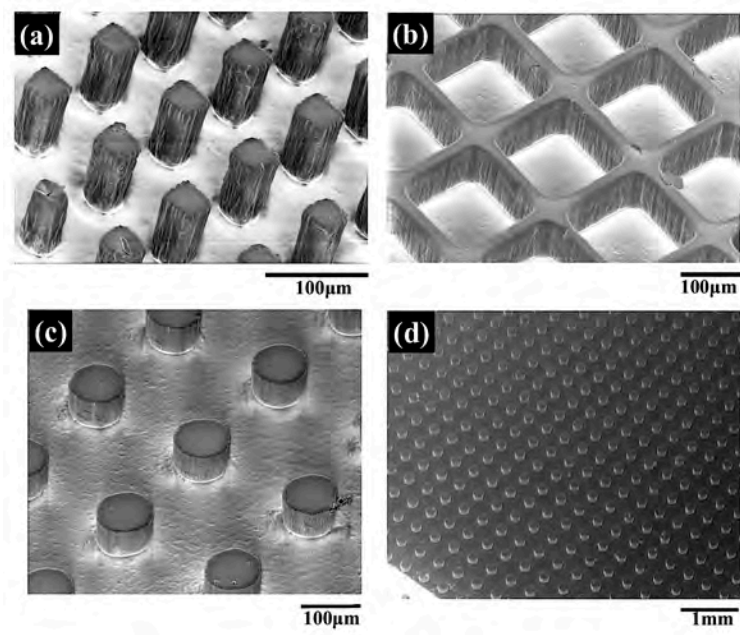


Figure 2.21: Scanning Electron Microscopy images of the fabricated PDMS surfaces: (a) Square pillars (SP), (b) Square wells (SW), (c) and (d) Circular pillars (CP). Scale bar is shown at the bottom-right corner of each image.

## 2.6.2 Contact Angle Measurements

As a measure of the hydrophobicity, water contact angle measurements were performed on different PDMS surfaces. Measurements were performed with deionized water and surfaces were cleaned to remove dust particles simply by blowing nitrogen gas over it. A pendant

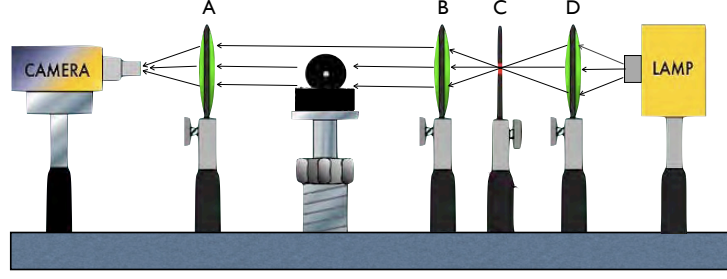


Figure 2.22: Schematics of Video Microscopy apparatus used for imaging the droplets: A, Objective lens; B, collimating lens; C, pinhole; D, focussing lens

Table 2.1: Comparing experimentally observed contact angle with that predicted from Wenzel and Cassie-Baxter theory; where  $a$  is side of a square,  $d$  is diameter of a circle,  $p$  is square pitch, and height  $h = 100\mu m$ .

No.	Surface Topology (in $\mu m$ )	$r$	$\phi_s$ (in%)	$\theta_c$	$\theta_w$	$\theta_{exp}$
1	Flat	1	100	-	-	105
2	SP, $a = 40, p = 100$	2.6	16	151.8	132.3	144
3	SW, $a = 170, p = 200$	2.85	27.75	142.6	137.5	145
4	CP, $d = 110, p = 250$	1.55	15	152.7	113.6	141
5	CP, $d = 130, p = 250$	1.65	21	147.6	115.3	128.4

bubble/sessile drop video microscopy setup was used to image the droplet, from which the contact angle was then obtained. Fig.(2.22) shows the video microscopy setup, in which light is collimated by using a series of optics, and then imaged by a CCD camera which is connected to a computer. Images recorded are shown in the Fig.(2.23) with respective contact angles for a constant droplet volume of  $6\mu l$ . Light coming from beneath the drop is an indication of the Cassie-Baxter kind of wetting and the droplet resting on a composite surface of solid and air. Approximately a  $40^\circ$  jump in the water contact angle was observed between the flat and the roughened surfaces. Table 2.1 compares the experimentally observed water contact angles ( $\theta_{exp}$ ) with the predicted values from Wenzel's approach ( $\theta_w$ ) and the Cassie-Baxter's approach ( $\theta_c$ ). We can see that the experimental values are closer to that predicted by the Cassie-Baxter's relation. This also confirms that the droplet is riding on a composite surface rather than having a fully wetted contact with the solid. In these experiments droplet was placed on the surfaces with a hand-held syringe and even with a little shaky motion of hand it is possible that the droplet contact line is forced to jump/explore the neighboring pillars and thus contact angle is much lower than  $180^\circ$ .

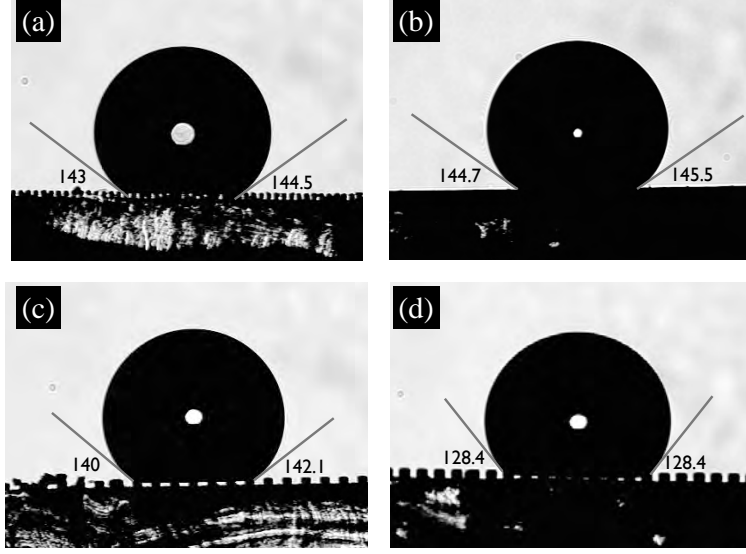


Figure 2.23: Contact angles as measured from the images obtained from video microscopy on (a) Square pillars (SP); (b) Square wells (SW); (c) and (d) Circular pillars (CP).

### 2.6.3 Experimental Results of Droplet Spreading over a Superhydrophobic Surface

#### Gravity driven spreading of a droplet

To study the gravity driven spreading dynamics of a droplet and to have somewhat similar conditions like our simulations, we fabricate 2-D surfaces i.e. surfaces have microstructures in the form of long parallel grooves as opposed to pillars. SEM images of such fabricated anisotropic surfaces are shown in Fig. 2.24. Also, this spreading dynamics is a very fast; for water if we compute characteristic velocity,  $V' = \rho g a^2 / \mu$ , for water  $V' \sim O(10)$  m/s and corresponding Reynolds number,  $Re = a V' \rho / \mu \sim O(10^5)$ . Thus, stokes flow assumption is definitely not valid. Therefore, we use glycerol instead of water because glycerol exhibit very similar contact angles on the flat PDMS surface as that of water ( $\theta_{gly} = 100^\circ$  and  $\theta_{wat} = 103^\circ$ ). The advantage using glycerol over water is that its viscosity is 1.2 Pa.s (1200 times viscosity of the water). Hence, characteristic velocity for glycerol,  $V' \sim O(0.01)$  and corresponding Reynolds number is  $Re \sim O(0.01)$ .

To capture the dynamics of the droplet, glycerol drop was gently touched the solid surface while still attached to the needle and needle was gently pulled up so that the drop snaps off from the needle and spreads under gravity over the parallel grooved surface. Its dynamics is visualized along the transverse direction (perpendicular to the grooves) with a fast video camera capable of capturing few thousand frames per second. Fig. 2.25 shows an experiment



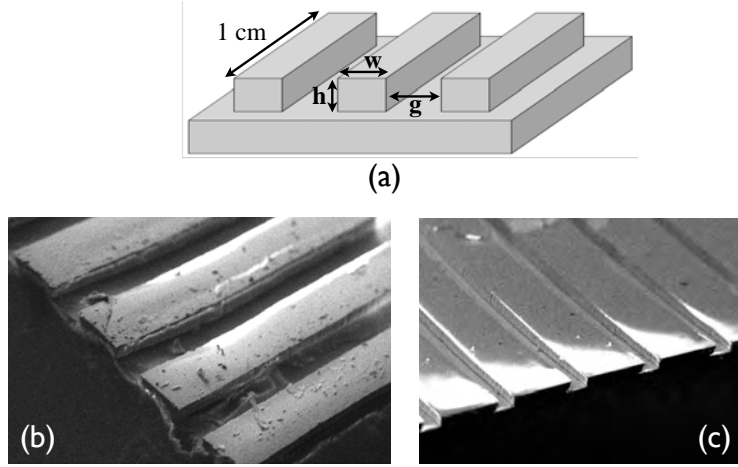


Figure 2.24: 2-D anisotropic parallel grooved/stripped surfaces. (a) Schematic of striped surface with width  $w$ , height  $h$  and gap between the two stripes  $g$ . Length of these stripes is 1 cm, much longer as compared to  $w, g$  and  $h$ . (b) and (c) Scanning Electron Microscopy images with width  $w$  of  $175 \mu\text{m}$  and  $375 \mu\text{m}$  respectively.  $g = 125 \mu\text{m}$  and  $h = 100 \mu\text{m}$  in both cases.

of gravity driven dynamics of glycerol droplet over a grooved surface of solid width  $175 \mu\text{m}$  and gap between the two pillars  $125 \mu\text{m}$ . Images were captured by the fast video camera at 2000 frames/second. Initially at time  $t=0$  s droplet is attached to the needle and touching the top of three solid surfaces and contact line is pinned at the two corners (one on the either sides). During the snap-off process, as the needle was pulled up, interface bends over while still remaining pinned at the same corner points and while doing so interface just touches the neighboring pillar (on the left) at time  $t=0.0175$  s. This initial contact point then becomes the new contact line position and new contact line slips over the top surface of the pillar from time  $t=0.0175$  s to  $t=0.0265$  s, at which time reaches the next pinning point located at the corner of the pillar. After time  $t=0.0265$  s contact line remains pinned (stuck) to the corner point and the contact angle increases till the droplet finally achieves an equilibrium at the new pinning position. During this process neck connecting the droplet with the needle thins and finally breaks. Equilibrium contact angle measured at the end of this process is  $168.3^\circ$ . The light coming from underneath the droplet again indicates the Cassie-Baxter kind of wetting where droplet rests on a composite surface of air and solid. For this surface if we calculate the average solid area fraction in the composite surface, we get  $\phi_s = 0.5833$ . By using Cassie-Baxter relation Eq.2.35, predicted equilibrium contact angle for this  $\phi_s$  is  $\theta^* = 121.19^\circ$ . This clearly indicates that Cassie-Baxter's relation fails to explain such a large equilibrium contact angle. Because droplet while spreading does not see an average solid area fraction of the composite surface but local surface properties. On the other hand, in our

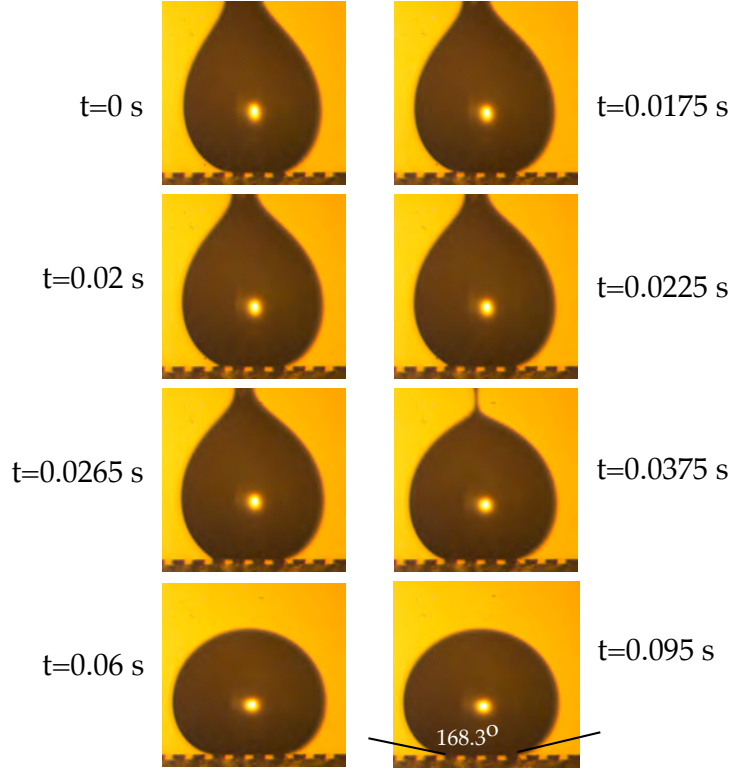


Figure 2.25: Gravity driven spreading motion of a glycerol droplet over a striped surface of solid width  $175\mu\text{m}$  and gap  $125\mu\text{m}$ . Images were recorded by a fast video camera at 2000 frames/sec. Droplet contact line shows distinct slip-stick motion after jumping to the adjacent pillar. Droplet interface touches the pillar on the left and slips over the surface till it remains stuck at the corner point.

simulations we have observed multiple equilibrium contact angles depending upon the initial base radius and for smaller initial base radius we have observed contact angles of about  $170^\circ$ .

Similar experiment of gravity driven spreading is shown in Fig. 2.26 on a grooved surface of solid width  $375\mu\text{m}$  and gap  $125\mu\text{m}$ . This experiment more clearly shows contact line's slip-stick motion after contact line jumps from its initial pinning point to neighboring pillar on the left at time  $t = 0.0417$  s. Images were recorded at 6000 frames/sec. After going through similar steps droplet again comes to equilibrium at the corner point with final contact angle of  $163 \pm 2^\circ$ . Average solid area fraction of the composite surface is  $\phi_s = 0.75$  and Cassie-Baxter relation predicts  $\theta^* = 113.14^\circ$ .

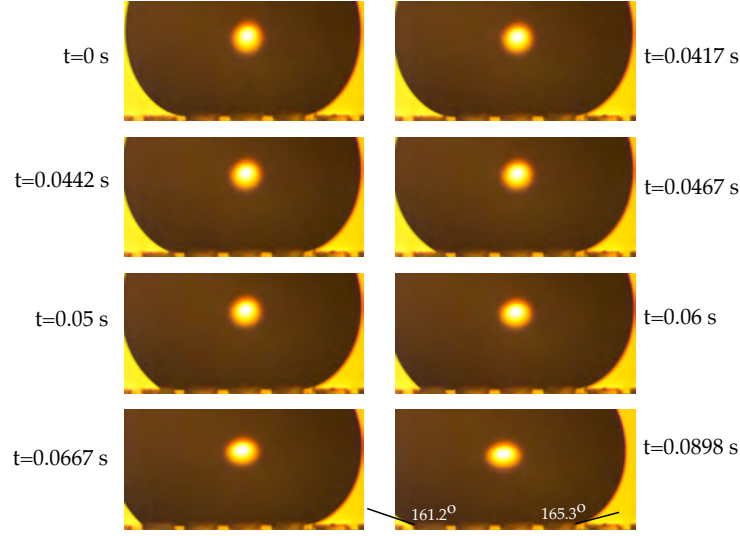


Figure 2.26: Gravity driven spreading motion of a glycerol droplet over a striped surface of solid width  $375\mu\text{m}$  and gap  $125\mu\text{m}$ . Images were recorded by a fast video camera at 6000 frames/sec. Droplet contact line shows distinct slip-stick motion after jumping to the adjacent pillar. Droplet interface touches the pillar on the left and slips over the surface till it remains stuck at the corner point.

### Controlled spreading of a droplet

Slip-stick motion of the contact line is demonstrated in section 2.6.3 where dynamics was too fast and it is captured with a fast video camera. In order to have a closer look at the contact line pinning and available multiple contact angles as well as to minimize the effect of the second curvature in 3-D droplet a controlled spreading experiments were performed. In these experiments droplet contact line does not advance by gravity driven spreading motion but due to increase in volume of the droplet. Experimental arrangement is as follows. Microtextured surface used is again 2-D, parallel grooved surface. Water is used as a liquid in these experiments as by controlling the rate of increase in the volume of the droplet we can still have stokes flow conditions. Volume of a droplet is increased with the help of a syringe pump which pumps the water at a very small rate through a needle which is attached at its end to a rectangular slit arranged above the surface with slit length aligned along the grooves. Water coming out of this slit forms a cylindrical droplet with axis of cylinder parallel to the grooves. This cylindrical shape of the droplet minimized effect of 3-D curvature and resembles more closely with the simulation conditions. Schematic of this experimental arrangement is shown in Fig. 2.27.

Fig. 2.28 shows one such typical experiment where volume of the droplet is increased gradually as the cylindrical drop forms over a surface consisting of stripes of  $275\mu\text{m}$  solid

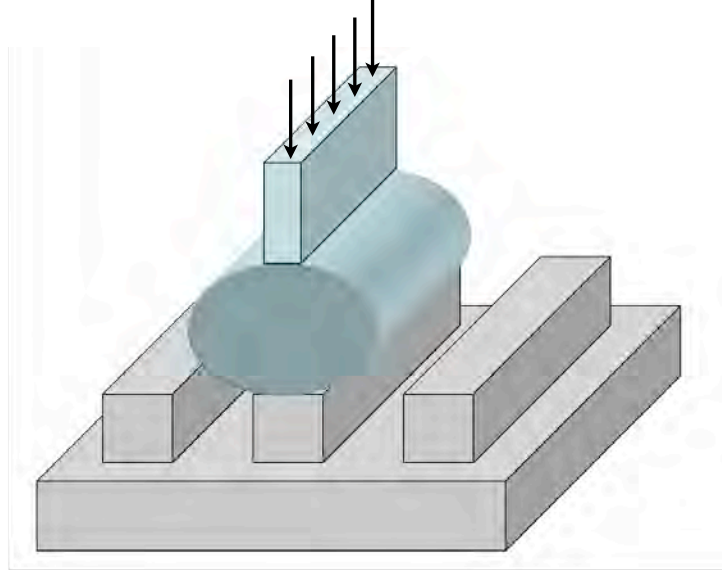


Figure 2.27: Schematic of the experimental arrangement for the controlled spreading of a cylindrical droplet over a parallel grooved surface. Droplet volume is increased by flow coming in through the slit.

width and  $125\ \mu\text{m}$  gap. Flow rate to the droplet was maintained at  $15\ \mu\text{l}/\text{min}$  and droplet spreading is observed in a transverse direction through a CCD camera. Camera is focused in the middle of the cylindrical droplet in order to avoid any end effects and as a result the surface topography appears blurred or washed out. (When camera is focused on the front end of the surface topography looks very sharp, as in the previous results of gravity driven spreading.) Images were captured at the rate of 1 frame/sec. Figure shows time dependent droplet shape in the vicinity of the contact line, which is initially pinned at a corner point. When the flow into the droplet is started contact line remains pinned at the same location, however rest of the droplet is free to move and as a function of time droplet goes through multiple contact angles from  $157^\circ$  till very close to  $180^\circ$  after 47 sec where the free interface just touches the next pillar. As soon as the interface touches the neighboring pillar on the left, contact line quickly slips and sticks to the downstream end of the corner point within a second where contact angle is again about  $157^\circ$  and the process continues. Fig. 2.29 shows a very similar experiment on a surface with topography of solid stripes width  $175\ \mu\text{m}$  and gap between the stripes  $125\ \mu\text{m}$ . In this experiment flow rate through the slit was maintained at  $10\ \mu\text{l}/\text{min}$  and images were captured at 1 frame/sec. These two experiments clearly confirms the presence of sharp pinning points and droplet can achieve any contact angle from the range permissible.

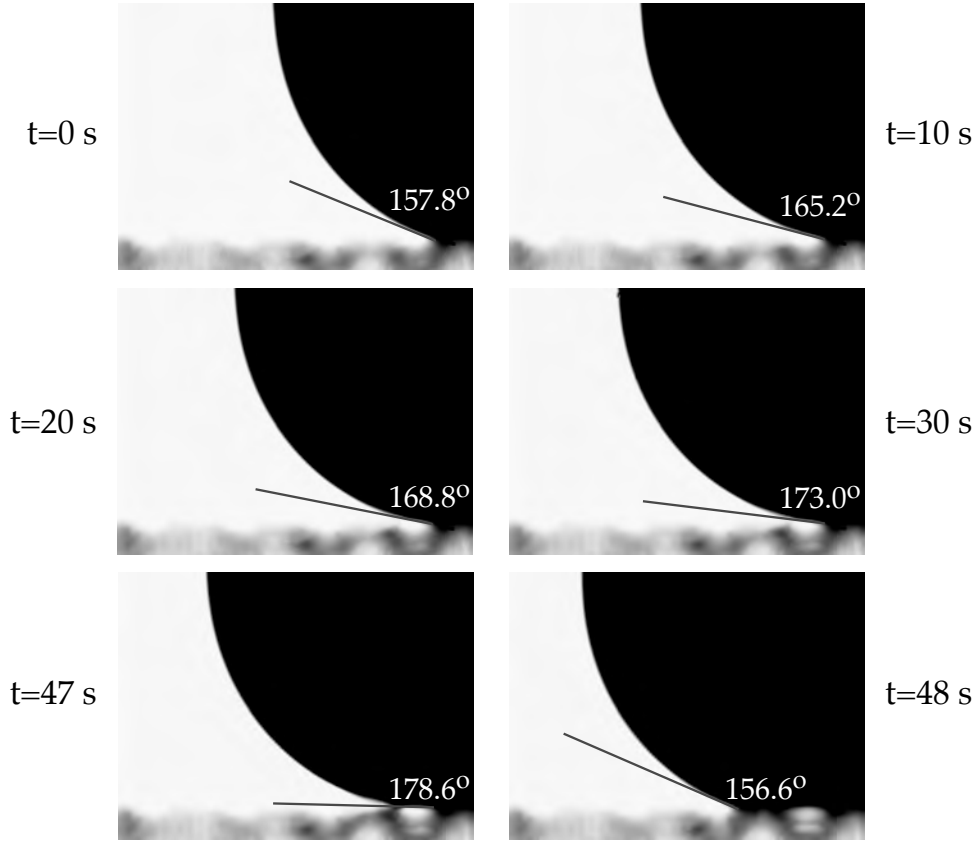


Figure 2.28: Controlled spreading of a 2-D droplet over a striped surface with  $w = 275\mu\text{m}$ ,  $g = 125\mu\text{m}$  and  $h = 100\mu\text{m}$ . Flow rate through the slit =  $15\ \mu\text{l}/\text{min}$ , frame capture rate = 1 frame/sec. Droplet shows pinning at the corner point while its contact angle increases till time  $t=47$  sec at which time the contact line jumps to the next pillar.

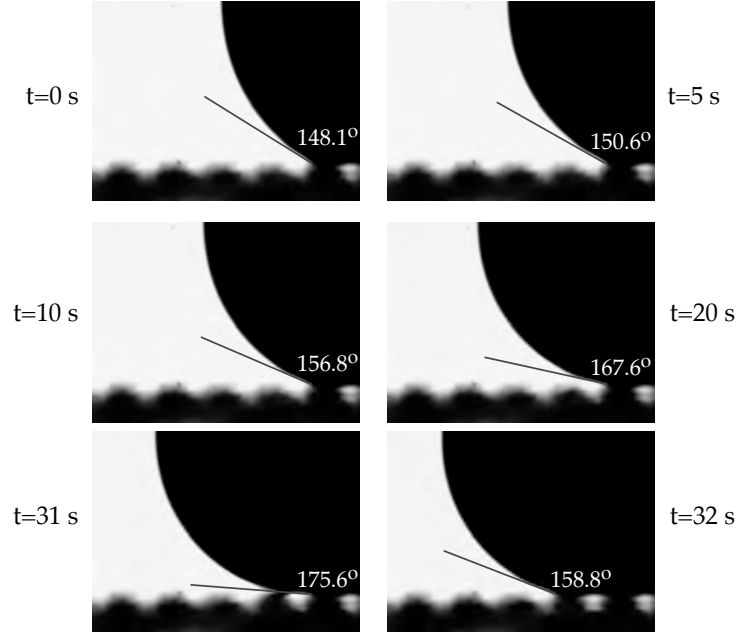


Figure 2.29: Controlled spreading of a 2-D droplet over a striped surface with  $w = 175\mu\text{m}$ ,  $g = 125\mu\text{m}$  and  $h = 100\mu\text{m}$ . Flow rate through the slit =  $10\ \mu\text{l}/\text{min}$ , frame capture rate = 1 frame/sec. Droplet shows pinning at the corner point while its contact angle increases till time  $t=31$  sec at which time the contact line jumps to the next pillar.

## 2.7 Conclusion

From our numerical simulations, what we see is the superhydrophobicity is attributed to the nature of the pinning points and the final equilibrium contact angle is dependent upon where the pinning points are located. Closer the distance of the final pinning point to the axis of symmetry, for a given volume, larger is the observed equilibrium contact angle. Once the droplet attains equilibrium at a corner, it doesn't know the presence of the pinning points which are ahead of the contact line. In our simulations, we also observe very large equilibrium contact angles, much larger than those predicted by Cassie-Baxter equation for similar surface features. Major difference between the two is that Cassie-Baxter equation is dependent upon effective surface properties while our hydrodynamic model is based on the interaction of fluid droplet contact line with local topography of the surface. On the textured surface there are number of equilibrium shapes of the droplet are possible at different pinning locations with corresponding contact angles. Final equilibrium shape attained by the droplet is based on the history of the droplet, i.e. how droplet achieved that equilibrium. When droplet spreads on the surface with a very small initial base radius, it first sees pinning points that are close to the symmetry axis and hence final equilibrium contact angle obtained is

larger. If for some reason (often in experiments due to inertia and relative motion of the depositing needle with the surface) the droplet initially starts spreading with a larger base radius, then as it spreads it will come across the pinning points that are ahead of the initial base radius. In that case, droplet will be pinned at a farther distance from the symmetry axis and for a given volume, it will achieve lower equilibrium contact angle corresponding to the location of the corner point. Thus apparent equilibrium contact angle achieved is dependent on location of pinning points, volume of the droplet, and history of the droplet spreading.

Superhydrophobic surfaces, of PDMS material, consisting of regular array of pillars were fabricated using soft-lithography technique. On 2-D array of posts and pores, a water droplet placed clearly shows Cassie-Baxter kind of wetting and measured water contact angle value also fairly matches with the predictions from the Cassie-Baxter relation. Water droplet placed on these surfaces, from a hand-held syringe, were associated with large oscillations due to inherent inertia of the depositing and droplet snap-off process. This oscillations causes the droplet to overshoot local minima and arrive at an equilibrium which is closer to the global minimum, i.e. near Cassie-Baxter equilibrium. However, when droplet is more carefully placed and is of higher viscosity, inertial effects are quickly damped and droplet motion is arrested at the first local minimum available. Dynamics of these viscous droplets studied with a fast video camera reveal the same slip-stick motion (in agreement with the simulations) of the contact line and droplet achieves equilibrium while remaining pinned at a downstream end of the post of 1-D parallel grooved surface. Observed apparent equilibrium contact angle is much larger than the Cassie-Baxter prediction as the droplet remains pinned in the local minimum. Similarly, controlled spreading experiment reveals multiple contact angles provided by the corner point before the contact line jumps to the next available pillar. And the droplet interface indeed makes a contact angle near  $180^\circ$  before it advances to the next pillar. These observations are consistent with our numerical simulations and reiterate the fact that wetting is a dynamic phenomena and equilibrium droplet contact angle on a textured surface is dependent upon the history of the droplet as well as available local minima in the form of pinning points.

## Chapter 3

# Hydrodynamics of Water Droplet Movement in Oil over Particle Microtextures Impregnated With Oil to Reduce Droplet Adhesion

### 3.1 Background

This research is a fundamental study on texturing a surface, so that, when the surface is submerged in a hydrocarbon (oil) phase, the adhesion of water droplets in the oil to the surface is low, and the mobility of the droplets along the surface is high. The rationale for the study is based on the lotus leaf paradigm or super hydrophobic effect (see the previous chapter and the references<sup>1-19</sup>), in which water droplets in air placed on a hydrophobic textured surface are observed to be nonadherent, and to easily roll off the surface. The water droplet does not penetrate into the texture due to the hydrophobicity, and instead beads-up on the surface, and under a lateral force (e.g. gravity), glides along the tops of the texture. As reviewed in these references, techniques for the materials fabrication of surfaces with the required hydrophobic texture have been developed, and have been applied to many applications, in drag reduction and de-icing, and as anti-sticking, anti-fouling surfaces and self-cleaning surfaces. Virtually all of the research has centered on water droplets or water flow over textured surfaces in air. We study here how this interfacial physics can be applied to design surfaces which, under oil, allow water droplets to be non-sticking and interfacially mobile. A primary application of surfaces which are repellant to water droplets in oil, and which motivates our work, is to prevent corrosion of surfaces in oils due to water droplet



adhesion as for example in oil pipelinning.

We provide first a brief background on the rationale for using superhydrophobic surfaces under oil to reduce the adhesion of water droplets in the oil to the surface, and increase their mobility along the surface. We then detail our preliminary progress on fabricating nano and micro-textured surfaces through particle assembly, and our contact angle measurements (advancing, receding and static) which verify that water droplets are non-adhesive on these surfaces. Finally we detail our measurements of the gliding (rolling-off) motion of the drops under oil over particle-textured surfaces, in which the surfaces are tilted to force the droplet motion.

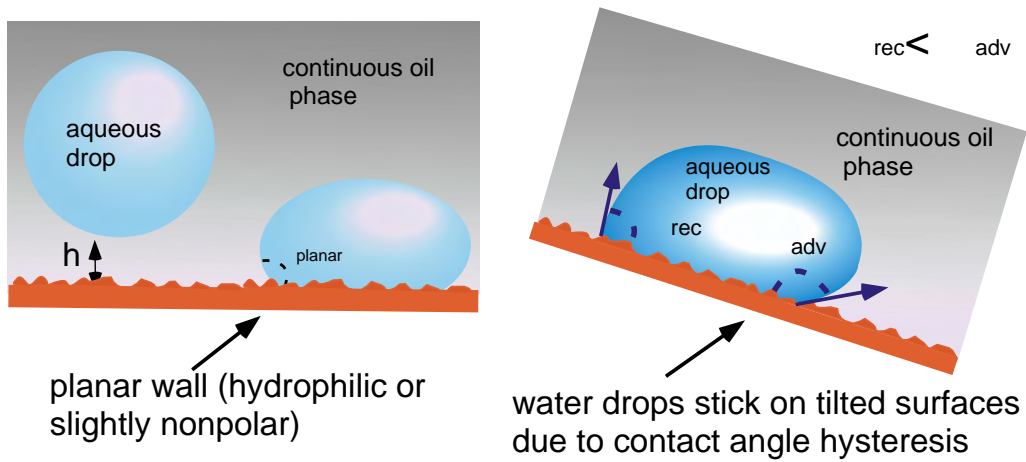


Figure 3.1: A water droplet in a hydrocarbon oil, separated by a thickness  $h$  from a wall with a planar surface, settles to the wall surface where it sticks with a finite contact angle  $\theta_{planar}$  on a surface that is polar or slightly hydrophobic. The surface is nominally flat with a surface roughness. Due to contact angle hysteresis, the droplet remains stuck when the interface is inclined, or moves with a retarded motion.

For illustration, in Fig. 3.1 is shown a water droplet (of order 1-100  $\mu\text{m}$  in (equivalent) spherical diameter), entrained in the flow of a continuous oil phase in a channel viewed in cross section. Buoyancy forces, owing to density differences between the water and oil phases, bring the droplet in the vicinity of a channel wall. As gravity presses the droplet against the wall, it drains the oil in the gap between the droplet and the surface, and flattens the fluid interface to create a thin intervening film of oil which can rupture and adhere the droplet to the surface (for reviews see, for example,<sup>62–67</sup> for film stability and<sup>22,68–70</sup> for surface wetting). Adhesion occurs when the surface is polar enough so that  $\gamma_{w/s} < \gamma_{o/s} + \gamma_{w/o}$  (where  $\gamma_{o/w}$  is the oil/water fluid tension and  $\gamma_{w/s}$  and  $\gamma_{o/s}$  are the water/solid and oil/solid surface energies) and the balance of tensions at the contact line insures a finite contact angle ( $\gamma_{w/s} = \gamma_{o/s} - \gamma_{o/w} \cos \theta_{eq}$ , where  $\theta_{eq}$  is measured through the water phase). This is the

usual case in oil contacting equipment, where the interfaces are usually polar, e.g. stainless steel. When the drop attaches with a finite contact angle ( $\theta$ ), the contact line perimeter can immobilize the drop because of contact angle hysteresis due to surface roughness<sup>20–22</sup>, Fig. 3.1. In order for the drop to move along the surface, the interface at the advancing perimeter has to deform to a larger contact angle than the equilibrium, and the trailing perimeter to a smaller angle (cf. the discussion in the previous chapter). Continuous phase stresses above a critical value can move the droplet (see for example<sup>71–73</sup>); however, even in this case, the drop mobility is retarded by this hysteresis and usually moves in a slow, episodic, jerky motion.

As discussed earlier, a superhydrophobic surface in air is a textured interface in which the texture can be regular (e.g. pillars or wells) or random (as for example textures obtained by etching, polymer adsorption or particle coating). The texture is required to be hydrophobic (either the texture material is hydrophobic, or the texture surface is modified with a hydrophobic coating). Because of this hydrophobicity, when a water droplet is placed on top of the surface in air, it does not penetrate into the texture, but resides over a cushion of air, forming a contact line periphery on the surface by pinning to the texture edges (“Cassie-Baxter” wetting)<sup>1–19</sup>. This pinning results in a contact angle ( $\theta^*$ ) which is much larger than the contact angle ( $\theta$ ) of a water droplet on a smooth surface of the texture material (or a smooth surface with the same hydrophobic coating). Thus the droplet contact area on the superhydrophobic surface is reduced relative to the smooth surface. A simple expression for the larger contact angle, in general agreement with data, is based on minimizing the fluid and solid energies, and is given by the Cassie-Baxter equation  $\cos \theta^* = (1 + \cos \theta)\phi_S - 1$  where  $\phi_S$  is the area fraction of the solid. Hence for an area fraction of  $\phi=.1$  and a contact angle of  $\theta=90^\circ$ , for example, an angle of  $\theta^*=150^\circ$  is subtended on the superhydrophobic surface. A second feature of the Cassie-Baxter wetting state is that water droplets in air can glide over the surface. Measurements of contact angle hysteresis on superhydrophobic surfaces show that microtextures of posts in particular (in contrast to wells) have small contact angle hysteresis which tends to zero as the area fraction tends to zero<sup>23–28</sup>. In the case of posts, the advancing and receding menisci move similarly over the tops of the posts, and hysteretic effects only arise from differences in motions over the solid surfaces, which become reduced as  $\phi \rightarrow 0$ . The receding meniscus over wells moves along the matrix around the wells, while the advancing meniscus jumps over the wells leading to a larger hysteretic effect. Within the drop, the viscous frictional resistance as the liquid moves along the surface is also reduced because of the air cushion. This motion is characterized by a slip coefficient  $\lambda$  defined as  $\mathbf{u} \cdot \mathbf{t} = \lambda \mathbf{n} \cdot \{\nabla \mathbf{u} + \nabla \mathbf{u}^t\} \cdot \mathbf{t}$  where  $\mathbf{u}$  is the velocity,  $\mathbf{n}$  and  $\mathbf{t}$  are the unit normal and tangent vectors to the surface,  $\nabla \mathbf{u}$  is the rate of strain tensor (evaluated at the surface) and

$\lambda \rightarrow 0$  describes the usual no-slip condition. While slip coefficients are usually of the scale of nanometers, for superhydrophobic surfaces the slip coefficient can exceed microns<sup>34,74–76</sup>.

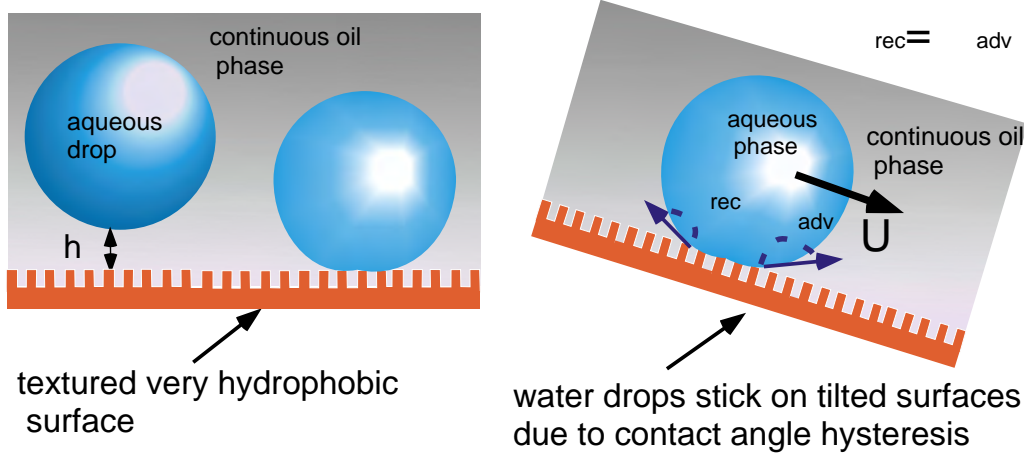


Figure 3.2: Superhydrophobicity and Cassie-Baxter Wetting: (a) microtextured hydrophobic surface of posts under oil is impregnated by the oil, and water droplet on the surface subtends a large contact angle because of the pinning of the interface to the geometry as is the case in air. More importantly contact angle hysteresis is eliminated because of the reduced contact of the water with the solid surface of the texture and the drop glides over the texture and does not adhere.

We extend the concepts of Cassie-Baxter wetting and superhydrophobicity to develop surfaces which allow water droplets in oil and in contact with the surface to move more smoothly over the interface, rather than sticking and (or) moving episodically. In this way, the droplets have no residence time on the surface of the wall as they are flushed downstream with the flow, and this should prevent nucleation phenomena initiated by stagnant drops on surfaces, such as corrosion. A textured hydrophobic surface immersed in oil allows a water droplet to rest on the surface with the oil impregnating the texture underneath the water, Fig. 3.2 and a large contact angle is achieved ( $\theta^*$ ) as the contact line is pinned to the texture. The static and dynamic behavior of such droplets have not been studied as extensively as the superhydrophobic configuration in air. But most importantly, a significant reduction in the contact angle hysteresis relative to a smooth surface should be realized (for posts in particular), again because the interface drags over the posts in a similar manner whether advancing or receding in oil or air. We also note that, within the droplet, while the friction of the aqueous phase moving along the saturated microtextured surface is reduced because of the liquid held in the structure, the effective slip generated (as measured by the slip coefficient) is not as great as occurs when the texture is filled with air. The principal effect that the Cassie-Baxter wetting affords as drops move in oil over the oil-saturated microtexture is an elimination of the contact angle hysteresis. We note that Aizenberg et al<sup>77</sup>

and Varanasi et al<sup>78</sup> in designing alternative superhydrophobic surfaces for allowing water droplets to move unimpeded over a surface in air have also used hydrophobic microstructures saturated with an oil, which in air supports a thin film of oil over the surface. Droplets in air then ride over this thin lubricating layer, rather than on the solid surface; the difference with the study here is that the water droplets are completely submerged in oil.

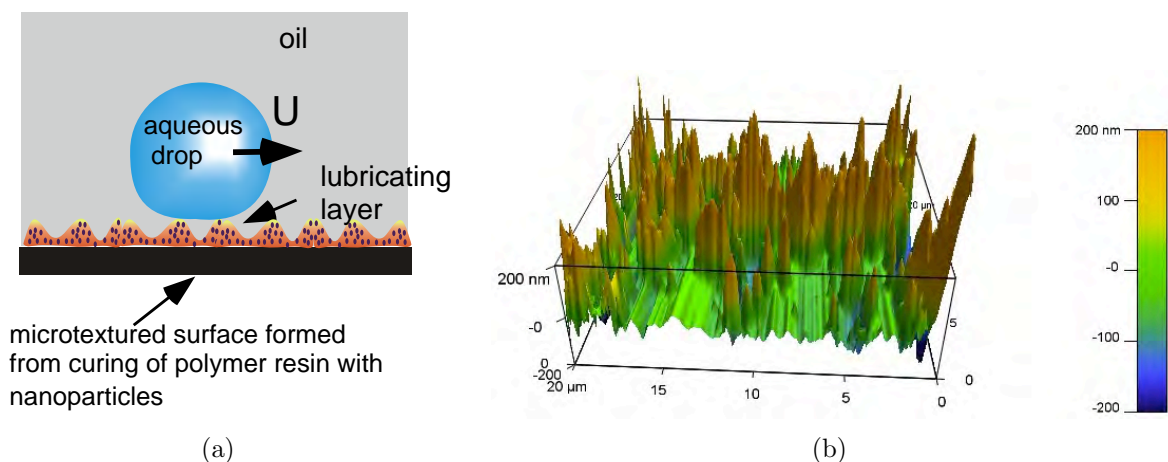


Figure 3.3: (a) A mixture of nanoparticles and binder cures to form a microtextured surface (b) Atomic force microscopy image of the particle surface in tapping mode.

## 3.2 Microtexture Fabrication Using Nanoparticles

To fabricate the textured surfaces, we disperse particles in a polymer resin, coat thin layers of the mixture on a substrate, and then cure the polymer resin. If the volume fraction of the particle relative to the polymer is large enough, then as the resin cures a roughened surface forms from the thin coats of the mixture which functions as they have a hydrophobic texture (Fig. 3.3(a)). This method for texturizing the surface is scalable, allowing for large surface area modification. Hydrophobically modified spherical silica nanoparticles, 20-30 nm in diameter, were first dispersed in a mixture of tetrahydrofuran (THF) and isopropyl alcohol (IPA) (40.60 v/v) at a concentration of 10 mg/ml by sonication. After dispersal, 150 mg of methylphenyl silicone resin binder (Momentive Performance Materials, SR355S) was dispersed in the mixture and sonicated. After sonication, the mixture was diluted with fresh THF/IPA. To coat a substrate with this mixture, cleaned glass slides were vertically dipped and withdrawn from the mixture at a velocity of 10 cm/min using a dip-coater over repeated cycles to coat the glass slide with the resin. After coating the sample was put in an oven at 40°C for 10 min to cure the resin binder. The important consideration in this study

is that the nanoparticle/binder adhere strongly to the surface so that the impregnating oil does not remove them. For this purpose, typically six cycles of dip-coating are required. In Fig. 3.3(b) are shown atomic force microscopy topology images in tapping mode of the surface made with six dip-coats after curing. The topology shows peaks and valleys of the order of a few hundred nanometers, and lateral variations along the surface of a few microns.

### 3.3 Equilibrium Contact Angles in Air and Under Oil

Equilibrium contact angles ( $\theta_{eq, texture}$ ) of water and oil droplets on the fabricated microtextured surfaces in air, and water droplets under oil are undertaken using standard contact angle goniometry to measure the angle directly from video images of sessile drops. Fig. 3.4(a) shows a side view of a water droplet in air on the textured surface; contact angles equal to  $165^\circ$  are recorded. When a droplet of oil (hexadecane) is placed on the surface, the hydrophobic nature of the texture allows the oil to infuse into the texture. The interface becomes oleophilic and a contact angle of approximately  $8^\circ$  is measured (Fig. 3.4(b)). Finally a water droplet placed on the surface under hexadecane shows a large contact angle, also approximately  $160^\circ$  (Fig. 3.4(c))

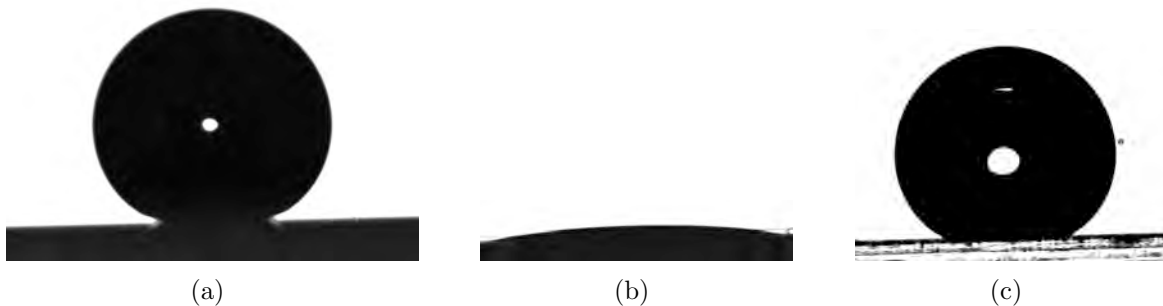


Figure 3.4: (a) A water droplet in air on the nanoparticle microtexture, (b) a hexadecane oil droplet in air on the microtexture, and (c) an equilibrium water droplet under hexadecane on the texture.

The low contact angle of the oil droplet on the surface in air suggests the oil is wetting into the microstructure, and the large contact angles of the water droplets in oil indicate a Cassie-Baxter wetting state since the contact angles of water on methyl silanated surfaces are typically  $140^\circ$  in oil. We have also measured the contact angle hysteresis of water droplets on these surfaces and find them only to be a few degrees, also confirming a Cassie-Baxter wetting state, in contrast to water drops in oil on a planar silanated surface of approximately 15 degrees. A clear demonstration of the mobility of the nanoparticle textured surface to water droplets in oil is shown in Fig. 3.5, in which a water droplet is released onto an inclined

surface and easily rolls on the surface.

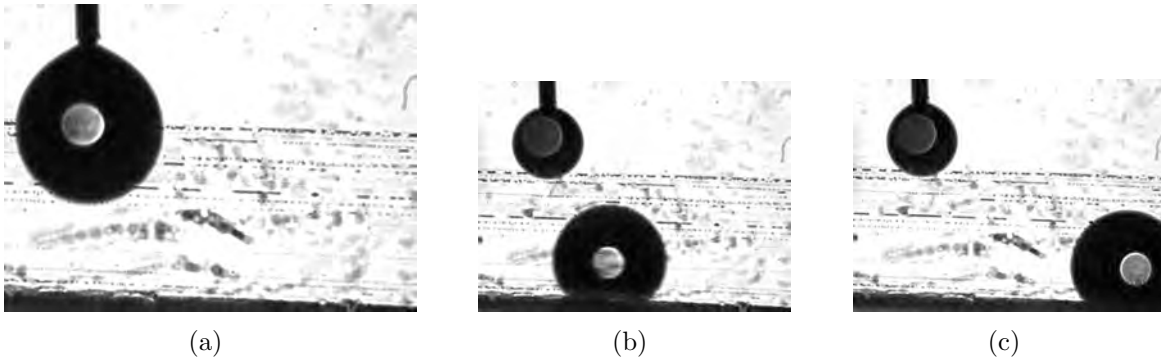


Figure 3.5: Movement of a water droplet under hexadecane along a surface inclined a few degrees. The droplet is a few hundred microns in diameter

# Chapter 4

## Hydrodynamics of Large Interfacial Slip at Porous (Air-Permeable) Polymer Surfaces For Drag Reduction

### 4.1 Introduction

Recently, new attention<sup>79</sup> has been paid to the possibility of hydrodynamic slip at an interface between a stationary solid surface and a “simple” (non polymeric) liquid moving over the surface. The consideration of boundary slip began long ago with the continuum level formulation of the Navier slip condition for a Newtonian fluid which equated the fluid velocity tangent to the surface,  $v_s$ , to the boundary tangential stress,  $\tau_s$ , by the slip coefficient  $\lambda$ , i.e.  $v_s = \frac{\lambda}{\mu} \tau_s$  where  $\mu$  is the fluid viscosity and  $\lambda$  has units of length. Since this formulation, experimental studies have made clear that the “no-slip” condition of  $\lambda = 0$  is sufficient to accurately model most macroscopic flows with length scales in the range of millimeters to meters. However, recent molecular dynamics simulations on atomically smooth surfaces have demonstrated slip on the molecular scale, and calculated  $\lambda$  as a function of the strength of the liquid-solid interaction<sup>80,81</sup>. For strong liquid-solid interactions which characterize complete or strong wetting of the liquid on the solid surface, slip lengths are of the order of only a few molecular diameters ( $O(1 \text{ nm})$ ), while relatively weaker interactions of partially wetting fluids have slip lengths extending tens of diameters ( $O(10 \text{ nm})$ ). Current tools for measuring  $\lambda$  include particle image velocimetry (PIV), image velocimetry enhanced with evanescent near-field illumination at the surface, and atomic force microscope (AFM) and surface force apparatus (SF) measurements.<sup>82</sup> Several experiments are consistent with the MD calculations. For smooth surfaces of a wetting liquid, e.g. water flowing along a

hydrophilic surface, either zero slip or coefficients less than a few nanometers are recorded, while water over a partially wetting hydrophobic surface (e.g. self assembled octadecyl silane (OTS) monolayers) obtain slip lengths of tens of nanometers, e.g.<sup>83–86</sup>. For nonpolar liquids wetting smooth hydrophobic surfaces (the weakest liquid/surface interactions), slip lengths are of the order of a few tens of nanometers<sup>87–89</sup>.

“Giant” slip ( $\lambda$  order 1  $\mu\text{m}$  or larger) is the subject of great interest for its application to reducing surface friction in micro and nanofluidic channel flows. Large slip can be achieved when low friction air layers are situated between the liquid and the surface a circumstance which arises when a population of nanoscopic gaseous domains adhere to a surface, or air becomes trapped in a micro or nano-textured surface that is not wet by the liquid (superhydrophobicity).<sup>90</sup> AFM studies have provided direct evidence of nanoscopic gaseous domains, primarily at the interface between water and a hydrophobic surface.<sup>91</sup> AFM measurements have also verified the reduction in surface friction<sup>92</sup>, and nanoscopic gas domains have been suggested<sup>93</sup> as one reason why some measurements of slip at the water/hydrophobic solid surface<sup>94,95</sup> obtain one micron or larger slip lengths. Hydrophobic, textured surfaces filled with air provide a more reproducible method for generating large slip,<sup>96–99</sup> and theoretical MD and continuum studies of model textures (see for example<sup>100,101</sup>) demonstrate that large slip requires the solid fraction of the surface to be a few percent.

Little attention has been paid to obtaining giant slip when nonpolar liquids slip over a surface (“oil slippery surfaces”), although significant interest is developing due to the emergence of dropwise microfluidic platforms which are based on water droplets moving in a continuous oil stream<sup>102</sup>. Generating gaseous domains at the surface is the key to large slip, and one method for generating a significant coverage of nanobubbles on surfaces submerged in oil is to nucleate them spontaneously on oil contact. Spontaneous nonequilibrium formation of nanobubbles at a surface occurs, for example, when an air saturated liquid (e.g. ethanol) is displaced by a second, miscible, liquid (e.g. water), also saturated with air, but with a lower solubility<sup>91</sup> and nanobubbles nucleate to accommodate the reduced solubility of the displacing phase. In this letter we demonstrate that a nanoporous, hydrophobic polymer, polydimethylsiloxane (PDMS), which has a significant permeability to air because of the hydrophobicity of the polymer and a relatively large free volume<sup>103</sup>, permits oil to slip over its surface with an order one micron slip length. When oil contacts the surface of an air-equilibrated PDMS substrate, air is released as nanobubbles to the oil/PDMS surface. The driving force for this release derives from the fact that the PDMS is also permeable to oil because of its hydrophobic nanoporosity, and diffusion of oil into the nanopores on the



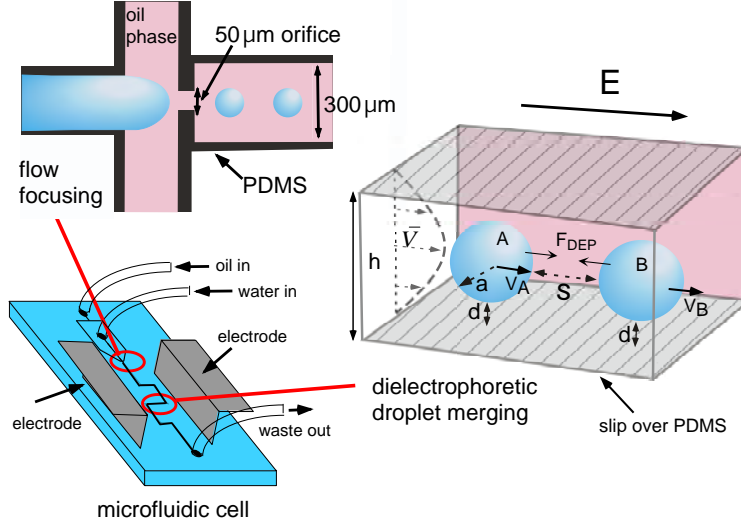


Figure 4.1: Measurement of microchannel slip at an oil/PDMS surface by observing the dielectrophoretic merging of water droplets in oil moving in close proximity to the PDMS channel wall.

contact of oil to the surface displaces the air to the interface.

We demonstrate in particular oil slip at the inside surface of a microchannel formed in a PDMS monolith fabricated by soft lithography. We use a viscous mineral oil ( $\mu_{oil}$  approximately  $10^2$  times that of water), a mix of high and low molecular weight olefins, which does not macroscopically swell the PDMS<sup>104</sup> and distort the surface from the atomically smooth topology normally evident in AFM measurements but can still displace air in PDMS by the solubilization of small linear alkanes in the oil.

## 4.2 Experimental Measurement of Droplet Approach

The microfluidic arrangement is shown in Fig. 4.1. (Additional details are given in the Appendix A.) Using optical microscopy, we measure, in a PDMS channel of rectangular cross section with height  $h$  ( $100 \mu\text{m}$ ) and wide width  $w$  ( $300 \mu\text{m}$ ), the edge-to-edge separation distance ( $s(t)$ ) of pairs of nearly occluding water droplets (“A” and “B”) which are entrained in a mineral oil stream and are driven together by a dielectrophoretic (DEP) force of attraction,  $F_{DEP}$ . This force is due to an electric field  $\mathcal{E}$  applied parallel to the bottom wall of the channel and along the flow direction. The merging droplet pair is part of a single file droplet train, formed upstream by flow focusing<sup>105</sup> of oil and water streams (flow rates equal to  $0.4\text{-}1 \mu\text{l}/\text{min}$  and  $0.04\text{-}0.1 \mu\text{l}/\text{min}$ , respectively), through an orifice  $50 \mu\text{m}$  in width. The

focusing forms droplets with radius  $a$  equal to approximately  $40\text{ }\mu\text{m}$ , which are separated by a few radii, and flow at the average stream velocity  $\bar{V}$  of approximately  $250 - 500\text{ }\mu\text{m}/\text{sec}$ . The electric field is applied to switchback flow lanes at the downstream end of the chip by a voltage  $\mathcal{V}$  set across parallel copper strip electrodes inserted through the PDMS (a dielectric) to insure a uniform field across the flow channels. Relative to the aqueous phase which is de-ionized water, the oil is nonconducting and the field polarizes each of the droplets of the pair into dipoles. In the flow lanes parallel to  $\mathcal{E}$ , the polarized drops are aligned with  $\mathcal{E}$  and attract each other, creating the dielectrophoretic force. Prior to the application of the field, the train flow is observed, and when a pair are observed to pair-off to a relatively close separation (less than one radius) due to flow disturbances, the field is applied to merge the pair, and a video recording is made with a high speed camera. At the time of application of the field, the droplets, heavier than the oil ( $\rho_{water}=10^3\text{Kg}/\text{m}^3$  and  $\rho_{oil}=8.75\times 10^2\text{Kg}/\text{m}^3$ ) have settled to a separation distance  $d$  from the bottom wall of the microchannel which is determined by their settling velocity and the transit time,  $\tau$ , from their formation at the orifice until application of the field and is of the order of a few hundred nanometers. At these distances from the wall, the approach velocity  $V_A - V_B = \frac{ds}{dt}$  due to the DEP force is affected (as we show by numerical solution of the hydrodynamic equations) by the drag, against the bottom wall, of the intervening oil between the droplet and the wall, and the slip on this wall. From comparison of  $s(t)$  with numerical solutions,  $\lambda$  is obtained with a precision which can distinguish a micron size slip length. We also measure the slip when the bottom surface is a glass slide, functionalized with octadecyltrichlorosilane (OTS), which we do not expect to nucleate nanobubbles at the surface because of low air permeability, and we find zero slip to the precision of the measurement.

One illustrative data set is given in Fig. 4.2 An edge detection routine is used to determine the droplet perimeters from which the size of the merging droplets  $a$  and the pair separation distance  $s(t)$  are computed. The separation distance is shown in Fig. 4.2, and the relative approach velocity is approximately  $40\text{ }\mu\text{m}/\text{sec}$ . To obtain different data sets of  $s(t)$  corresponding to different droplet radii or droplet-wall separations  $d$  (transit times  $\tau$ ), the oil and water flow rates at the flow focusing orifice are changed, or the merging at different switchback lanes is observed.

A nonionic surfactant (Span 80, sorbiton monooleate) is dissolved in the mineral oil at a concentration  $C = 2.3\times 10^{-2}\text{ M}$ , well above its critical micelle concentration (CMC) ( $C_{CMC}=2.3\times 10^{-4}\text{ M}$ ). At and above the CMC the equilibrium tension  $\gamma$  is  $3\text{ mN}/\text{m}$  and the equilibrium surface concentration  $\Gamma_{CMC}=3.6\times 10^{-6}\text{mole}/\text{m}^2$ ; dynamic tension measurements

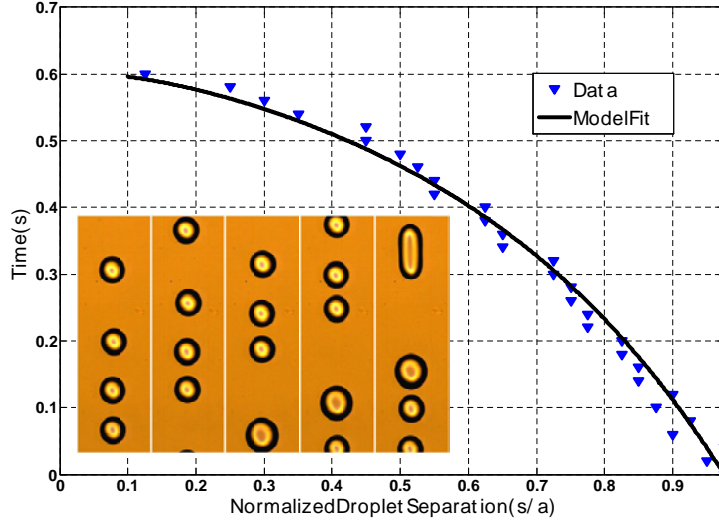


Figure 4.2: Dielectrophoretic merging of  $40\ \mu\text{m}$  radius droplets at the oil/PDMS surface: Frame captures of the pairwise merging at time intervals of .12 sec, flow direction from bottom to top and time ( $t$ ) as function of the measured edge-to-edge scaled separation  $s/a$  from the images. The continuous line is a fit for a value for the droplet-wall drag coefficient,  $\alpha$ .

indicate the desorption rate constant,  $k_d$ , is of order  $10^{-3}\ \text{sec}^{-1}$ .<sup>106</sup> Since the time scale for convection of surfactant along the droplet  $a/\bar{V}$ , order  $10^{-1}\ \text{sec}$ , is much shorter than the desorption time,  $1/k_d$ , surfactant collects at the trailing edge of the droplet causing the tension to be larger at the front than the back. This Marangoni gradient opposes the surface flow and immobilizes the interface since the ratio of the characteristic scale for the retarding tension gradient  $RT\Gamma_{CMC}/a$  to the oil viscous stress on the droplet surface,  $\mu_{oil}\bar{V}/a$ , the Marangoni number ( $Ma = \frac{RT\Gamma_{CMC}}{\mu_{oil}\bar{V}}$ ) is order  $10^2$ . Hence the pairwise hydrodynamic interaction is one of interfacially rigid droplets.

To compare the data sets of  $s(t)$  to a hydrodynamic model of the merging process, the applied field and droplet-wall separation distance  $d$  have to be determined. Since the PDMS and oil are dielectric phases, they act as capacitors in series, and therefore  $\mathcal{E} = \mathcal{V}\{2L_{PDMS}(\epsilon_{oil}/\epsilon_{PDMS}) + L_C\}^{-1}$  with  $\epsilon_{PDMS}$  and  $\epsilon_{oil}$  the dielectric constants for the PDMS and oil (2.65 and 2.18, respectively), and  $L_c$  and  $L_{PDMS}$  are, respectively, the length of the channel and the distance between the electrode and the channel (6 mm and 4.5 mm, respectively). An AC electric potential  $\mathcal{V}$  (500 Hz, 5 kV sine) is applied across the electrodes, resulting in an average field strength  $\mathcal{E}=365\ \text{V/mm}$ . While an alternating potential is used to prevent any residual charge accumulation in the PDMS and oil, the oscillation does not affect

the merging process since  $F_{DEP}$  is proportional to the square of the field, and the oscillation period is much faster than the time scale for the merging. To obtain  $d$ , we assume that at the flow-focusing orifice the droplets detach symmetrically from the top and bottom walls of the channel and are therefore initially centered at the midplane, hence the initial separation  $d_i$  is  $h/2 - a$ . Clearly, each drop is not precisely released at the center of the channel, but statistically above and below the midplane. However, our data analysis will average over several data sets at a nominal value of  $d$  which should account for this statistical variation. The distance  $d$ , accounting for only the resistance of the lower wall, is, for  $d/a \ll 1$ , given by<sup>107</sup>  $\ln \left\{ \frac{d}{d_i} \right\} = -\frac{2ga(\rho_{water}-\rho_{oil})}{9\mu_{oil}}\tau$  where  $g$  is the acceleration of gravity. (Values for  $d/a$  are less than 0.25, for which this expression is accurate. The equation for  $d$  can be corrected to include wall-slip and the effect of the resistance due to the opposite channel wall, but these corrections, if included, can be shown to be negligible in the determination of  $d$ .<sup>108</sup>)

### 4.3 Finite Element Simulations of the Droplet Hydrodynamics

The droplet hydrodynamics is in the Stokes regime of negligible inertia. The Reynolds number, as given by  $Re = \rho_{oil}\bar{V}h/\mu_{oil} = O(10^{-4})$ , and the droplets remain spherical until the onset of coalescence (cf. Fig. 4.2) as the viscous forces are smaller than the tension force (capillary number,  $Ca = \mu_{oil}\bar{V}/\gamma = O(10^{-2})$ ) and the Maxwell electrical stresses are smaller than the tension force (electric Bond number,  $B_e = \varepsilon_o\varepsilon_{oil}\mathcal{E}^2a/\gamma = O(10^{-2})$ ), where  $\varepsilon_o$  is the permittivity of free space. The total fluid drag exerted on each of the droplets as they merge can be calculated from the sum of the fluid drags (formulated as a drag coefficient  $f$  multiplied by  $6\pi\mu_{oil}a$  and a velocity) in three flow configurations (Fig. 4.3): the Poiseuille flow over fixed droplets ( $f_p$ ), and the motions, stationary in the farfield, of  $A$  with  $B$  fixed or  $B$  with  $A$  fixed, with the later two configurations each divided into a mutual approach ( $f_m$ ) and an in-tandem motion ( $f_u$ ). The total fluid drag balances  $F_{DEP}$ ,  $V_A - V_B = \frac{2F_{DEP}}{6\pi\mu_oaf_m}$ . The slip is obtained by comparison of a theoretical calculation of  $f_m$  (a function of  $h/a$ ,  $s/a$ ,  $d/a$  and  $\lambda/a$ ) to an experimental value calculated through the measurement of  $V_A - V_B$  (or equivalently  $s(t)$ ) and  $F_{DEP}$ .

To obtain  $F_{DEP}$ , the electric field in the mineral oil around the merging (uncharged) water droplets in the microchannel is approximated by the bispherical harmonic solution<sup>109</sup> for

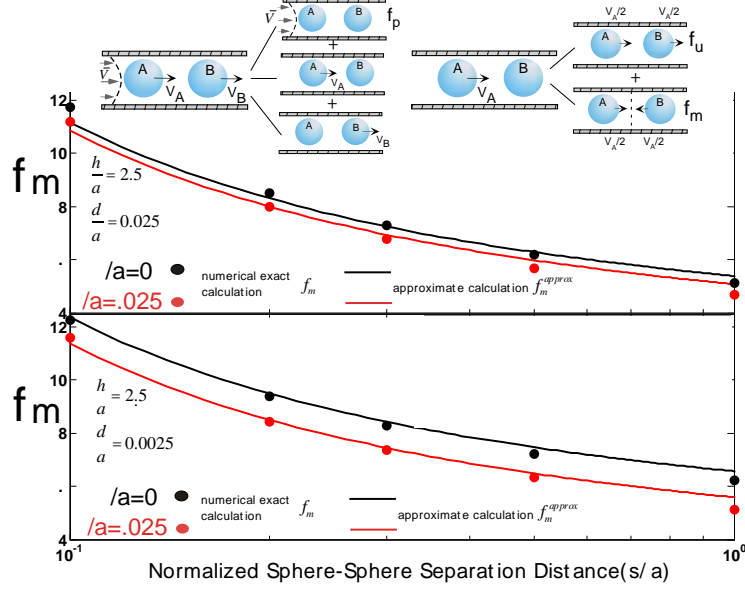


Figure 4.3: The drag coefficient  $f_m$  as a function of  $s/a$  for no-slip ( $\lambda=0$ ) and  $\lambda=1 \mu\text{m}$  for  $d=1 \mu\text{m}$  (top) and  $d=100 \text{ nm}$  (bottom) for  $h=100 \mu\text{m}$  and  $a = 40 \mu\text{m}$ .

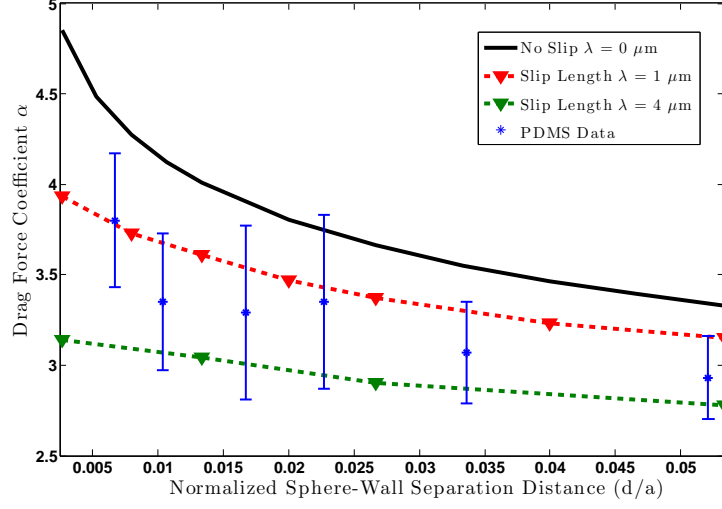
the electrostatic field in an unbounded insulating dielectric surrounding a pair of perfectly conducting spheres (zero net charge) due to a farfield electric field applied in the direction of the line of centers between the spheres, from which  $F_{DEP} = \epsilon_o \epsilon_{oil} a^2 \mathcal{E}^2 \Im(s/a)$ .  $\Im(s/a)$  is an infinite series function of  $s/a$  evaluated here with polynomial interpolation (see Appendix B).

The coefficient  $f_m$  is calculated numerically from a COMSOL (4.2a) finite element simulation using the experimental parameters. The simulation is first verified by computing the drag coefficient for a single sphere in a plane-parallel channel moving parallel to the wall, denoted as  $\alpha(d/a, \lambda/a, h/a)$ , and comparing for  $\lambda/a=0$ , to an interpolating formulae for  $\alpha$  for no slip obtained from a multipole solution by Feuillebois et al<sup>110</sup> (see Appendix B). Fig. 4.3 shows  $f_m$  (symbols) as a function of  $s/a$  for no slip and  $\lambda=1 \mu\text{m}$ , for  $a=40 \mu\text{m}$  and for a separation distance  $d = 1 \mu\text{m}$  (top) and  $100 \text{ nm}$  (bottom). As expected, the closer the droplet pair to the wall, the greater is the influence of the slip, and it is clear that when  $d$  of the order of a few hundred nanometers a order ten percent reduction in  $f_m$  is achieved from the no-slip case for  $\lambda=1 \mu\text{m}$ , and this change is the basis of our measurement of a order one micron slip length. A slip coefficient can be obtained from the experimental profiles  $s(t)$  by comparison to the integration of  $\frac{ds}{dt} = V_A - V_B = \frac{2F_{DEP}}{6\pi\mu_o a f_m}$  using the numerical calculations of  $f_m$  as a function of  $s$ . We avoid this extended calculation by an approximation for  $f_m$  as the sum of the drag on a single (rigid) droplet moving at a distance  $d$  in

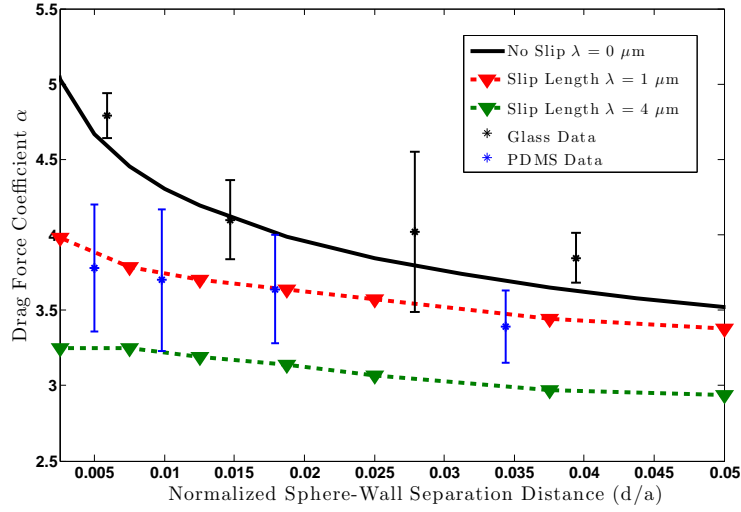
a channel of height  $h$  with slip  $\lambda$ ,  $\alpha(d/a, \lambda/a, h/a)$  (obtained by COMSOL calculation and independent of  $s$ ), the drag on a (rigid) droplet pair mutually approaching at a distance  $s$  from each other in an infinite medium,  $\mathcal{R}$  (Jeffreys solution for which there is a correlation,  $\mathcal{R}(\frac{s}{a}) = \{1 + \frac{a}{2s}\} \left\{1 + .38e^{-\{\ell n \frac{s}{a} + .68\}^2 / 6.3}\right\}$ , see supplementary material) and a correction  $\mathcal{D}(s/a)$ :  $f_m^{approx} = \alpha \left\{ \frac{d}{a}, \frac{\lambda}{a}, \frac{h}{a} \right\} + \mathcal{R} \left\{ \frac{s}{a} \right\} + \mathcal{D} \left\{ \frac{s}{a} \right\}$ . The correction factor  $\mathcal{D}(s/a)$  accounts for the double counting evident in  $f_m^{approx}$  when  $s/a$  tends to infinity and should tend to -1; we use  $\mathcal{D}(s/a) = -\frac{s/a}{1+s/a}$  which allows congruence of the approximate formulation over the entire range of  $s/a$ , cf. Fig. 4.3. A theoretical prediction for  $s(t)$  can be constructed by integrating the force balance, using  $f_m^{approx}$ :  $t = \int_{s_i/a}^{s/a} \frac{\alpha \left\{ \frac{d}{a}, \frac{\lambda}{a}, \frac{h}{a} \right\} + \mathcal{R} \left\{ \frac{s}{a} \right\} + \mathcal{D} \left\{ \frac{s}{a} \right\}}{\varepsilon_o \varepsilon_{oil} \mathcal{E}^2 \mathfrak{S} \left\{ \frac{s}{a} \right\} / 3\pi \mu_{oil}} d \left\{ \frac{s}{a} \right\}$  where  $s_i$  is the initial separation of the droplet pair. This prediction is easily fit to a data set by adjusting  $\alpha$  (which is independent of  $s$ ), and the fit is shown for the illustrative data in Fig. 4.2. (In practice, to include the forces on the droplets due to immediate neighbors of the train at an assumed distance  $s_t$  from the pair, we have addended their dielectrophoretic dipole contribution ( $\frac{24\pi}{(s_t/a+2)^4}$ ) to  $\mathfrak{S}$  and the leading order droplet-droplet interaction  $1 + a/(2s_t)$  to  $\mathcal{R}$ .) All data sets corresponding to different  $d$  and  $a$  are fit in this way. To correlate the fitted values of  $\alpha$  to  $\lambda$ , we first bin all the data sets into groups in which in each group the radii differ by at most 3 percent. Each binned group in diameter is then further binned into wall separation distances  $d$  which differ by no more than 3 percent. The results are plotted as the symbols with error bars (from the standard deviation from the average) in Fig. 4.4 for a droplet radii bin  $a=37.5 \pm 1.25 \mu\text{m}$  and a bin  $a=40 \pm 1.25 \mu\text{m}$  as a function of the (binned) values of  $d/a$ . As each droplet radius bin corresponds to a fixed value of  $h/a$ , the theoretical value of  $\alpha$  in these bins is only a function of  $d/a$  and  $\lambda/a$ . Plotted in Fig. 5.4 as symbols (for the two radii bins) are the theoretical values as a function of  $d/a$  for values of  $\lambda$  equal to zero (the Feuillebois correlation<sup>110</sup>), 1 and 4  $\mu\text{m}$  (from COMSOL calculation). For the PDMS bottom channel wall, the comparison of the theoretical and experimental values of  $\alpha$  show clearly a micron-sized slip, while for a bottom microchannel wall made of glass, no-slip is obtained as expected.

## 4.4 Conclusions

Our demonstration of order one micron slip at the interface of an oil and a polymeric surface (PDMS) which releases to the surface air retained in the material to form a lubricating layer, may serve as method for enabling giant slip without having to modify the surface with



(a)



(b)

Figure 4.4: Hydrodynamic drag coefficient  $\alpha$  as a function of separation  $d/a$  for droplets of radius  $37.5 \mu\text{m}$  (a) and  $40 \mu\text{m}$  (b) for fixed height  $h=100 \mu\text{m}$ . Symbols with error bars are the experimentally fitted coefficients, the remaining symbols are from numerical simulation (the accompanying dotted lines are a guide), and the no-slip line is from the Feuillebois et al<sup>110</sup> correlation.

an air-sequestering texture. These results are particularly relevant to microfluidics where PDMS is the standard material, and the use of oil streams with reagent water droplets have become a dominant lab on a chip platform.

## 4.5 Appendix A: Materials and Cell Fabrication

Aqueous Phase: DI water, from Millipore ultrafiltration unit, conductivity,  $18 \text{ M}\Omega \text{ cm}^{-1}$ , and from handbook values  $\rho_w = 10^3 \text{ kg m}^{-3}$ , and  $\mu_w = 10^{-3} \text{ kg m}^{-1}\text{s}^{-1}$  at  $20^\circ\text{C}$ . Mineral oil: Sigma-Aldrich,  $\varepsilon_{oil} = 2.18$  (parallel plate capacitor measurement),  $\rho_{oil} = 8.75 \times 10^2 \text{ kg m}^{-3}$  (manufacturer's data sheet) at  $20^\circ\text{C}$ . The oil viscosity  $\mu_{oil}$  is temperature sensitive in the range in which the experiments were undertaken ( $20\text{--}23^\circ\text{C}$ ), and was measured (with the surfactant, Span 80,  $C = 2.3 \times 10^{-2} \text{ M}$ ) by a temperature-controlled rheometer (see data below, Figure 1) and fit to a correlation  $\mu(T) = 2.20 \times 10^{-5}T^3 - 1.63 \times 10^{-3}T^2 + 3.58 \times 10^{-2}T - 0.139$ . A thermocouple in the PDMS measured the temperature for each experiment, and in the fitting for the drag coefficient  $\alpha$  the viscosity at the temperature measured for the experiment was used by calculation from the correlation.

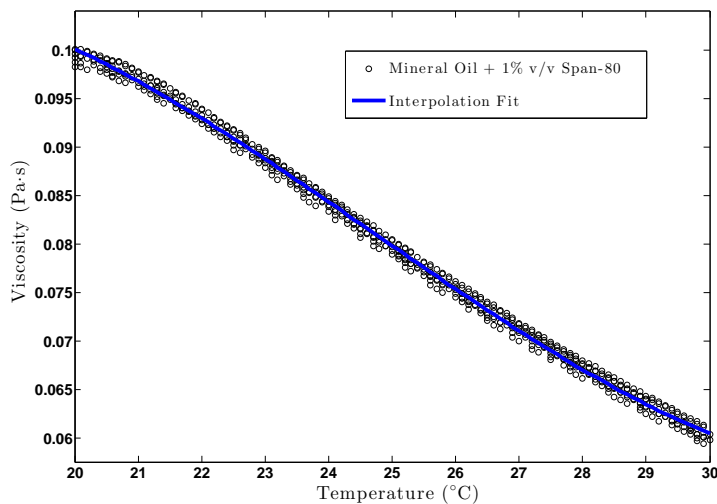


Figure 4.5: Viscosity of mineral oil as a function of temperature.

The microfluidic cell is fabricated via the methods of soft lithography<sup>111</sup> from two slabs of polymerized and cured PDMS, one slab containing the inscribed channels and a second, flat slab bonded to the first to enclose the channels. The PDMS prepolymer and curing



agent is obtained as a kit, Sylgard 184 (Dow Corning). The top half of the cell containing the inscribed fluidic circuitry is molded from a master fabricated by photolithography using a transparency mask and a negative tone SU-8 photoresist and developer (Microchem), and the lower half is a cast layer of PDMS which is bonded to the top half by plasma treating the surfaces and then conformally contacting the halves. Dielectric constant of cured elastomer is 2.65 (manufacturer's material data sheet). Fluids are delivered to the cell from syringe pumps (Harvard PHD) via polyethylene tubing (1.5 mm ID) through punch-hole entry ports.

## 4.6 Appendix B: Interpolating Functions and Validation Simulations of the Finite Element Calculations

The calculation of Davis<sup>109</sup> for the dielectric force on a pair of zero charge perfectly conducting spheres in an unbounded insulating dielectric subject to a uniform electric field  $\mathcal{E}$  at infinity applied along the line of centers of the spheres is given as an infinite series solution of the edge-to-edge separation distance  $s$  divided by  $a$ , from which the dielectrophoretic force between the spheres is obtained as  $F_{DEP} = \varepsilon_o \varepsilon_{oil} \mathcal{E}^2 a^2 \mathfrak{S}(s/a)$  where  $\mathfrak{S}(s/a)$  is an infinite series.

We approximate the series by the polynomial  $\mathfrak{S}(s/a) = -2.02 \times 10^{-7}(s/a)^3 + 7.33 \times 10^{-7}(s/a)^2 - 9.99 \times 10^{-7}(s/a) + 5.99 \times 10^{-7}$  and a comparison of this interpolation formulae and the Davis expression is given in 4.6.

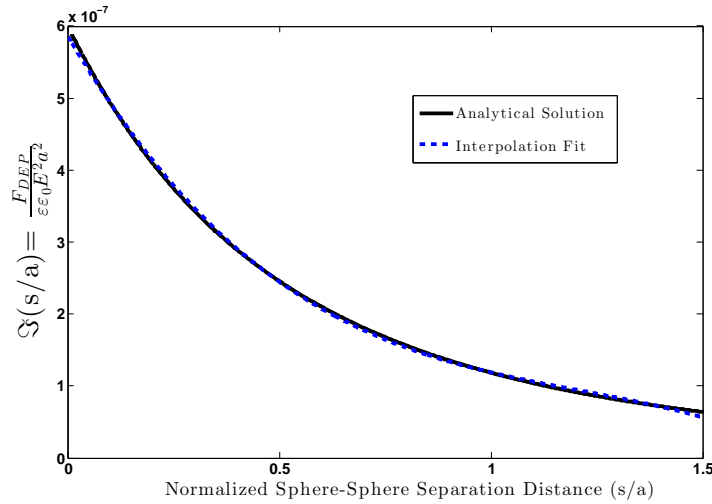


Figure 4.6: Normalized electrostatic force as a function of normalized separation distance as given by the exact bispherical calculation and the interpolating equation.

The solution for the hydrodynamic drag exerted on a pair of two mutually approaching (interfacially rigid or solid) spheres in an infinite medium is the Stimson and Jeffrey solution in bispherical coordinates and is expressed as an infinite series and the drag coefficient  $\mathcal{R}(s/a)$  is expressed as an infinite series (see eq. 4.1); for numerical calculation we use the interpolation as given by Ivanov et al<sup>112</sup> and written in the manuscript

$$\mathcal{R}(s/a) = \sinh \epsilon \sum_{n=1}^{\infty} \frac{n(n+1)}{\Delta_n} \left\{ \frac{\lambda_n \exp(2\epsilon)}{2\lambda_{n-1}} + \frac{\lambda_n \exp(-2\epsilon)}{2\lambda_{n+1}} + \frac{\exp(-2\epsilon\lambda_n)}{\lambda_{n-1}\lambda_{n+1}} - 1 \right\} \quad (4.1)$$

$$\cosh \epsilon = 1 + \frac{s}{2a}, \lambda_n = n + \frac{1}{2}, \Delta_n = \sinh(2\lambda_n\epsilon) - \lambda_n \sin(2\epsilon)$$

Detailed multipole solutions for the drag coefficient for a single solid sphere translating parallel and between two parallel walls was given by Feuillebois et al, as cited in the chapter. They construct an interpolating formulae (eq. 29) for this drag coefficient, and in Fig. 3 we compare the results of this correlation with our COMSOL results as a means of validating our numerical simulations.

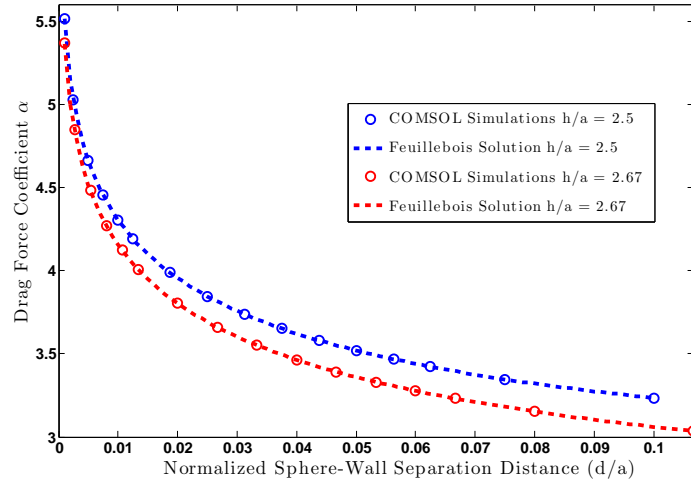


Figure 4.7: Hydrodynamic drag force on a single sphere translating between two parallel walls for no slip,  $\lambda = 0 \mu\text{m}$  as a function of the sphere/wall separation distance  $d$  (edge-to-edge), comparing the Feuillebois correlation and our COMSOL calculation for two values of the channel height  $h$  relative to the sphere radius  $a$ .

## Chapter 5

# Hydrodynamic Capture of Microbeads in Microtexture Obstacle Courses for Biomolecular Screening in Pathogen Sensing and Point of Care Diagnostics

### 5.1 Introduction

Analytical methods which allow a target protein to be screened against a probe library of potential binding partners (e.g. other proteins or small biomolecular ligands) to determine binding affinities are central to fundamental studies in cell and molecular biology, where they can be used to map the web of interactions by which proteins orchestrate biological activity. Screening tools are also important in applied research, where they are used in drug, antibody and enzyme discovery<sup>113–115</sup>, in the identification of disease markers and in the development of biosensors for environmental surveillance and food monitoring<sup>116–119</sup>. The standard method for screening protein binding interactions is the microtitre well plate, in which the library of probe molecules is spotted into an array of wells, and each well is then incubated with a target and interrogated individually (typically with an enzyme linked sandwich immunoassay) to determine target-probe conjugation. Many applications, particularly those using combinatorial synthesis for the development of new biomolecules, require a large number of probe molecules to be displayed, and for these applications the screening platform should be miniaturized to enable higher library probe densities than can be

accommodated with microtitre plates. Flat microarrays (see for example the reviews<sup>120–129</sup>) are one innovation, in which probes are robotically spotted into small areas or patches (a few hundreds of microns in diameter) on a substrate to form a library. Probe biomolecules either adsorb directly to the substrate surface, or the surface is functionalized to covalently bind the printed probe molecules. The library is then incubated with a target, and binding is detected, in a single (parallel) step, usually by fluorescently labelling the target and examining the array for spots which fluoresce upon excitation. In the flat microarray (as with the microtitre plate assay) target first diffuses through a quiescent analyte solution to the surface and subsequently kinetically binds to the surface probe. Binding is detected when enough target binds to the probes to register a fluorescent signal. When transport through the analyte phase is only by diffusion, this assay time can be relatively long even if the kinetic step is fast<sup>130,131</sup>. Streaming analyte across the flat microarray can enhance the transport by bringing analyte solution directly to the probe surface in a convective boundary layer. The detection time would then be determined by only the kinetic rate (a property of the probe and target), and would not be limited by a diffusion barrier. With this as a goal, biosensor designs have incorporated a printed microarray of probes (or a single patch of one probe) as the bottom surface of a microfluidic channel, and have convectively screened the array with target (for reviews see<sup>132–140</sup>). In an alternative format, separate channels in a microfluidic cell, each displaying one probe at the channel bottom, have been used to construct a library<sup>141–144</sup>. The use of microfluidics to convectively screen patch arrays of probe libraries as a lab on a chip not only reduces the assay time for screening the library by enhancing transport of the target to the probe (and thereby increases the throughput), it has the added advantage of reducing the volumes of targets and reagents that are needed for the assay.

The microfluidic screening platform in which the probe library is an array of patches situated on the floor of the flow channel is one miniaturized design. However, the assembly of this platform is complicated because the microarray has to first be constructed ex-situ of the microfluidic cell, and then incorporated into the cell, a procedure which becomes very difficult when the spotted probes need to be continually immersed in water, as for example cell membrane proteins which are spotted sequestered in lipid bilayers. In-situ methods for assembling the probe library directly inside the flow channel are under current study, and are based on using microbeads (10–100  $\mu\text{m}$  in diameter) to host the probe biomolecules, and facilitate their arrangement into an array library within the microfluidic cell<sup>145–148</sup>. Probe biomolecules are first covalently linked to the microbead surface in sets, with each set prepared separately and displaying a single probe on its surface. (Similar to flow cytometric assays platforms<sup>128,149–156</sup>.) A microbead suspension is then streamed through the microflu-

idic flow channel, and patterning techniques are used to position and fix the microbeads in separable positions along the channel to form a probe array. A library of multiple probes is constructed by sequentially streaming the microbeads in sets with each set displays only one probe. After a set is introduced, the locations of the members of the set in the channel are noted before the next set is introduced so a registry of the probe on each arrayed microbead can be compiled. Fluorescently labelled target can then be streamed through the cell and over the microbeads to undertake a screening assay, with binding events recognized by identification of fluorescing microbeads, and the binding probe identified by referencing the library registry.

The patterning used to fix the microbeads in array positions in the microfluidic cell is the key to the assembly process. The most straightforward method for fixing beads in position on a surface would be to pattern the surface in an array of adhesive domains, i.e. islands with functional groups which stick to the microbeads when the beads are deposited on the surface. Surfaces patterned with functionalities which allow beads to stick by electrostatic forces or covalent bonding have been used to assemble a microbead array on a substrate outside of a flow cell<sup>157–161</sup>, and these arrays have been utilized to screen biomolecules by incubating static analyte solutions above the array in analogy with the a flat microarray. Similarly, a microbead array can be assembled within a microfluidic flow channel by streaming a suspension of beads through though the channel and allowing them to stick to adhesive domains on the floor of the channel. However, these immobilized microbeads are typically displaced by the target flow because the binding of the microbead to the surface is not over enough bead area to insure a strong retaining force. For this reason, studies have focused on using retaining structures to position the microbeads in fixed locations. The two designs that are the most common are wells patterned into the bottom surface of the microfluidic cell<sup>162,163</sup> and traps arranged as a microfluidic obstacle course (DiCarlo et al<sup>164,165</sup>, Cooper et al<sup>166–171</sup>, Huebner et al.<sup>172</sup> and Nehorai et al<sup>173,174</sup>. Well designs size the cavity to be only slightly larger than the microbead to be retained, so that only one microbead is captured at a location. Well deposition has also been enhanced by using electric and magnetic fields to assist in the capture<sup>175–177</sup>, or by using holes placed in the well and connected to a drain to provide fluid suction (see McDevitt et al<sup>178–187</sup> and Ketterson<sup>188</sup>). Trap obstacle courses in microfluidic cells have been used predominantly to hydrodynamically array cells, or droplets containing cells, but a few reports have used the trapping geometry to array microbeads, including ones which has studied optimal geometries for the trap shape and course arrangement to insure high capture efficiency<sup>173,174</sup>, and our effort which demonstrated the arraying of microbeads with a lipid bilayer (lipobeads) for screening membrane receptors<sup>189</sup>. Traps designed to capture a single microbead are usually half-open, “V” shaped retaining

structures which span the height of the channel and are oriented with the open part of the cavity facing the flow. These designs typically have an opening at the back end of the trap, to facilitate flow through the trap enabling easy capture and allowing target to stream over a trapped microbead (see Fig. 5.1 used in our study<sup>189</sup> and similarly in<sup>173,174</sup>).

The major question which emerges when retaining structures are used to assemble probe-functionalized microbeads in a microfluidic cell to construct a probe library is the effect of the retaining structure on the mass transfer of the target to the probes on the microbead surface. As a reference, consider first the target transport in the idealized case in which the microbeads are (fictitiously) attached to the bottom of the flow channel without a retaining structure. The target transport occurs in two steps. Target diffuses from the stream passing over the microbeads to the bead surface by crossing the flow streamlines, and then kinetically conjugates to the probes on the bead surface. As a result, a diffusion zone is created around the microbead in which the concentration falls below the inlet concentration. Within this zone, a target concentration gradient is formed normal to the surface with the concentration decreasing from the inlet concentration at the top of the zone to a reduced concentration in the sublayer of liquid immediately adjacent to the surface (the sublayer concentration). As binding proceeds and the surface becomes saturated with target, the kinetic conjugation rate decreases, causing the sublayer concentration to increase as the gradients in concentration in the diffusion zone relax and eventually disappear at equilibrium in which case the concentration around the bead becomes equal to the inlet concentration. Hence the overall binding rate of the target to the probe is determined by an in-series transport process of diffusion and surface kinetics. When the convective flow along the surface is fast relative to the diffusion normal to the surface, this transport picture is retained, but the diffusion zone becomes a thin boundary layer and the diffusive flux to the surface becomes large, and the surface quickly saturates. For any flow regime, it is the kinetic conjugation step of the target to the surface probe that actually populates the surface with the target. This step is described by a surface kinetic equation that relates the rate of conjugation to the instantaneous surface concentration of the target, and the target's sublayer concentration adjoining the surface, as for example, the Langmuir equation. If this surface kinetic rate is much slower than the diffusion rate (due to the concentration gradient normal to the surface in the diffusion or boundary layer zone), the concentration gradient decreases and the concentration of target in the zone approaches the inlet concentration. In the limit of a very slow kinetic conjugation relative to diffusion, the overall binding rate is simple to describe since it is only determined by integrating the surface kinetic equation with the sublayer concentration equal to the inlet concentration (the ideal kinetic limit). However, if the kinetic rate is of order of the rate of bulk diffusion, then the diffusion gradients reduce the overall binding rate from the simple

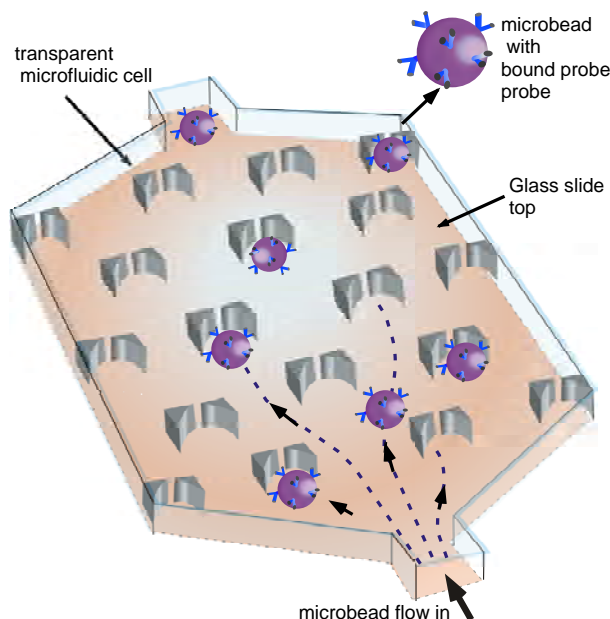


Figure 5.1: Microbeads hosting surface probes are arrayed in a microfluidic cell using a trapping course.

kinetic limit and the transport process is mixed with the sublayer concentration obtained from the solution of the convective diffusion mass transfer equations.

When retaining structures such as traps and wells are used to array microbeads in fixed positions, the confinement reduces the convective flow around the microbead, and decreases the mass transfer rate of target to the surface probes by increasing the size of the diffusion zone or the boundary layer thickness. A reduction in the target transport rate affects the performance of the screening assay, as it increases the time necessary to achieve the particular level of target concentration necessary to detect a signal. The focus of this study is to examine this effect for the case in which microbeads are arrayed by an obstacle course of traps (see Fig. 5.1). While the analysis of the binding of targets to surface probes as a screening platform has been studied in detail for the case of probe “patches” situated on a microchannel wall<sup>133,190–199</sup>, the binding of target to microbeads captured in traps has received very limited attention. Bau et al<sup>200</sup> studied the geometry of microbeads sandwiched between the top surface of a flow channel and a shallow well at the bottom of the channel (the microbeads were preassembled in the shallow wells before closing the cell), and obtained solutions for the target concentration on the microbead surface as a function of the stream velocity and target-probe kinetic rate constants. These simulations represent approximately the idealized case of unobstructed microbeads. Our aim is to construct numerical solutions for the hydrodynamic flow and target mass balance equations to determine the surface concentration on the bead surface as a function of time when the microbeads are entrapped. The

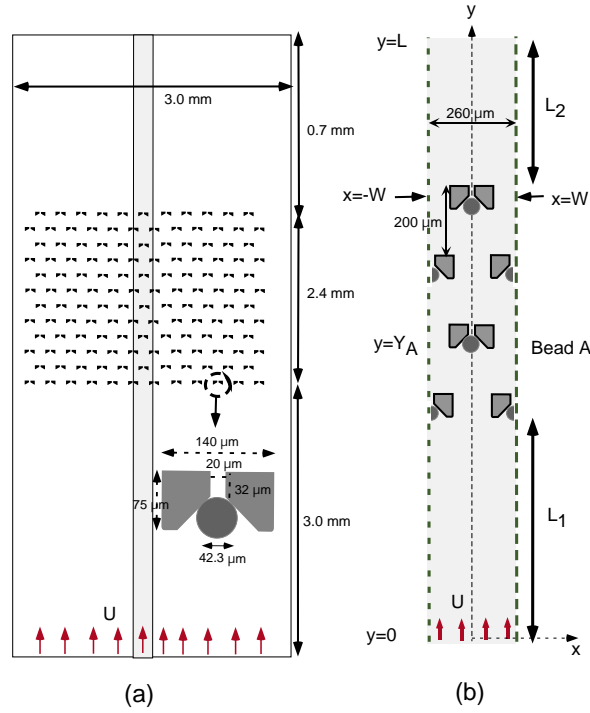


Figure 5.2: (a) Schematic of the trapping array used in the experiments and modeled in the simulation, and an inset detail of an individual trap with a microbead. The analyte solution is streamed from bottom to top. (b) Schematic of the unit cell computational domain with dimensions.

solutions are compared to the binding rates of target to probes on unconfined microbeads in a channel (as the Bau simulations) to determine the effect of the trap. The simulations will also be used to identify regimes of slow surface kinetics for which the overall binding rate approaches the ideal kinetic limit. This criteria is of interest in experimental studies of target-probe binding kinetics since the ideal kinetic binding rate is a simple expression easily compared to experimental measurements of the binding rate to determine the appropriate kinetic model or to evaluate surface kinetic rate constants. We will also undertake screening experiments on the microbead array to illustrate how the simulations can be used to select experimental conditions on the imposed flow rate so that the experimentally measured overall binding rate of the target to the surface probes is controlled by the surface conjugation step so the overall binding rate can be easily simulated. For this demonstration, we will use the protein NeutrAvidin as the target, and biotin (its binding partner) as the probe. Biotin will be bound to the surface of the microbeads, and the NeutrAvidin will be fluorescently labelled so that its accumulation on the microbead surface can be quantitatively measured to obtain the overall binding rate.



## 5.2 Hydrodynamic and Mass Transfer Numerical Simulations

### 5.2.1 Formulation

The simulation of the target analyte flow, and the convective diffusion and binding of the target to the probes on the microbeads arrayed in traps in the flow cell is constructed as a three dimensional simulation which models directly the trapping geometry used in our earlier publication on lipobead arraying<sup>189</sup> and the Neutravidin-biotin binding assay experiments which are described later on. A schematic of the experimental layout of the trap arrangement in the obstacle course, and the detail of an individual trap, is shown in Fig. 5.2a. The traps, in a wide channel, are arranged in parallel rows (perpendicular to the flow) which are separated by  $200\text{ }\mu\text{m}$ , and columns (along the flow) which are separated by  $260\text{ }\mu\text{m}$  and staggered symmetrically with an offset of  $130\text{ }\mu\text{m}$  (Fig. 5.2b). The channel is of rectangular cross section, with an overall channel width of  $3\text{ mm}$ , a length of  $6.1\text{ mm}$  and a height,  $h$  is  $60\text{ }\mu\text{m}$ . A total of 144 traps are arranged in a cluster at approximately the center of the flow channel. (The open area downstream of the cluster accomodates an entry port for the introduction of the microbeads, and both ends are connected to channels of smaller width( $300\text{ }\mu\text{m}$  from which the analyte flow enters and exits.) The “V” shaped configuration of the trap contains an aperture at the back end which is  $20\text{ }\mu\text{m}$  in width, permitting the microbeads which have a diameter  $2a$  equal to  $42.3\text{ }\mu\text{m}$  to be captured. The trap height is equal to the channel height. The microbeads, which are made of glass in the experiments, settle to the bottom of the flow cell during the entrapment process, and therefore an approximately  $20\text{ }\mu\text{m}$  gap exists between the microbead and the top wall of the microchannel, permitting flow over a microbead when it is localized in the trap. To simplify the calculations, we ignore the edge effects of the side walls of the channel, and undertake calculations on a unit cell (Fig. 5.1b) with symmetry boundary conditions for the flow and mass transfer along the side walls of the unit cell. A cartesian coordinate system is located with an origin at at the center of the entrance and the bottom wall of the channel, with  $y$  in the flow direction,  $x$  perpendicular to the side walls and  $z$  perpendicular to the bottom wall. The unit cell consists of 4 of the twelve rows of the trapping course bounded by inlet and exit cross-section planes at  $y = 0$  and  $L$ , respectively. (Calculations demonstrate that the addition of a further row did not change either the flow or the mass transfer.) The microbeads in the unit cell are symmetrically placed at the centerline of the traps, and are fixed in a position touching at one point the bottom of the flow cell. While in experiments the analyte flow pushes the microbead directly against the trap walls, in the simulations, the

microbeads are separated by a distance of  $1 \mu$  to avoid complexities in the mesh construction for the numerical solution. Reducing this separation distance did not change the results. A uniform velocity  $U$  (in the  $y$  direction) and a uniform target concentration  $c_o$  is imposed at the upstream inlet ( $y = 0$ ); at the exit ( $y = L$ ) a zero pressure condition is imposed, and the derivative of the concentration in the  $y$  direction is set equal to zero. The symmetry boundary conditions along the side walls ( $x = \pm W$ ) of the unit cell are that the velocity in the  $x$  direction is equal to zero, and the derivative, in the  $y$  direction of the velocity in the  $y$  and  $z$  direction and the concentration is equal to zero. At the initial time, the target concentration in the unit cell is assumed to be uniform and equal to  $c_o$ .

The target solution is assumed to be an incompressible Newtonian fluid with density  $\rho$  and viscosity  $\mu$  of water ( $\rho=10^3 \text{ kg m}^{-3}$  and  $\mu = 10^{-3} \text{ kg m}^{-1}\text{sec}^{-1}$ ) independent of the analyte concentration which is assumed to be dilute. The steady hydrodynamic flow is described by the solution of the continuity and Navier-Stokes equations, written in nondimensional form in terms of the velocity  $\tilde{\mathbf{v}}$  scaled by the velocity  $U$ .

$$\nabla \cdot \tilde{\mathbf{v}} = 0 \quad (5.1)$$

$$\Re \mathbf{e} [\tilde{\mathbf{v}} \cdot \nabla \tilde{\mathbf{v}}] = -\nabla \tilde{p} + \nabla^2 \tilde{\mathbf{v}} \quad (5.2)$$

where the nondimensional variables  $\nabla$  and  $\nabla^2$  are the gradient and Laplacian operators (scaled by  $h$ ),  $\tilde{p}$  is pressure (nondimensionalized by  $\mu U/h$ ), and  $\Re \mathbf{e} = \frac{\rho U a}{\mu}$  is the Reynolds number. The continuity and Navier-Stokes equations are solved in cartesian coordinates with the inlet and outlet conditions detailed above, and boundary conditions of no slip on the interior walls of the trap and the bead surface and symmetry conditions along the unit cell border  $x = \pm W$ . The solution is obtained numerically using finite elements implemented with the COMSOL Multiphysics simulation package (4.2), using both triangular and quadrilateral meshes.

The concentration field of the target is obtained by solving the convective diffusion equation

$$\frac{\partial \tilde{c}}{\partial \tau} + Pe \tilde{\mathbf{v}} \cdot \nabla \tilde{c} = \nabla^2 \tilde{c} \quad (5.3)$$

In the above,  $\tilde{c}$  is the concentration of target (nondimensionalized by the inlet concentration  $c_o$ ),  $\tilde{\mathbf{v}}$  is the steady velocity obtained above, and  $Pe$  is the Peclet number defined as  $Pe = Ua/\mathcal{D}$ , with  $\mathcal{D}$  the diffusion coefficient of the target and time is scaled by the diffusion time  $\tau_{\mathcal{D}} = a^2/\mathcal{D}$  the time required for target to diffuse over the length scale  $a$  of the bead.  $Pe$  is the ratio of the time required for fluid to convect over the microbead ( $a/U$ ) to the diffusive time scale  $\tau_{\mathcal{D}}$ . Eq. 5.3 is solved with the inlet and outlet conditions detailed above, and assuming zero flux of target on the surfaces of the trap and channel walls and symmetry conditions on

the borders ( $x = \pm W$ ) of the unit cell. The boundary condition on the microbead surface models the binding kinetics, and is described in detail in the following.

The kinetic binding of target from the sublayer of liquid immediately adjacent to the microbead surface to probes on the microbead surface is a bi-molecular process. which is described generally by,

$$\frac{\partial}{\partial t} \left\{ \frac{\Gamma}{\Gamma_\infty} \right\} = k_a c_s \phi - k_d \left\{ \frac{\Gamma}{\Gamma_\infty} \right\} \quad (5.4)$$

where  $\Gamma$  is the surface concentration of target,  $\Gamma_\infty$  is the maximum concentration of target which can bind,  $t$  is time,  $c_s$  is the sublayer concentration of target at the surface and  $k_a$  and  $k_d$  are the association and disassociation rate constants, respectively and  $\phi$  is the fraction of sites available when the target concentration is  $\Gamma$ . To calculate  $\phi$ , we specify first the density of probes fixed on the surface as  $\Gamma_p$ , and the projected area per molecule of the target as  $\mathcal{A}_t$ . When the surface density of probes ( $\Gamma_p$ ) is small enough such that bound target does not overlap unbound sites ( $\Gamma_p \mathcal{A}_t < 1$ ), the maximum concentration of bound target is equal to the probe density  $\Gamma_\infty = \Gamma_p$  and the fraction of sites available is  $\phi = 1 - \frac{\Gamma}{\Gamma_p}$ , leading to a simple Langmuir kinetic scheme. Under many circumstances, the target's projected area is much larger than the probe area, and surface densities can be large enough so that  $\Gamma_p \mathcal{A}_t \geq 1$ . In this case, as binding proceeds, the binding of targets to probes becomes sterically hindered, and the fraction of sites available is not given by  $\phi = 1 - \frac{\Gamma}{\Gamma_p}$ . Models for  $\phi$  to account for steric hindrance based on Monte Carlo simulations of random sequential adsorption have been developed (e.g.<sup>201</sup>), and these also calculate  $\mathcal{A}_t \Gamma_\infty$  as a function of  $\Gamma_p \mathcal{A}_t$ . Here, for our simulations, we generalize the Langmuir equation and assume that  $\phi = 1 - \frac{\Gamma}{\Gamma_\infty}$  where the maximum packing can be obtained from the random sequential model calculations. In the experiments, the surface density is low enough such that  $\Gamma_p \mathcal{A}_t \ll 1$  so the Langmuir model is applicable with  $\Gamma_\infty = \Gamma_p$ . The equilibrium surface density ( $\Gamma_{eq}$ ) is  $\frac{\Gamma_{eq}}{\Gamma_\infty} = \frac{k}{1+k}$  where  $k = \frac{k_a c_o}{k_d}$ . Many biomolecular binding processes are nearly irreversible (i.e.  $k \gg 1$ ), and in our screening experiments on the binding of Neutravidin to surface biotin previous experiments show that this is certainly the case. Therefore in our simulations, we will neglect the disassociation step. The boundary conditions on the microbead surface equate the diffusive of target to the kinetic rate of binding, and sets the rate of accumulation of target at the microbead surface to the flux:

$$\{\mathbf{n} \cdot \nabla \tilde{c}\}_{\text{bead}} = Da \left[ \tilde{c}_s \left\{ 1 - \tilde{\Gamma} \right\} \right] \quad (5.5)$$

$$\Omega \frac{\partial \tilde{\Gamma}}{\partial \tau} = \{\mathbf{n} \cdot \nabla \tilde{c}\}_{\text{bead}} \quad (5.6)$$

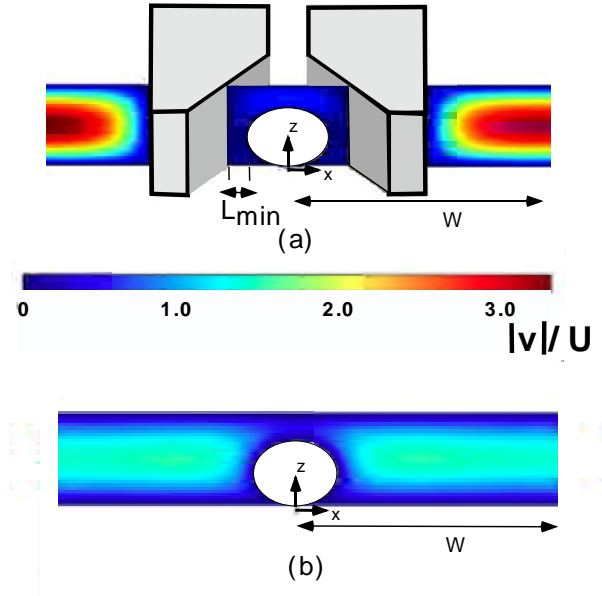


Figure 5.3: Simulation of the flow around the upstream center microbead in the unit cell (microbead “A” in Fig. 5.2) in a trapped (a) and untrapped (b) configuration for a flow Reynolds number  $\mathfrak{Re} = 0.2$ . The magnitude of the velocity (divided by the average velocity  $U$ ) is plotted in the  $x - z$  plane corresponding to the equatorial section of the bead perpendicular to the flow,  $y = Y_A$ .

where  $\mathbf{n}$  is the outward normal to the microbead surface,  $\tilde{c}_s$  is the nondimensional sublayer concentration,  $\Omega = \frac{\Gamma_\infty}{c_o a}$ ,  $Da$  is the Damkohler number,  $Da = \frac{k_a \Gamma_\infty a}{\mathcal{D}}$  and  $\tilde{\Gamma}$  is the surface concentration scaled by the maximum binding density  $\Gamma_\infty$ . The parameter  $\Omega$  is the ratio of the adsorption depth  $\Gamma_\infty/c_o$ , the distance above the surface which contains (per unit area) enough target to saturate the surface to the microbead radius  $a$ . The Damkohler number is the ratio of the characteristic kinetic flux to the surface ( $k_a c_o \Gamma_\infty$ ) to the characteristic diffusive flux on the particle length scale ( $\mathcal{D} c_o/a$ ). The surface concentration ( $\Gamma$ ) is a function of the position on the bead surface, and we denote by  $\bar{\Gamma}$  the average value on the bead surface.  $\bar{\Gamma} = \frac{1}{\mathcal{A}} \int_{\mathcal{A}} \Gamma d\mathcal{A}$  where  $\mathcal{A}$  is the area of the microbead surface.

The mass transfer equations are integrated using the COMSOL simulation package, using forward marching in time. An adaptive time step is used in which for the earliest times for large  $Pe$  the time step is set to one order of magnitude smaller than the time required for formation of the boundary layer around the microbead,  $\delta^2/\mathcal{D}$  and for order one  $Pe$  the diffusion time scale  $a^2/\mathcal{D}$

### 5.2.2 Hydrodynamic Flow Simulations

In a typical microfluidic trapping geometry, channel heights and widths are of order  $10^2 \mu\text{m}$  and  $10^3 \mu\text{m}$ , respectively and for flow rates of order  $10^{-1} - 10^2 \mu\ell/\text{min}$ , the average velocity  $U \sim 10 - 10^2 \mu\text{m/s}$ . Hence  $\text{Re}$ , based on the microbead radius (typically  $10 \mu\text{m}$ ) is usually less than  $10^{-1}$ , and the motion is predominately a Stokes inertialess flow. In these simulations, we choose  $\text{Re} = 0.2$ , which is the experimental value. The hydrodynamic flow pattern around a microbead situated at the bottom of the downstream trap at the center of the unit cell (“A” in Fig. 5.2 with center at position  $y = Y_A$ ) is shown in Fig. 5.3a. The flow pattern is the magnitude of the velocity (divided by the average velocity  $U$ ) in the  $x-z$  plane ( $y = Y_A$ ) perpendicular to the flow and through the bead equator. (The flow is symmetric in  $x$  since  $x = 0$  is the symmetry plane of the unit cell. The projection of the figure is an oblique view, accounting for the elliptical appearance of the spherical bead.) Due to the staggered configuration of the traps, most of the flow circulates around, rather than through the trap, as the hydrodynamic resistance through an occupied trap is much larger than the resistance in the open space between the traps. Within the trap, the figure makes clear that the maximum velocity, as would be expected, is in the large gap ( $\approx 20 \mu\text{m}$ ) between the top of the channel and the bead ( $h < z < 2a, y = Y_A, x = 0$ ). Analyte flows through this space, and then out the back of the trap. The lateral gap thickness between the trap sidewalls and the microbead ( $L_{\min} - a > x - a > 0, y = Y_A, z = a$ ) in the equatorial plane of Fig. 5.3a, is much smaller ( $L_{\min} = 10 \mu\text{m}$ ) and the velocity in this gap is less than between the bead and the top wall of the channel. The flow velocity in the same plane around microbead “A” in the untrapped configuration (the same array of microbeads as in Fig. 5.2 but without traps) is given in Fig. 5.3b, and as expected, the flow around the lateral sides of the microbead is larger due to the absence of the trap. In this case the analyte stream freely flows over most of the microbead, except the lower half of the bottom hemisphere which is obstructed by contact with the bottom wall. As fluid is no longer directed around the blunt edges of the traps, the fluid velocity in the space occupied between the symmetry plane and the position formerly occupied by the outer trap wall is reduced relative to when the trap is present. In fact in this space, spanning a distance of  $\approx 2a$  from the microbead to the symmetry plane, approaches two dimensional Poiseuille flow with the maximum velocity at the midplane of the channel in this space equal to  $3/2$  of the upstream average velocity  $U$  in front of the trap cluster.

As stated earlier, in the regime in which the convective rate of transport of target along the microbead is large relative to the diffusive flux to the surface, the mass transfer is through a thin boundary layer around the particle. The thickness of this boundary layer decreases with the local velocity gradient (or shear rate) at the microbead surface, and the target

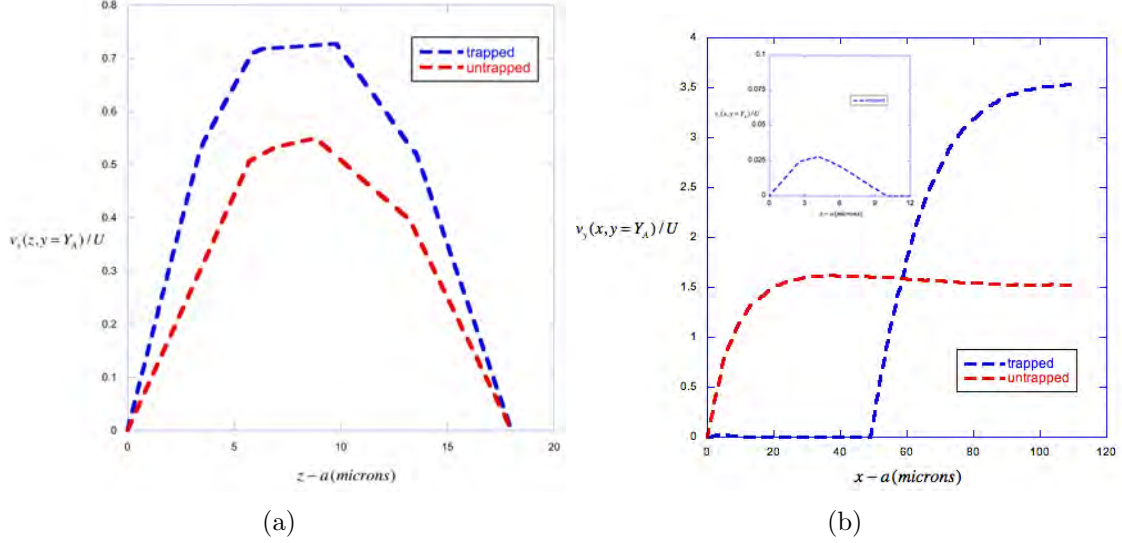


Figure 5.4: Simulation of the flow velocity in the  $y$  (streamwise) direction (divided by  $U$ ) between (a) the top of the channel and the microbead ( $0 < z - 2a < h - 2a$ ,  $y = Y_A$ ,  $x = 0$ ) and (b) the side of the microbead and the channel wall ( $0 < x - a < L_{\min}$ ,  $y = Y_A$ ,  $z = a$ ) and the trap wall and the symmetry plane of the unit cell for the upstream center microbead in the unit cell (microbead “A” in Fig. 5.2) and comparison to the untrapped microbead for  $\mathfrak{Re} = 0.2$ . The inset shows the distribution in the gap between the microbead and the trap wall.

flux becomes correspondingly larger. Hence an examination of the surface shear rate is important in understanding the target transport in the convective regime. Detailed profiles of the velocity in the  $y$  (stream) direction, as a function of the distance across the gaps at the top and sides of the trapped microbead, are shown in Fig. 5.4(a) and compared to the profiles for a microbead without a trap (Fig. 5.4(b)). For the trapped microbead, the flow in the lateral gap is very small (velocities are of order  $10^{-2}U$ ), and the shear rate at the wall is also small. For the top gap, the velocity (of order  $U$ ) and shear rate are much larger, and the target mass transfer to the upper hemisphere of the microbead should be expected to be larger than the lower hemisphere (see the following section). In contrast, in the case of the untrapped microbead, while the shear rate at the top is comparable to that of the trapped microbead, the shear rate along the lateral side is much larger as the trap no longer blocks the flow, and the mass transfer rate should be correspondingly more symmetrical between the top and bottom hemispheres. Interestingly, the flow rate through the top gap is less for the untrapped microbead than the trapped one, as fluid streams more easily laterally around the microbead.

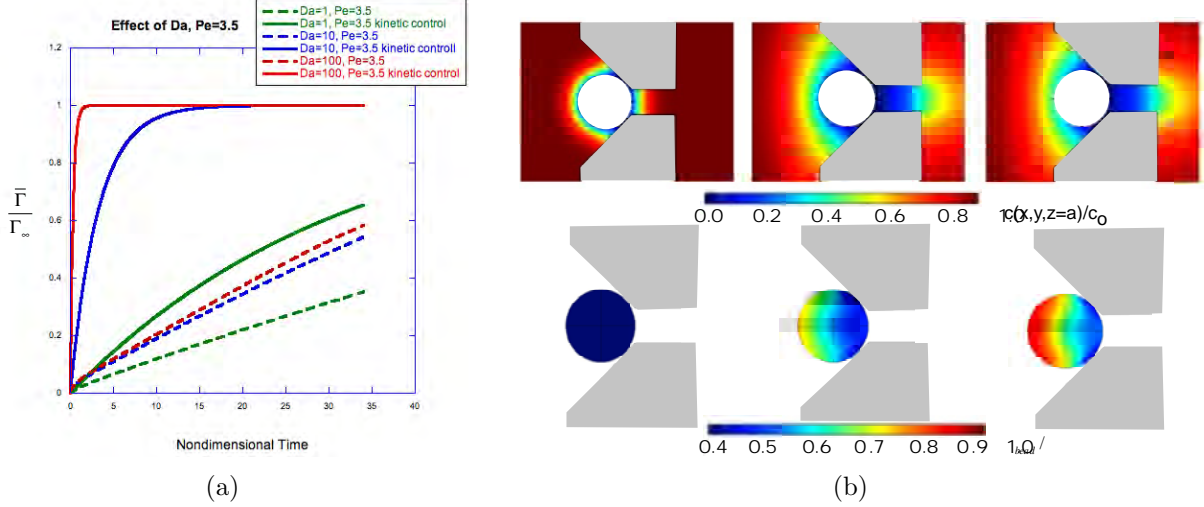


Figure 5.5: The binding of a target to the surface of a microbead in a trap (microbead “A”,  $y = Y_A$ ) for  $Pe = 3.5$  ( $\Omega = 32$ ,  $\Re = 0.2$ ): (a) The average nondimensional surface concentration on the surface of the microbead,  $\bar{\Gamma}/\Gamma_\infty$ , as a function of  $\tau$  for  $Da = 1, 10$  and  $10^2$  alongside the kinetic limits for these values of  $Da$ . (b) Target concentration diffusion zones for  $Da=10$  in the equatorial plane  $z = a$  and the projection of the surface concentration averaged for the upper ( $z > a$ ) and lower ( $z < a$ ) hemispheres of the microbead for  $\tau = .136, 20.4$  and  $30.26$  and  $Da = 10$ ,  $\Omega = 32$ ,  $\Re = 2 \times 10^{-4}$ .

### 5.2.3 Mass Transfer Simulations

The objective of the mass transfer calculations is to determine the nondimensional average concentration on the microbead surface ( $\bar{\Gamma}/\Gamma_\infty$ ) as a function of nondimensional time  $\tau$ . Aside from the geometric parameters of the unit cell, the average concentration is a function of  $\Omega$ ,  $Da$  and  $Pe$ , and therefore  $\frac{\bar{\Gamma}}{\Gamma_\infty}(\tau; Da, Pe, \Omega)$ . In most screening applications the concentration of the target is low enough or the binding capacity large enough so that  $\Gamma_\infty/c_o \gg a$ , and hence  $\Omega \gg 1$ . As a result, the accumulation of target on the surface, as is clear from eq. 5.6, occurs in accordance with a slower time scale  $\tau^* = \tau/\Omega$ , as the larger the value of  $\Omega$ , the slower is the binding rate. Rescaling eq. 5.6 with  $\tau^*$  reformulates the balance to become independent of  $\Omega$ , i.e.  $\frac{\partial \bar{\Gamma}}{\partial \tau^*} = \{\mathbf{n} \cdot \nabla \tilde{c}\}_{\text{bead}}$ . The second boundary condition, eq. 5.5, is independent of  $\Omega$  (as is the zero flux boundary condition on the trap and channel walls), and the convective diffusion equation (eq. 5.3) becomes  $\frac{1}{\Omega} \frac{\partial \tilde{c}}{\partial \tau^*} + Pe \tilde{\mathbf{v}} \cdot \nabla \tilde{c} = \nabla^2 \tilde{c}$ . Solutions of the rescaled equations are therefore independent of  $\Omega$  to leading order for  $\Omega \gg 1$ , as the transport dynamics in the bulk becomes quasi-stationary and dictated in time only by the change in flux on the surface in  $\tau^*$ . We find that the time derivative term in the bulk is only important in the earliest times in which the diffusion zone around the particle develops from a uniform concentration. Otherwise the bulk time derivative term is negligible, and as such, simulations integrated in  $\tau$  done for a particular value of  $Da$  and  $Pe$  and  $\Omega$  (assumed

much larger than one) can be used for another large value of  $\Omega$  by just rescaling time in the completed solution by the ratios of the two values of  $\Omega$ . Therefore for  $\Omega \gg 1$ , simulations varying  $\Omega$  are not necessary. In the general set of simulations presented here  $\Omega$  is fixed at 32 which is smaller than the experimental value, but is used to accelerate the integration time.

The target surface concentration on the microbead as a function of time ( $\Gamma(\tau)$ ) is determined by a balance between the Peclet ( $Pe = Ua/\mathcal{D}$ ) and Damkohler ( $Da = k_a\Gamma_\infty a/\mathcal{D}$ ) numbers.  $Pe$  is the ratio of the time scale for diffusion over a distance  $a$  normal to the surface ( $a^2/\mathcal{D}$ ) to the nominal scale for fluid to convect over the microbead surface (estimated as  $a/U$ ). Target proteins or smaller biomolecular ligands have molecular weights of order  $10^3 - 10^4$  and corresponding diffusion coefficients of  $\sim 10^2 \mu\text{m}^2/\text{s}$ ; for  $U \sim 10^2 - 10^4 \mu\text{m}/\text{s}$  and  $a$  of order  $10 \mu\text{m}$ ,  $Pe$  is of order  $1 - 10^3$ , which encompasses different transport behavior in the analyte stream. For  $Pe$  of order 1-10, diffusion zones (regions where the concentration is less than the inlet concentration  $c_o$ ) develop normal to the microbead surface and are of thickness of order  $a$ . However, for increasingly larger  $Pe$  ( $10^1 - 10^3$ ) the nominal convection time is much faster and the diffusion zone takes the form of asymptotically thin boundary layers. In the simulations we consider an order one value ( $Pe = 3.5$ ) with order  $a$  diffusion zones, and  $Pe = 3500$ , characteristic of thin diffusion zones and representative of our experiments. Values for the Damkohler number  $Da$ , the ratio of the characteristic kinetic flux to the surface ( $k_a c_o \Gamma_\infty$ ) to the characteristic diffusive flux on the particle length scale ( $\mathcal{D}c_o/a$ ), are dependent on the surface kinetics. For  $Da$  of order 1 or smaller, the kinetic rate step is of the same order or slower than diffusion, and the gradients in concentration in the diffusion zone are small as the zone is nearly at the bulk concentration  $c_o$ . In the limit  $Da \rightarrow 0$ , the bulk concentration around the microbeads becomes equal to  $c_o$ , and the transport becomes kinetically limited with the surface concentration independent of the position on the microbead surface and given by the solution to eqs. 5.5 - 5.6 after elimination of the diffusive flux term.

$$\frac{\Gamma^{\mathcal{K}}(\tau)}{\Gamma_\infty} = 1 - e^{-\frac{Da}{\Omega}\tau} \quad (5.7)$$

For larger  $Da$ , the kinetic step becomes faster and the concentration gradient is large in the diffusion zone. In the simulations, we study values of  $Da = 1$ , characteristic of the experiments, and two larger values of 10 and 100 representing large gradients in the diffusion zones.

Consider first a low value of  $Pe = 3.5$ . The average nondimensional target surface concentration  $\bar{\Gamma}$  (scaled by  $\Gamma_\infty$ ) on microbead ‘‘A’’ in a trap as a function of nondimensional time for  $Pe = 3.5$  and  $Da = 1, 10$  and  $10^2$  ( $\Omega = 32$ ) is given in Fig. 5.5(a) and compared to the



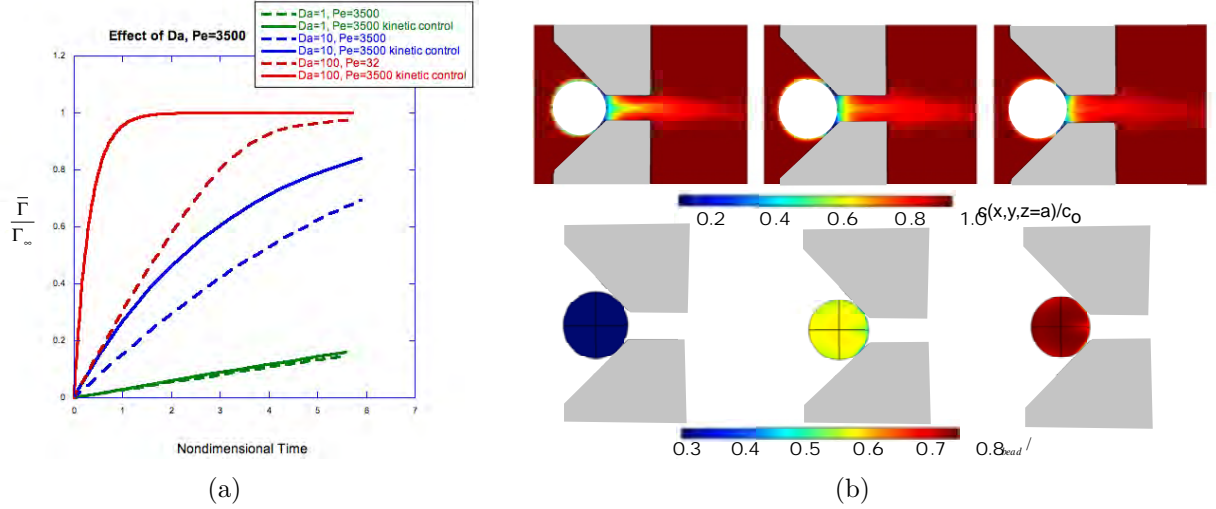


Figure 5.6: The binding of a target to the surface of a microbead in a trap (microbead “A”,  $y = Y_A$ ) for  $Pe = 3500$  ( $\Omega = 32$ ,  $\Re = 0.2$ ): (a) The average nondimensional surface concentration on the surface of the microbead,  $\bar{\Gamma}/\Gamma_\infty$ , as a function of  $\tau$  for  $Da = 1, 10$  and  $10^2$  alongside the kinetic limits for these values of  $Da$ . (b) Target concentration boundary layer for  $Da=10$  in the equatorial plane  $z = a$  and the projection of the surface concentration averaged between the upper ( $z > a$ ) and lower ( $z < a$ ) hemispheres of the microbead for  $\tau = .012, 2.9$  and  $5.4$  and  $Da = 10$ .

kinetic limits, eq. 5.7, for each of the values of  $Da$ . Due to the fact that the convective and diffusive fluxes are of the same order, large diffusion zones develop around the microbead, and this slows the transport rate of the target to the surface. As a result, for every value of  $Da$  in the figure, the binding rate is much slower than the corresponding kinetic limit which assumes the concentration is uniform and equal to  $c_o$  around the microbead. The diffusion zones around the microbead are depicted for  $Da = 10$  in Fig. 5.5(b) for three nondimensional times,  $\tau = .136, 20.4$  and  $30.26$  in the equatorial plane  $z = a$ . Diffusion brings target to the surface where it kinetically binds to the receptors, and the bulk concentration decreases in the zone in the direction normal to the microbead surface. As time progresses, target depletion becomes more pronounced and the gradients become sharper. This is especially evident at the downstream end of the microbead, where the concentration drops to zero through the opening at the back of the trap by  $\tau = 30.26$ . At this time the region in back of the trap is also depleted. This significant depletion is due to the reduced convective flow at the back of the microbead, relative to the front, and as a result the back side of the microbead lags behind the front in adsorption. This is shown in Fig. 5.5(b) which depicts the nondimensional surface concentration on the microbead surface ( $\Gamma/\Gamma_\infty$ ) as a projection on the equatorial plane  $z = a$  of the surface concentrations of the top and bottom hemispheres. For longer times (not shown), the saturation of the surface decreases the binding rate and the diffusive flux repopulates target in the diffusion zone. As a result the concentration

gradients in the zone decrease, and eventually fade away. The surface concentration at the back end of the microbead catches up with the front end as the surface concentration over the entire microbead surface approaches  $\Gamma_\infty$ .

The binding curves in Fig. 5.5(a) show clearly the effect of  $Da$  at this low (and fixed)  $Pe$ . For the highest value ( $Da = 10^2$ ), the binding rate is fast relative to diffusion and the sublayer concentration at the microbead surface ( $c_s$ ) falls far below  $c_o$ , and sharp concentration gradients develop in the diffusion zone. As a result, the binding rate is much reduced very far from the kinetic limit where  $c_s = c_o$ . As  $Da$  decreases to 10, the kinetic limit slows down (in accordance with eq. 5.7), as does the simulated binding rate. At  $Da = 10$ , the binding rate curve is however closer to its kinetic limit because the reduced kinetic rate does not deplete the sublayer of target as dramatically as when  $Da = 10^2$ . Finally when  $Da = 1$ , the simulated curve is even closer to the kinetic limit, but is still apart due to the diffusion barriers due to the large diffusion zones for  $Pe = 3.5$ . In fact, a  $Da$  less than 0.1 is required for the simulated curves to overlap the kinetic curve for  $Pe = 3.5$ .

When  $Pe$  is increased to 3500, a thin concentration boundary layer develops over the microbead surface due to the higher convective rate relative to the diffusion flux, which decreases the diffusional resistance to the target transport by reducing the thickness of the diffusion zones, and increases the rate of binding (Fig. 5.6). The diffusion zone is shown in Fig. 5.6(b), again for  $Da = 10$ , but for earlier nondimensional times  $\tau = .012, 2.9$  and  $5.4$  than those shown for the smaller  $Pe$ . The boundary layer is very thin, except at the very backend of the microbead where the slow convection through the trap's backend opening leads to some depletion. Because of the thin boundary layer circumscribing most of the microbead, the kinetic binding on the microbead surface is more uniform than in the case of  $Pe = 3.5$ . The backend adjoining the trap opening lags only slightly behind. The surface concentration on the lateral sides of the microbead which adjoin the trap side walls also lag behind, due to the reduced convection through the side gaps between the trap walls and the microbead which enlarges the boundary layer. The boundary layer on the underside is also enlarged by the reduced convection between the microbead and the bottom wall of the flow cell. Because of this, and the fact that the gap between the top of the channel and the bead is large ( $\approx 20 \mu\text{m}$ ), and the boundary layer fits within the gap, the top ( $z > a$ ) and bottom hemispheres have different average concentrations as shown in Fig. 5.7 for  $Pe = 3500$  and  $Da = 10^2$ , where the more unobstructed flow in the top gap results in a larger binding rate. This difference becomes reduced as  $Da$  decreases, and the kinetic limit is approached, since the sublayer concentration becomes uniform. In the case of small  $Pe$  (3.5), the difference in binding rates between the hemispheres is not very pronounced because of the large diffusion zone which wraps around the trap creating an overall barrier to transport.

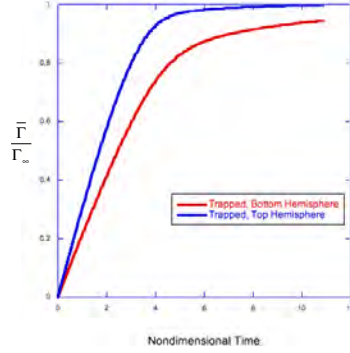


Figure 5.7: Asymmetric binding to the top and bottom hemispheres of a trapped microbead (“A”) due to reduced convection at the bottom half of the bead which rests on the channel floor.  $Pe = 3500$ ,  $Da = 10^2$ ,  $\Omega = 32$ ,  $\mathfrak{Re} = 2 \times 10^{-1}$ .

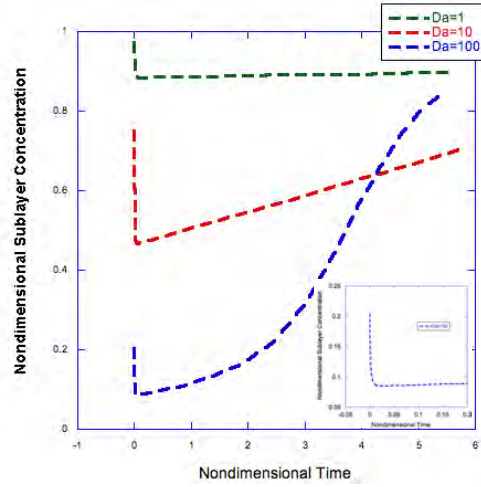


Figure 5.8: The average nondimensional sublayer concentration  $\bar{c}_s/c_o$  at the surface of a trapped microbead “A”, as a function of nondimensional time for  $Pe = 3500$ ,  $Da = 1, 10$ , and  $10^2$ ,  $\Omega = 32$  and  $\mathfrak{Re} = 2 \times 10^{-1}$ . The inset details the sublayer concentration immediately after the target analyte is introduced for  $Da = 100$ .

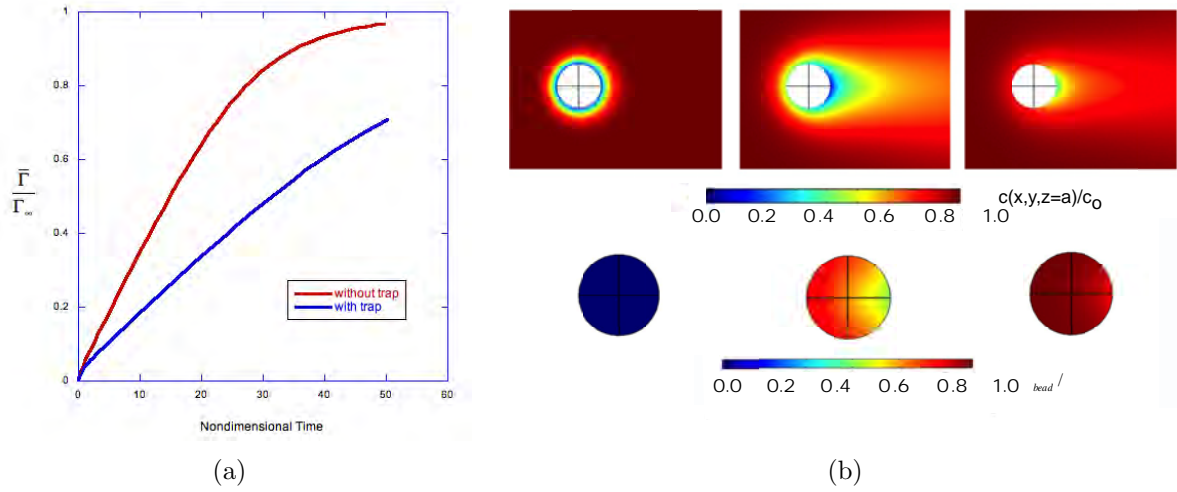


Figure 5.9: The binding of a target to the surface of an untrapped microbead (“A”) for  $Pe = 3.5$  and  $Da = 10$  ( $\Omega = 32$ ,  $\mathfrak{Re} = 2.0 \times 10^{-4}$ ): (a) The average nondimensional surface concentration on the surface of the microbead,  $\bar{\Gamma}/\Gamma_\infty$ , as a function of  $\tau$  for  $Da = 10$  and comparison to a trapped microbead for the same  $Pe$ ,  $Da$ ,  $\Omega$  and  $\mathfrak{Re}$ . (b) Target concentration boundary layer for  $Da = 10$  in the equatorial plane  $z = a$  and the projection of the surface concentration averaged between the upper ( $z > a$ ) and lower ( $z < a$ ) hemispheres of the microbead for  $\tau = 0.136, 20.4$  and  $32.6$ .

In Fig. 5.6(a),  $\Gamma(\tau)/\Gamma_\infty$  is given for  $Da = 1, 10$  and  $10^2$  and  $Pe = 3500$ , and it is clear, on comparison with Fig. 5.5(a) for  $Pe = 3.5$  that binding rates are much faster for the same values of  $Da$ . In this case, because of the reduced diffusional resistance, the binding curve at  $Da = 1$  now overlaps the kinetic curve. This overlap represents the case where the binding is controlled solely by the target-probe kinetics, and is a regime which has the particular advantages when these platforms are used to measure binding constants, since the kinetic binding data only has to be regressed against the analytic kinetic curve (eq. 5.7), without the need to model the convective diffusion. In this high Peclet number regime, a general criteria can be developed through scaling arguments to identify the value of  $Da$  below which the transport becomes kinetically limited. When a thin concentration boundary layer develops around the microbead, the boundary layer thickness,  $\delta$  at the back end can be estimated as the distance the target should be away from the surface for which the time to move along the microbead,  $a/U_\delta$  (where  $U_\delta$  is the velocity at a distance  $\delta$  from the microbead) becomes equal to the time required for the target to diffuse to the surface,  $\delta^2/\mathcal{D}$ . The velocity can be estimated as the average velocity gradient (or shear rate) evaluated at the microbead surface,  $\bar{\dot{\gamma}}$  multiplied by  $\delta$ , and therefore  $\frac{a}{\bar{\dot{\gamma}}\delta} = \frac{\delta^2}{\mathcal{D}}$  or  $\frac{\delta}{a} \sim \left[ \frac{\mathcal{D}}{a^2 \bar{\dot{\gamma}}} \right]^{1/3}$ . For the well studied case of a fixed microbead in an infinite medium subject to a uniform flow  $U_\infty$  with concentration  $c_o$  far from the bead, the average shear rate  $\bar{\dot{\gamma}} \sim U_\infty/a^{202}$ . The average shear rate over the surface of microbeads in a microchannel either situated in a trap or (ideally) fixed to a

surface is a more complicated flow than the unbounded case due to the effect of the channel and trap walls. However, to a first approximation in order to construct a simple criterion, we assume that  $\bar{\gamma} \sim U/a$  so that  $\frac{\delta}{a} \sim \left[ \frac{1}{Pe} \right]^{1/3}$  for  $Pe \gg 1$ . The diffusive flux to the surface, for  $Pe \gg 1$ , through the boundary layer scales as  $\frac{\mathcal{D} \{c_o - \bar{c}_s\}}{\delta}$  (where  $\bar{c}_s$  is the average sublayer concentration on the microbead surface); equating this flux to the maximum kinetic flux ( $k_a \Gamma_\infty$ ) defines a scale for the (minimum) sublayer concentration at the earliest times,  $\frac{\bar{c}_{s,min}}{c_o} \sim \frac{1}{1 + \frac{Da}{Pe^{1/3}}}$ . When  $Da/Pe^{1/3} \ll 1$ , the sublayer concentration is equal to the farfield concentration, the process is kinetically controlled and the binding is given by eq. 5.7. To validate this criterion, note first Fig. 5.8 which plots for microbead ‘‘A’’ the average nondimensional sublayer concentration  $\bar{c}_s$  as a function of nondimensional time for  $Pe = 3500$  for  $Da = 1, 10$ , and  $10^2$ . For the largest value of  $Da$  the large kinetic binding rate relative to diffusion leads to a rapid drop in the sublayer concentration to a value of approximately 0.1, and the sublayer slowly recovers to one as the surface saturates with target and the concentration in the diffusion zone relaxes. As  $Da$  decreases, the slowing of the kinetic rate decreases the binding, and the initial reduction in the sublayer concentration in the earliest times is much smaller than the case for  $Da = 10^2$ . The scaling evaluation for the minimum sublayer concentration,  $\frac{\bar{c}_{s,min}}{c_o} \sim \frac{1}{1 + \frac{Da}{Pe^{1/3}}}$  gives 0.9, 0.6 and 0.1 for  $Da = 1, 10$ , and  $10^2$ , respectively, which is in very good agreement with the simulation minima as given in Fig. 5.7. The criteria for kinetic control  $Da/Pe^{1/3} \ll 1$  is also validated in the simulations in Fig. 5.6, where it is clear that for the three values of  $Da$ , 1, 10, and  $10^2$ ,  $Da/Pe^{1/3} \ll 1 = 0.06, 0.6$  and  $6.6$  respectively and only the  $Da = 1$  value satisfies the criteria and is in fact the only curve coincident with the kinetic limit eq. (5.7).

Alternatively when  $Da/Pe^{1/3} \gg 1$ , the sublayer concentration tends to zero, at least initially, and the target flux to the surface is controlled solely by the diffusive mass transfer. The characteristic time for the target to bind to an equilibrium surface density ( $t_{eq,\mathcal{D}}$ ) is given by  $t_{eq,\mathcal{D}} \frac{\mathcal{D}c_o}{\delta} \sim \Gamma_\infty$  or  $\tau_{eq,\mathcal{D}} = \frac{t_{eq,\mathcal{D}}}{h^2/\mathcal{D}} \sim \frac{Da}{Pe^{1/3}}$  where  $\tau_{eq,\mathcal{D}}$  denotes a nondimensional completion time scaled by the diffusion time across the channel ( $t_{\mathcal{D}}$ ). For the case of  $Da = 10^2$  in Fig. 5.6, which is the only value of the Damkohler number large enough to satisfy  $Da/Pe^{1/3} \gg 1$ ,  $\tau_{eq,\mathcal{D}} \approx 6.6$  which is in excellent agreement with the simulation equilibration time. Bruus et al<sup>199</sup>, for a patch of probes on one wall of a two dimensional microfluidic channel, have examined, by comparison to numerical simulations, the validity of reproducing the entire binding curve of the target to the patch for  $Pe \gg 1$  by a boundary layer approximation in which  $\mathcal{D} \left\{ \frac{c_o - \bar{c}_s}{\delta} \right\} = k_a \Gamma_\infty \left\{ 1 - \frac{\Gamma}{\Gamma_\infty} \right\} - k_d \Gamma$  with the boundary layer thickness given by  $Pe^{-1/3}$  (see also the two compartment models for transport to surface probes in a

channel<sup>203–211</sup>). Bruus et al find for large  $\Omega$ , small  $Da$  and large  $Pe$  the approximation is most accurate. We find that simulating the binding curves of Fig. 5.6 for binding of target to microbeads in traps in our parameter space gives only qualitative agreement, although the equilibration is captured accurately. This is probably due to the more complicated nature of the flow in the case of the entrapped microbeads.

To assess the effect of the trap on the mass transfer of the target to the microbead probe surface, simulations of the binding are presented for microbeads situated in the same array as in Fig. 5.2, but without the traps. Consider first the case of  $Pe = 3.5$ , where the diffusion zone is very large, and in the presence of a trap, extends beyond the trap itself as shown for  $Da = 10$  (Fig. 5.5(b)). For the very same conditions ( $Pe = 3.5$ ,  $Da = 10$ ,  $\Omega = 32$ , and  $\mathfrak{Re} = 2.0 \times 10^{-4}$ ) and the same nondimensional times (0.136, 20.4 and 32.6), Fig. 5.9(a) shows that the diffusion zone around the unobstructed microbead is more compact. The concentration gradients at the later times are not as sharp, and less depletion is evident at the back end of the microbead. What becomes clear in comparing Figs. 5.5(a) and 5.9(a) is that the trap obstructs the transport to the back end completely at low  $Pe$ , leading to a complete depletion in the aperture at the back end of the trap. When unobstructed, the transport is not unlike a bead in an infinite medium, where some depletion at the back end would be expected due to the larger boundary layer at the downstream face of the microbead. The nondimensional surface concentration on the microbead surface (again a projection of the surface concentration averaged between the top ( $z > a$ ) and bottom ( $z < a$ ) hemispheres) shows a simple asymmetry with the back end lagging behind the front because of thinner boundary layer at the upstream face of the microbead.

The more compact diffusion zone in the case of open rather than trapped microbeads also leads to a significantly more rapid binding rate, as shown in Fig. 5.9(a) which compares the two transport geometries for  $Pe = 3.5$ . In fact, this difference increases with the  $Da$  number, as the diffusion limitation becomes more rate determining due to a decrease in the sublayer concentration. In the opposite limit, as  $Da \rightarrow 0$  and the sublayer concentration approaches the inlet concentration, both the trapped and untrapped microbeads approach the kinetic limit. For this value of  $Pe$ ,  $Da$  is required to be as small as 0.1 for overlap, so differences exist for  $Da$  larger than this value.

When the  $Pe$  number is increased to 3500, the diffusion zone around a trapped microbead takes the form of a thin concentration boundary layer which hugs the microbead and lies within the trap except at the back face and bottom part of the microbead where the bead contacts the trap walls. The presence of the enclosing trap is therefore not as important in the high Peclet number regime, and as shown in 5.10, for identical conditions ( $Pe = 3500$ ,  $\Omega = 32$ , and  $\mathfrak{Re} = 2.0 \times 10^{-1}$ ), the kinetic binding rate to the unobstructed microbeads

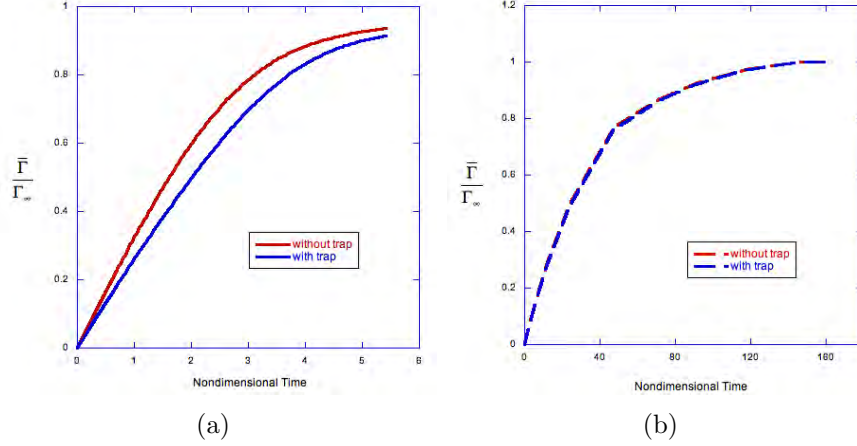


Figure 5.10: Comparison of the binding rate for trapped and untrapped microbeads “A” in the array in the high Peclet number regime ( $Pe = 3500$ ) for (a)  $Da = 10^2$  and (b)  $Da = 1$ . ( $\Omega = 32$  and  $\Re = 2.0 \times 10^{-1}$ ).

is only marginally faster at  $Da = 10^2$  (5.10(a)) and becomes equal to the binding rate for the trapped microbead by  $Da = 1$  (Fig. 5.10(b)), at which point both agree with the kinetic equation (eq. 5.7).

## 5.3 Experimental Binding Assay

The aim of the experiments is to first demonstrate a binding assay with the hydrodynamically assembled microbead library platform of Fig. 5.1, using as a prototype the conjugation of fluorescently labelled NeutrAvidin as the target analyte to biotin (its binding partner) displayed on the microbead surface, and secondly to measure the surface kinetic rate constant. We illustrate how the flow rate of the assay (or equivalently the  $Pe$  number) can be selected, using the simulations as a guide, so that the transport of target is kinetically controlled, and a kinetic rate constant can be obtained by comparing the measurements to a simple kinetic expression (e.g. eq. 5.7) without having to solve for the target’s convective-diffusion equations.

### 5.3.1 Materials and Methods

The fluorescently labeled protein, fluorescein conjugated NeutrAvidin (Neutravidin-FITC), was obtained from Thermo Fisher Scientific, Inc. NHS-PEG<sub>4</sub>-biotin and NHS-PEG<sub>4</sub> (N-hydroxysuccinimide esters linked to four polyethylene glycol (PEG,  $-(CH_2CH_2)_2O-$ ) groups and capped with biotin or a methyl group) were purchased from Pierce Corp. Toluene, acetone, isopropanol, methanol (99.8%) and dimethylformamide (DMF) were obtained from Alfa

Aesar (HPLC Grade). Phosphate buffered saline buffer (PBS, pH=7.4), hydrogen peroxide, ammonium hydroxide and hydrochloric acid were obtained from Fisher Scientific. Amino-propyltrimethoxysilane ( $\text{NH}_2(\text{CH}_2)_3\text{Si}(\text{OCH}_3)_3$ , APS) and PEG silane, 2-(methoxy(poly-ethyleneoxy)propyl trimethoxysilane ( $\text{CH}_3(\text{CH}_2\text{CH}_2\text{O})_n(\text{CH}_2)_3\text{Si}(\text{OCH}_3)_3$ ,  $n=6-9$ ) were obtained from Gelest. DI water with a resistivity of 18 M-cm was obtained from a Millipore water filtration system. Negative tone SU8-2050 photoresist and developer were purchased from Microchem. Sylgard 184 elastomer base and curing agent was purchased from Dow Corning as a kit. All chemicals were used as received except for the PBS which was filtered with 0.2  $\mu\text{m}$  syringe filters. Soda lime glass calibration microbeads, 42.3  $\mu\text{m}$  in diameter with a 1.5  $\mu\text{m}$  standard deviation in the size distribution, were obtained from Thermo Fisher Scientific, Inc. Test grade single crystal polished silicon wafers (3 inch in diameter) were obtained from Silicon Quest Inc. Polyethylene tubing (1.5 mm OD, 1 mm ID) was obtained from VWR. Dye removal resin column kits were obtained from Thermo Fisher Scientific (Pierce Protein Biology Products).

### 5.3.2 Microbead Functionalization

N-hydroxysuccinimide ester (NHS)-conjugated reagents are commonly used to label proteins, reacting with primary amine groups to form an amide bond between the protein and the reagent<sup>212,213</sup>, and this reaction is used here to functionalize the surface of glass microbeads with mixed monolayers of PEG and biotin by first using a silane reaction to attach amine groups to the hydroxylated surface of the glass microbeads. Soda lime glass microbeads (42.3  $\mu\text{m}$  in diameter) are first washed in an aqueous solution consisting of 4 weight percent hydrogen peroxide and 4 weight percent ammonium hydroxide to remove hydrophobic surface contaminants. The solution is heated for 10 min. on a hotplate with vortexing, decanted, and the beads are resuspended in DI water. This is repeated three times, and the beads are then washed similarly with an aqueous solution consisting of 4 weight percent hydrogen peroxide and 0.4M HCl. After resuspension in DI water, the microbeads are dried in a convection oven for 12 hours at 85°C. To attach amine groups to the microbead surface, the washed and dried microbeads (30 mg) are added to 10 ml of a 5mM solution of aminopropyltrimethoxysilane (APS) in toluene for 1hr 30min under stirring. (This concentration is 100 times larger than the concentration needed to graft to a coverage of 225  $\text{\AA}^2$  per amine, corresponding to the measured maximal amine grafting densities, see the discussion below.) In the presence of water, either on the surface or in toluene, the trijmethoxy groups attached become hydrolyzed to hydroxyl groups which react with the surface silanols to form siloxane bonds producing a self-assembled monolayer (SAM) terminated with a primary amine. To remove bounded



but unreacted APS from the microbead surface, the microbeads are washed and sonicated with toluene. They are then centrifuged and washed twice with dimethylformamide (DMF).

The probe molecule, biotin, is attached to the grafted amine surfaces of the microbeads by reacting the amines on the microbead surface with NHS derivatized biotin (NHS-PEG<sub>4</sub>-biotin) in solution to form an amide linkage of the biotin to the amine. The surface density of the biotin probe ( $\Gamma_p$ ) can be varied by reacting with mixtures of NHS-PEG<sub>4</sub>-biotin and NHS-PEG<sub>4</sub>. The resulting surface of the microbead displays PEG-biotin and PEG, with equal subunits of PEG, so that the biotin extends just beyond the PEG layer making it accessible to the NeutrAvidin analyte in solution. NHS-PEG linkers are utilized because the resulting background PEG layer resists the non-specific adsorption of protein<sup>214,215</sup> (in particular the target NeutrAvidin), so that the target recorded on the microbead surface is only due to the direct binding of the biotin to NeutrAvidin. For mixed functionalization, 30 mg of microbeads are suspended in 10 ml of a solution of NHS-PEG<sub>4</sub>-biotin and NHS-PEG<sub>4</sub> in DMF, with a total concentration of the NHS ester of 1 mg/ml solution, and with the molar ratio of NHS-PEG<sub>4</sub>-biotin and NHS-PEG<sub>4</sub> varied with stirring overnight. (This total concentration is enough to cover all the amine sites by a factor of 100.) The microbeads are then washed three times with DI water and stored in a refrigerator at 4°C until used.

### 5.3.3 Device Design and Fabrication

The trapping course incorporated in the microfluidic cell, and used to array the microbeads into a probe library, consists of a staggered array of “V” shaped enclosures as shown in Fig. 5.2 and directly modeled in the simulations. The trapping course is set in a wide channel of height 60  $\mu\text{m}$  which contains an open space upstream for an inlet port to inject the microbeads. The wide channel is connected upstream by a narrow channel to an inlet for introducing the analyte, and connected downstream to an opposing narrow channel to an outlet for collecting microbeads and analyte. The cell is fabricated in two layers, a bottom part containing the features of the trapping array, connecting network and inlet and outlet ports which is imprinted on a monolith by molding against a master. The second part is a glass slide which is bonded to the face of the molded bottom part containing the features to enclose the channels and the trapping array. The molded part is made from the elastomer polydimethylsiloxane (PDMS) using soft lithography. The master, with the negative features of the fluidic network, is made from a photoresist using lithography. The bottom part is molded from the master using the two component heat curing system from Dow Corning Sylgard 184; the ratio of base to elastomer is 10:1 by weight. The photoresist master is placed at the center of a Petri dish, and the base-curing agent mixture is poured over the master,

and allowed to sit under vacuum for 30 min to release bubbles sticking to the bottom of the master holes that would eventually become the PDMS trap. The mixture is then cured by heating in an oven at  $65^{\circ}\text{C}$  for one hour. The resulting elastomer is subsequently peeled off of the master, and cut into individual cells. Inlet and exit ports are punched through the molded face to the backside of the monolith, and an access hole is also punched in the space upstream of the trapping array for the introduction of the microbeads. The elastomer and glass slide are sealed by bringing the faces in conformal contact to form siloxane linkages after oxygen plasma treating their open faces (Harrick Plasma Cleaner). The inside surfaces of the flow channels and the interior surfaces of the traps are functionalized with a PEG silane to prevent nonspecific adsorption.

### 5.3.4 Microbead Arraying

Microbeads are arrayed in the microfluidic device by introducing them through the injection port in front of the traps. The prepared device is submerged in a beaker of water, which is placed in a dessicator chamber under mild vacuum to extract air bubbles in the device. After the air bubbles have been removed by visual inspection, the device is kept under water. A 2.0 ml aliquot of a microbead suspension is loaded in a glass gas tight syringe, and tubing is slipped over a needle at the end of the syringe. The microbeads are allowed to settle back against the plunger of the syringe with the syringe orientated horizontally, and the tubing extending from the syringe is then filled with water by depressing the plunger. The tubing is then inserted into the access hole above the staging area in front of the trapping array. The syringe is maintained in a horizontal position so no beads are yet introduced into the device. The inlet port of the cell is then connected to a target analyte filled syringe by inserting the tubing into the access port on the device and slipped over a needle attached to the syringe. Tubing is inserted into the exit hole. When all the ports are connected to the tubing, the device is gently removed from the water, dried with a wipe and placed on the stage of a optical microscope. The syringe containing the analyte target is placed in a syringe pump (Harvard Apparatus PHD). The microbeads are introduced into the device by raising the syringe to a vertical orientation to allow microbeads to settle at the bottom of the syringe. The syringe plunger is then depressed to push the microbeads through the obstacle course, delivering 0.5 ml in approximately 30 sec for a flow rate of  $10^3 \mu\text{l}/\text{min}$ . The filling of the course with the microbeads is observed through optical microscopy by visual. After injection, the syringe is placed back in a horizontal position, the beads return to the side and back end of the syringe and the plunger is depressed slowly to flow DI water through the course to remove the few beads that are untrapped.

### 5.3.5 Screening Assay and Fluorescence Imaging of NeutrAvidin-FITC Binding to the Biotinylated Microbeads

NeutrAvidin is a homotetrameric protein ( $MW = 60000$ ), consisting of four identical subunits, each of which contains a receptor pocket site for the insertion of the small molecule biotin ligand ( $MW = 244$ ). NeutrAvidin is the deglycosylated form of the naturally occurring protein Avidin, with a near neutral pI equal to 6.3. X-ray studies indicate that the sites are barrel shaped enclosures constructed from  $\alpha$  helices, and arranged in the tetramer so that two sites are on one face of the protein, and two sites are on an opposite face, with each face having an area of  $\mathcal{A}_t = 3025 \text{ \AA}^2$ . Because of the large area of the binding face of the protein, the insertion of the surface biotin into the barrel site can cover other surface ligands and make them unavailable for binding another protein if the biotin probe density  $\Gamma_p$  is larger than the inverse of the protein binding face.

The biotin probe density on the surface of the microbeads is determined firstly by the density of the amine groups grafted to the surface by the silane reaction, and secondly by the ratio of the reagents NHS-PEG<sub>4</sub>-biotin and the NHS-PEG<sub>4</sub> which are mixed in solution and react with the surface amines to link either PEG<sub>4</sub> or PEG<sub>4</sub>-biotin to the surface via an amide bond. The surface density of APS-silane grafted amines on glass which are available for reaction with NHS has been measured in 2.19(b) by first reacting NHS, linked to a disulfide, to surface grafted amines on glass slides, and then attaching a fluorescent group to the disulfide. This group is then removed into solution by reduction, and the fluorescence in solution is measured to obtain the number of amine groups which reacted with the NHS-disulfide. They find that aminated surfaces prepared by APS silanization in a toluene solvent (as here) results in surface densities of approximately 20 amine sites per 100 nm<sup>2</sup> (500  $\text{\AA}^2/\text{site}$ ). In a second study, the surface density of APS-silane grafted surface amines on silica nanoparticles was measured by directly reacting the amine with a isothiocyanate linked to a fluorescent group, and then measuring the fluorescence of the nanoparticles to quantify how many fluorescent molecules had bound to the surface of the particles. In this case the silanes were grafted onto the particles from an ethanol solvent, and they find a larger surface density of 44 amine sites per 100 nm<sup>2</sup> (227  $\text{\AA}^2/\text{site}$ ). In either case, the surface density is much smaller than the theoretical limit of the maximum packing for the grafted amines, which, based on the cross section of the propyl chain of APS in an all trans configuration, is 20  $\text{\AA}^2$ , or 500 amine sites per 100 nm<sup>2</sup>. (This is also approximately the surface density of hydroxyl groups on silica 2.19(b).) The smaller surface densities of the grafted amines compared to the maximum packing is attributed to the reduced intermolecular cohesion of the propyl group which does not allow for a high surface density self assembled monolayer

(SAM) to form, and hydrogen binding of grafted amines to surface hydroxyl groups which blocks the grafting of additional APS to the surface 2.19(b).

In our silane functionalization of the glass microbeads, the concentration of the APS silane solution used is 100 times larger than the concentration necessary to cover the microbeads assuming the maximum attainable coverage of 44 sites per 100 nm<sup>2</sup> or 227 Å<sup>2</sup> per amine, so we assume this maximum amine coverage is achieved. Although this coverage is low, the area occupied per amine molecule is still much larger than the binding face of NeutrAvidin, so that if every amine site was linked to a biotin by the hydroxysuccinimide reaction with NHS-PEO<sub>4</sub>-biotin, protein bound to a surface biotin would block or sterically hinder other unoccupied biotin probe sites from binding protein. (Note that the NHS-PEO<sub>4</sub>-biotin links to the surface amine, the oligomeric ethylene oxide chain forms a helical configuration from the surface amide bond with a cross section of approximately 20 Å<sup>2</sup> per molecule, which is much smaller than the area per grafted amine, so the PEO<sub>4</sub> does not overlap other surface amines.) Thus to model the binding kinetics of NeutrAvidin to biotinylated glass microbeads with the highest probe densities ( $\Gamma_p = 20 - 44$  biotin molecules/100 nm<sup>2</sup>), the effect of steric hindrance should be incorporated in eq. 5.4, as the fraction of biotin sites available for binding,  $\phi$ , is not equal to the fraction of unbound sites. If the biotin probe density is reduced so that the area per biotin probe is much larger than the binding face of NeutrAvidin (i.e.  $1/\Gamma_p > \mathcal{A}_t$ ), then when the protein binds to the surface biotin it does not obstruct unbound probes, and the available fraction for binding is equal to the fraction of unbound probes (Langmuir kinetics,  $\phi = 1 - \frac{\Gamma}{\Gamma_p}$ , and the maximum surface concentration of the target,  $\Gamma_\infty$ , equals the probe density  $\Gamma_p$ ). Here we study this low probe density limit to insure Langmuir kinetics, and lower the biotin probe density by linking the amines on the surface, through the hydroxysuccinimide reaction, to PEG<sub>4</sub> as well as PEG<sub>4</sub>-biotin by reacting the microbeads with a mixture of NHS-PEG<sub>4</sub> and NHS-PEG<sub>4</sub>-biotin in a molar ratio of 1:1000 (NHS-PEG<sub>4</sub> to NHS-PEG<sub>4</sub>-biotin). These molecules are identical, except for the biotin moiety, which is distal to the NHS reacting center, and therefore the reaction rates to the surface amines should be proportional to the bulk concentrations. As such, the ratio of the surface concentration of PEG<sub>4</sub> linked to the surface amines, to the surface concentration of linked PEG<sub>4</sub>-biotin should be in the ratio of their bulk concentrations. Therefore the surface probe density of the biotin is 1/1000 of the density of the amine sites, or a (biotin) area per molecule, which is 1000 times larger than the amine area per molecule of 227 - 500 Å<sup>2</sup>, which in turn is much larger than the binding face of NeutrAvidin.

The target analyte, NeutrAvidin, fluorescently labeled with fluorescein (NeutrAvidin-FITC), is flowed through the cell, and the accumulating fluorescence on the surface of the microbeads functionalized with the biotin surface probes are obtained using epifluorescence

measurements on an inverted Nikon Eclipse TIE microscope with a motorized stage for scanning different areas of the trapping array, a 10x/NA=0.3 air objective, a filter cube for measurements of FITC luminescence (excitation filter  $470 \pm 40$  nm, emission (barrier) filter  $525 \pm 50$  nm) and a high sensitivity digital camera (DigiSight, Nikon). The microfluidic cell is placed with the glass slide down, so that the array is observed through the optically more transparent thin glass slide than the PDMS half of the monolith. Images of the microbead array fluorescence at different regions in the assembled array were obtained in regular 10 min time intervals from a starting point ( $t=0$ ) when the analyte flow is first introduced into the array for a period of approximately 1.5 hr. The NeutrAvidin-FITC flow rate is 100  $\mu\text{l}/\text{min}$  and the concentration of protein is 500 ng/ml, and images were recorded for approximately 1.5 hr which is the observed time necessary for the protein binding to saturate and the fluorescence on the microbead surface to become steady. NIH imaging software is used on the time sequence of images of the array luminescence to encircle the fluorescence on individual microbeads in the array, and sum the recorded intensities of the pixels in the encircled regions to obtain the individual fluorescence of each encircled microbead. For each microbead whose fluorescence is recorded in this way, the integrated intensity at each time is divided by the steady luminescence of the microbead, obtained by averaging the integrated intensity of the microbeads over the last few minutes of the 1.5 hr of the experiment, where the intensity appeared approximately constant. Assuming the surface concentration of the labelled protein is linear in the measured fluorescence, the quotient of the measured microbead fluorescence at time  $t$  to the asymptotic saturation value for long time is equal to the average surface concentration ( $\bar{\Gamma}(t)$ ) divided by the maximum packing concentration ( $\Gamma_\infty$ ). Each experiment involves the recording of the fluorescence for several microbeads at each time interval; these individual recordings (divided by the asymptotic (saturation) values for each microbead) are averaged and plotted as  $\Gamma_\infty$  as a function of time, with error bars established from the standard deviations of the individual microbead measurements. The result for the 0.1% NHS-PEG<sub>4</sub>-biotinylated microbeads (from three parallel experiments) is plotted in Fig. 5.11 (blue solid line) along with the error bars obtained from the standard deviations of the measurements.

### 5.3.6 Comparison with Simulations

Simulations are constructed to be in congruence with the experiments and follow the representation of the array as presented earlier in which one unit cell of four rows is modelled (Fig. 2). The physical parameters of the analyte solutions are set to the same as the experiment: NeutrAvidin diffusion coefficient,  $D = 6 \times 10^{-11} \text{m}^2 \text{sec}^{-1}$ ,  $C_0 = 8.33 \times 10^{-6} \text{mol m}^{-3}$

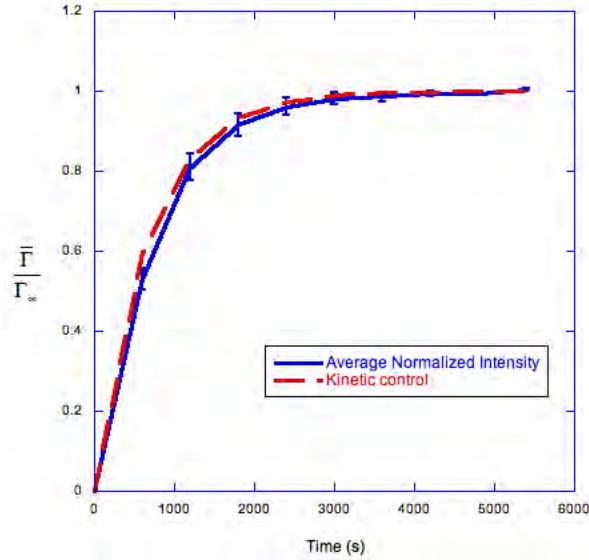


Figure 5.11: A comparison of simulation data with experiment data for the dynamic response of the microbead array. The blue solid line with error bars shows the normalized intensity of the fluorescence of NeutrAvidin-FITC bound to 0.1 mol % NHS- PEG<sub>4</sub>-Biotin microbeads as a function of time for a solution concentration of 500 ng/ml and a flow rate of 100  $\mu\text{l}/\text{min}$ . The red line shows the simulation fit, for a value of  $k_a = 180 \text{ m}^3 \text{ mole}^{-1} \text{ sec}^{-1}$ , and the kinetic limit (red) overlies the finite element simulation.

and screening assay perfusion flow rate of  $10^2 \mu\text{l}/\text{min}$  (average velocity  $U = 10^{-2} \text{ m}/\text{sec}$ ). As we noted, for a 1/1000 molar ratio of NHS-PEG<sub>4</sub> – *biotin* to NHS-PEG<sub>4</sub> the molecular saturation coverage of the protein is equal to the surface density of the biotin, and the kinetics can be described by a Langmuir model in which the bound proteins do not interact. For 0.1 mol % NHS-PEG<sub>4</sub>-Biotin, assuming an area per molecule of the amine binding sites of  $200 \text{ \AA}^2$ ,  $\Gamma_{\infty} = 8.3 \times 10^{-10} \text{ mol} \cdot \text{m}^{-2}$ . The Peclet number  $Pe$  based on the radius of the bead ( $Pe = Ua/D$ ) is equal to 3500, and  $\Omega$  based on the initial concentration of NeutrAvidin-FITC ( $\Omega = \frac{\Gamma_{\infty}}{c_0 a}$ ) is equal to 4.8. The Damkohler number  $Da = \frac{k\Gamma_{\infty}a}{D}$  is then varied until they are in agreement with the experiments and we find  $Da = 0.05$  which corresponds to  $k_a = 180 \text{ m}^3 \text{ mol}^{-1} \text{ s}^{-1}$ , (see Fig. 5.11 (red dot line)). Also in the figure is shown the purely kinetically controlled curve, which as expected from the general simulations for a value of  $Da$  much less than one and  $Pe$  of order  $10^3$ , overlap the mixed simulation curve as the process under these conditions is kinetically controlled.

### 5.3.7 Summary and Conclusions

In this study, we have examined the mass transfer of a target molecule to a microbead probe library which was incorporated in a wide channel of a microfluidic cell. The library is constructed by conjugating the probe molecules to the microbead surface, and assembling the

microbeads in an array layout by hydrodynamically capturing the microbeads in a trapping course situated in the channel. The traps are V-shaped, half-open enclosures with the open end facing the flow, and are arranged in a staggered configuration. The enclosures span the entire height of the channel, which is just slightly larger than the microbead diameter, and are sized to sequester only one microbead, so that the trap course arrangement serves as the template for arraying the microbeads, and keeping them in place. The traps have an aperture opening at the back end to allow flow over the surface of the microbead. Assaying the binding interaction of a target with the probe library is undertaken by flowing a fluorescently labelled target analyte through the course, and identifying microbeads which are luminescent.

The central issue which we address is the influence of the retaining structure of the trap on the accessibility of the surface probes on the microbead surface to the target analyte streaming over the microbeads. The dynamic response of the microbead array - i.e. the time required to develop a recognizable signal (or equivalently the number of fluid cell volumes for this signal) is dependent on the ability of the target to diffuse rapidly enough across streamlines to the probe surface. Once at the surface, the target is required to kinetically conjugate to the probes and this rate, as an in-series process, also contributes to the overall binding rate of the target to the probe. We undertook numerical simulations of the mass transfer, using a Langmuir model to describe the surface conjugation step, and computed the surface concentration of the target on the microbead surface as a function of time. This overall binding rate, in nondimensional form, was characterized by two groups, a Peclet number ( $Pe$ ) describing the rate of target solute convection across the microbead (which is proportional to the analyte flow rate) to the rate of diffusion to the particle surface, and a Damkohler number ( $Da$ ) describing the rate of target-probe surface conjugation to the rate of bulk diffusion to the surface. We find that the effect of the trap on the transport rate can be described through, and is critically dependent on, the Peclet number. For fixed  $Da$  and order one values of  $Pe$  (corresponding to weak convection), as shown in Fig. 5.5, large diffusion zones, where the concentration is below the inlet concentration, develop around the microbead and envelop the trap. In this case, because of the presence of the trap, the weak convection cannot bring sufficient amounts of fresh analyte to the probe surface at a rate comparable to the rate of diffusion to the surface. As a result the overall rate of target-probe binding is slow, and, as shown in Fig. 5.9 is much slower than the rate at which target binds to the surface in the idealized case of an unobstructed microbead at the floor of the microchannel. Solutions for the fluid flow also demonstrate the attenuation of the flow around the microbead - especially in the space between the sidewalls of the trap and the microbead - relative to the idealized unobstructed microbead. For the same value of  $Da$ , and  $Pe$  of order  $10^3$ , we find the very interesting result that the larger convection at higher

$Pe$  leads to the development of diffusion zones which take the form of thin boundary layers which encircle the beads within the trap (Fig. 5.6). Because the boundary layers are thin, the diffusion fluxes are large and the overall binding rate increases relative to  $Pe$  of order one. In fact, the binding rate approaches the rate for the idealized case of an unobstructed microbead positioned at the bottom of the channel. Thus if flow rates are large enough, the presence of the trap retaining structure necessary to hold the microbeads in place does not necessarily have to hinder the target transport to the surface. In the trap geometry used here, the aperture at the back end of the trap (and the gap between the microbead and the channel top) allows flow over the microbeads (see the flow simulation, Fig. 5.3 and Fig. 5.4) and it is this flow, when  $Pe$  is large enough, that allows the development of the thin boundary layers which sit inside the trap and around the microbeads and enhance the diffusion rate of the target to the surface. In other studies, wells at the floor of the microchannel are used to sequester and array microbeads to construct the probe library. In this geometry, target only streams over the top part of the microbead, and at high  $Pe$  thin boundary layers cannot encircle a large portion of the microbead. As a result diffusive transport is hindered, and one solution which is proposed is to create drains in the wells to enhance convection around the microbead. The trapping geometry studied here uses an aperture at the back end to accomplish the same goal (as well as providing a gap between the microbead and the top surface of the channel), and is much easier to implement. Another method for constructing a microbead array/ probe library in a microfluidic cell is to place the functionalized microbeads in shallow wells arrayed at the bottom of the channel, and then place the channel top on the microbead array. The height of the channel is the same size as the microbead diameter, so that the channel top holds the microbeads in place. The binding rate in this geometry approaches the idealized case of an unobstructed microbead in the channel for all  $Pe$ , but the microbead array assembly is undertaken ex-situ, which is more demanding than the in-situ hydrodynamic entrapment of the trap array studied here.

The surface kinetic parameter  $Da$  is determined by the nature of the target and the probe, and the probe surface density, and is independent of the trapping geometry. We find that as  $Da$  decreases for a fixed  $Pe$ , the reduced kinetic conjugation rate relative to diffusion results in more uniform surface concentrations around the microbead as the diffusion zones disappear. We identified for each  $Pe$  values of  $Da$  for which the surface kinetics controls the overall binding rate, and the surface concentration can be described by a simple exponential solution which represents the integration of the Langmuir kinetic equation for a constant sublayer concentration (eq. 5.7). The larger  $Pe$ , the larger is the critical value of  $Da$  to achieve this kinetic limit, as the larger  $Pe$  have reduced diffusion limitations. We find in particular for the trapping geometry, that for  $Pe$  of order  $10^3$ , values of  $Da$  less than or equal



to one insures the kinetic limit.

## Chapter 6

# Electrocoalescence of Water-in-Crude Oil Emulsions in Two Dimensions

Direct observation of electrocoalescence of water droplets in crude oil emulsions is demonstrated. Two dimensional configurations of monodisperse water droplets are subjected to a uniform, external electric field and coalescence of individual droplet pairs is observed. By calculating the electrostatic force between droplet pairs using finite element simulations, the identity of coalescing pairs can be accurately predicted.

### 6.1 Introduction and Background

Emulsion stability is relevant to a wide range of applications, including foods, cosmetics, petroleum and other industrial processes. The fundamental issue in the understanding of emulsion stability is the interaction between droplets (or bubbles) of the dispersed phase, specifically the time required for them to approach and coalesce. This can be understood in terms of the time required to drain the continuous fluid phase from between adjacent droplets. To predict this time, knowledge of the forces between the droplets is required to make the coalescence time a well-defined hydrodynamics problem. Validation of such a prediction is most accurately realized by direct observation of individual droplet pair interactions, but this can be difficult to achieve from experiments performed on bulk emulsions.

Microfluidics offers the ability to generate emulsions of monodisperse droplets and observe interactions between droplets on a pairwise basis<sup>102,216–218</sup>. Droplet separation distances can be precisely measured, enabling calculation of droplet interaction forces on a pairwise basis. The origin of these interaction forces depends on the emulsion system being studied and its application. In some instances, emulsion stability is desired, while other applications are predicated on efficient separation of the emulsified phases. In these applications, an external

field is often applied to facilitate droplet coalescence and separation.

A primary example of this field-assisted separation is the use of dielectrophoretic forces to electrocoalesce conducting water droplets in a insulating continuous oil phase<sup>219,220</sup>. The importance of electrocoalescence is primarily due to its utilization in the oil industry, where it is used to separate water from crude oil in a process colloquially known as 'desalting'. Water droplets intentionally introduced into the crude oil to extract salt are subsequently removed via application of an electric field, which polarizes the conducting droplets, producing attractive (and repulsive) forces between droplets that result in coalescence of droplet pairs<sup>221–230</sup>. Successive coalescence events between droplets produce progressively larger droplets that settle under gravity into a bulk water phase that can be easily removed. The simplest model of electrocoalescence assumes that the water droplets behave as infinitely conducting spheres in a perfectly insulating oil, and that the interfacial rheology of the water-crude oil interface plays no role in droplet coalescence. In practice, many crude oils have significant conductivity, reducing droplet polarization when the electric field is applied at 0 Hz. More importantly, crude oils contain numerous polar compounds known as asphaltenes, which adsorb at the oil-water interface and act to stabilize the droplets, inhibiting coalescence. Due the unique nature of the asphaltene constituents in a specific crude oil, the effect of these surface-active compounds cannot be ascertained independently. A valid experimental investigation should therefore be conducted using the crude oil under study to accurately predict electrocoalescence.

Numerous studies of various aspects of electrocoalescence have been published. Several examine the physics of the coalescence event itself. Others examine the behavior of droplet pairs initially separated by some distance. Bibette et al.<sup>231</sup> measured the effect of field strength and droplet separation distance on the coalescence of microfluidically generated surfactant-stabilized water droplet pairs in hexadecane, mapping out a phase diagram which includes three regimes: coalescing, non-coalescing and partial coalescing. Chiesa et al.<sup>226–228</sup> modeled the trajectory of a small droplet coalescing into a larger one as a force balance between the attractive electrostatic and resistive hydrodynamic forces, showing good agreement between experiment and theory. However, no current study examines electrocoalescence in two dimensions, with interactions between multiple droplets taken into account. Furthermore, all of the existing studies are performed in model systems, which are of limited applicability to water in crude oil emulsions where the heterogeneous nature of the crude oil may have a dramatic impact on electrocoalescence.

This study reports results of electrocoalescence experiments performed on two dimensional configurations of monodisperse water droplets in a crude oil. The objective was to first use microfluidics to visualize the electrocoalescence process, and secondly to accurately

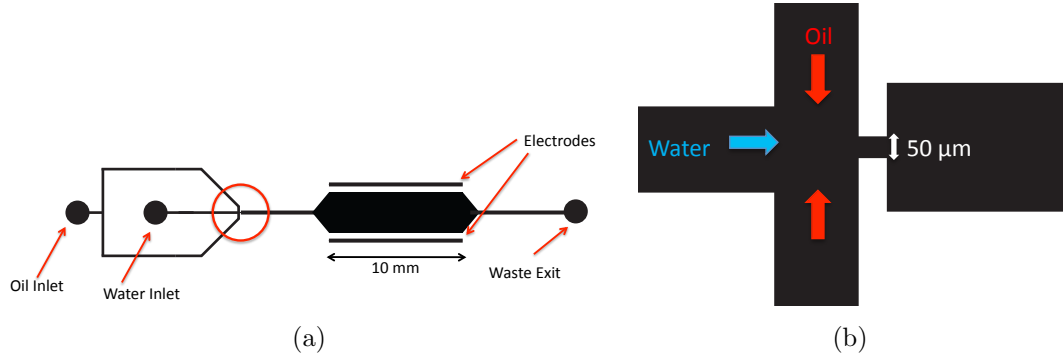


Figure 6.1: Schematic of the microfluidic cell used in the experiments (a) Arrangement of the flow focusing orifice and the chamber to collect the droplets and apply the electric field. (b) Detail of the flow focusing.

predict electrocoalescence between droplet pairs based on a calculation of the pairwise electrostatic force as determined by finite element simulations.

## 6.2 Experimental

To enable direct observation of water droplets in crude water-in-oil emulsions, experiments were performed in a microfluidic cell composed of transparent PDMS. The emulsion was formed by using flow focusing<sup>105,232,233</sup> to create a monodisperse train of water droplets in crude oil, which were then directed through a feeding channel to a holding chamber in which they arrange themselves in an arbitrary configuration, and in which the electric field is applied (Fig. 6.1). Droplets flow out of the chamber through an exit port. The height of the channels in the cell is  $100\ \mu\text{m}$ , and the droplets produced from the  $50\ \mu\text{m}$  orifice are approximately  $80\ \mu\text{m}$ , so the droplets move through the feeding channel and the chamber as a single layer. The microchannels were fabricated using standard soft lithography techniques to produce two layers of PDMS, one containing the fluidic channel and a second, flat layer to seal the channel. The two layers were bonded together following exposure to an oxygen plasma and mounted on a standard glass microscope slide. Access ports cored into the top layer using a biopsy punch allowed introduction fluids of interest via polyethylene tubing connected to syringe pumps. To generate a uniform electric field  $\mathcal{E}$  across the droplets, planar electrodes of aluminum were inserted into the PDMS perpendicular to the lateral plane of the cell, and sited externally from the fluid. The electrodes were connected to an amplifier controlled by a frequency generator. The electric field is applied across the channel and the droplet coalescence events are recorded using a high-speed camera. To prevent the electrical conductivity of the crude oil from reducing the electric field over time, the electric field is applied at a frequency of 500 Hz. The resulting coalescence process in the chamber

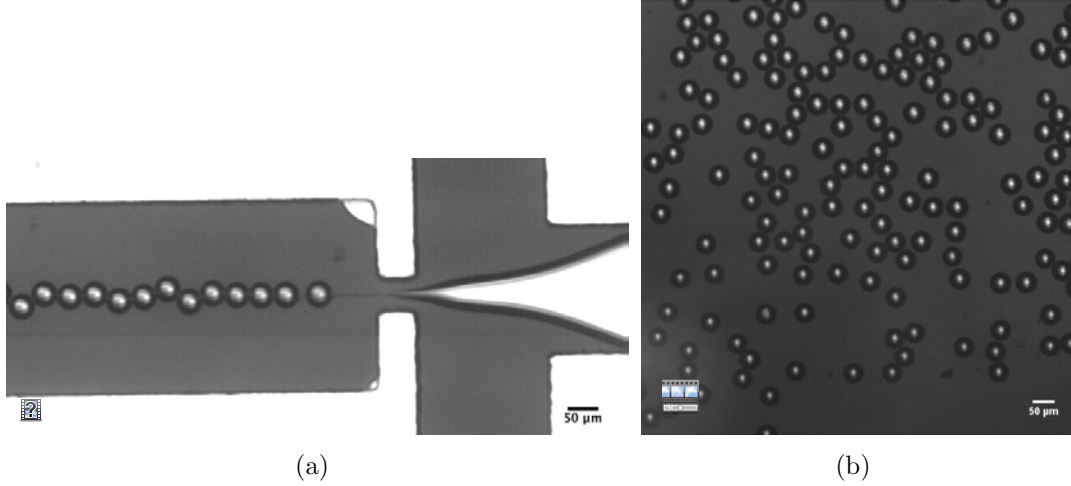


Figure 6.2: (a) Flow focusing production of water droplets in oil and (b) assemblage of droplets in the chamber.

is visualized by optical microscopy using an inverted microscope in brightfield mode and a high speed camera.

Optical micrographs of the flow focusing production of the water droplets in oil at the flow focusing orifice, and a snapshot from a fast video recording of the droplet collection in the chamber are given in Fig. 6.2. The experiments were undertaken in a continuous flow through mode in which the droplet train flows continually into the chamber, and the droplets exit through the port on the opposite side of the chamber. Because the width of the chamber is much larger than the width of the microchannel which feeds the droplets into the chamber, the flow in the chamber is relatively slow, and the droplets only slowly change their configuration with respect to one another.

### 6.3 Theoretical

To predict electrocoalescence between the water droplets in the two-dimensional configuration upon application of the electric field, the electrostatic forces between the droplet pairs must be calculated. We denote by  $\mathcal{E}$  the magnitude of the uniform electric field applied to the droplets in the chamber, by  $a$  the droplet radius, by  $\epsilon_{Oil}$  and  $\epsilon_{Water}$  the dielectric constants of the oil and water phases, respectively, by  $\sigma_{Oil}$  and  $\sigma_{Water}$  the conductivities of the oil and water phases, respectively, and by  $\gamma$  the interfacial tension of the droplets. The magnitude of the applied electric field is less than that required to distort the shapes of the droplets (the electric Bond number,  $Bo = \epsilon_{Oil}\mathcal{E}^2a/\gamma$ , is less than one), therefore the droplets are modeled as monodisperse spheres with known diameter and position. The period of the

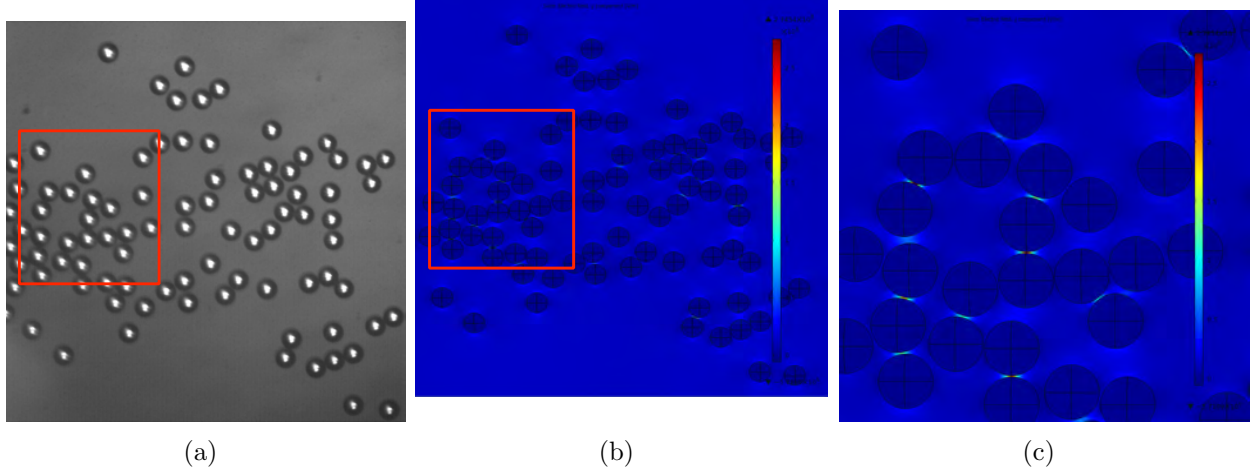


Figure 6.3: (a) Two dimensional configuration of water droplets in crude oil, (b) the associated simulation cell and overlay of color map of the magnitude of the electric field and (c) Detail of the electric field in the boxed area of (a) and (b).

applied field is much greater than the polarization time of the droplets,  $\tau = \epsilon_{Water}/\sigma_{Water}$ . This produces an electric field distribution around the droplets that is quasi-static and can be calculated from the solution to the Laplace equation for the electric potential  $V_{Oil}$  within the oil phase, and within each of the droplets  $i$  in the assembly  $V_{Water}^i$  :

$$\nabla^2 V_{Oil} = 0 \quad (6.1)$$

$$\nabla^2 V_{Water}^i = 0, \quad i = 1, 2, \dots, N \quad (6.2)$$

where  $N$  is the number of droplets. The boundary conditions on the surface of the droplets are continuity of the electric potential and the balance of the electrical conductive flux (no charge accumulation at the surface at steady state),

$$V_{Oil}^i = V_{Water}^i, \quad i = 1, 2, \dots, N \quad (6.3)$$

$$\mathbf{n}^i \cdot \{ \sigma_{Oil}^i \nabla V_{Oil} - \sigma_{Water} \nabla V_{Water}^i \} = 0 \quad i = 1, 2, \dots, N \quad (6.4)$$

where  $\mathbf{n}^i$  is the unit normal to droplet  $i$ .

Although the external field is uniform, the field around the droplets is non-uniform due to their polarization, with larger field strengths at the two poles aligned with the external field and lower field strengths at the two poles aligned perpendicular to the external field. In the case of a single droplet, the magnitudes of the field strengths at these poles will be equal, resulting in no net force on the droplet and therefore no motion. However, droplets

in proximity to one another will experience non-symmetric local fields and will consequently experience net attractive or repulsive forces depending on their orientation relative to the external field. In the simple case of a single droplet pair, this net force has been theoretically calculated using bispherical coordinates. In the case of a configuration of multiple droplets as studied here, finite element simulations are used to solve the above set of equations using the COMSOL Multiphysics 4.2 simulation package for an instantaneous configuration of the droplets. To illustrate in Fig. 6.3(a) is shown a configuration of droplets in the assembly as captured from the high speed recording. This image is used to construct a simulation domain of the droplets in the chamber in which spheres are constructed at the locations of the droplets as dictated by the image to form a two dimensional assembly. (Fig. 6.3(b)). The simulation domain is closed by top and bottom walls, separated a distance  $h$  apart, corresponding to the height of 100  $\mu\text{m}$  of the microfluidic chamber. These walls are modeled as conductors with surface charge to apply the electric field. The three dimensional simulation domain is then closed by side walls in which the potential is assumed to be linear, corresponding to the applied field  $\mathcal{E}$  applied across the electrodes.

Superimposed on the simulation domain of Figure 6.3(b) is a color map of the magnitude of the electric field within each droplet and in the continuous oil phase. The large electric field strengths between the droplets in the chamber which align along the field direction are evident, and indicative of the strong dipolar attractive force which causes the particles to coalesce. Note that the field between the droplets which are aligned perpendicular to the field do not develop the high electric field strengths and therefore do not coalesce.

This electric field computed by the COMSOL simulation is used to calculate the net force on each droplet. In this quasistatic formulation, the force on the droplet  $i$  is composed of the electrical Maxwell stress tensor force on the droplets, and the pressure.

$$\mathbf{F}_{Droplet}^i = \oint \mathbf{n}^i \cdot \mathbf{T}_{Oil}^i dA - \oint p_{Oil}^i \cdot \mathbf{n} dA \quad (6.5)$$

where  $\mathbf{n}^i$  is the surface normal and  $\mathbf{T}_{Oil}^i$  is the Maxwell stress tensor and  $p_{Oil}^i$  is the pressure exerted on droplet  $i$  by the oil phase. The general expression for the Maxwell stress tensor in the oil phase, where  $\mathbf{E}_{Oil}$  is the electric field vector in the oil phase is given by:

$$\mathbf{T}_{Oil} = \epsilon_{Oil} \mathbf{E}_{Oil} \mathbf{E}_{Oil} - \frac{\epsilon_0}{2} |\mathbf{E}_{Oil}|^2 \boldsymbol{\delta} \quad (6.6)$$

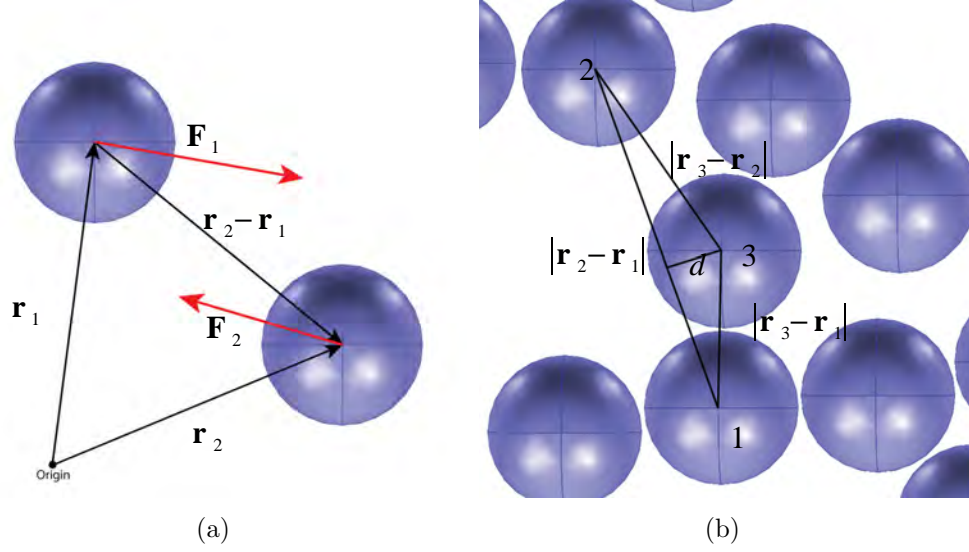


Figure 6.4: (a) Forces exerted on two droplets (in red), and the position vectors of the droplets and (b) details of computing the algorithm for identifying nearest neighbors for coalescence.

where  $\delta$  is the identity matrix. Applying the Maxwell equations  $\nabla \cdot \epsilon \mathbf{E}_{Oil} = 0$  and  $\nabla \times \mathbf{E}_{Oil} = 0$  and a vector identity simplifies the divergence of  $\mathbf{T}_{Oil}$ , which is equal to the pressure gradient:

$$\nabla \cdot \mathbf{T}_{Oil} = \frac{\epsilon_{Oil} - \epsilon_0}{2} \nabla |\mathbf{E}_{Oil}|^2 = \nabla p_{Oil} \quad (6.7)$$

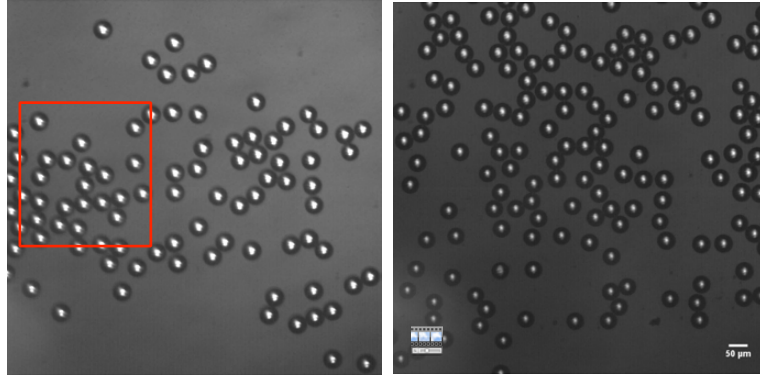
At the surface of the droplet,  $\mathbf{E}_{Oil}$  has no tangential component, therefore  $|\mathbf{E}_{Oil}|^2 = E_{n,oil}^2$  and the net force on the droplet can be calculated:

$$\mathbf{F}_{Droplet}^i = \oint \frac{\epsilon_{Oil}}{2} E_{n,oil}^2 dA \quad (6.8)$$

From the finite element simulations of the electric field, the force on each of the droplets is computed from eq. 6.8.

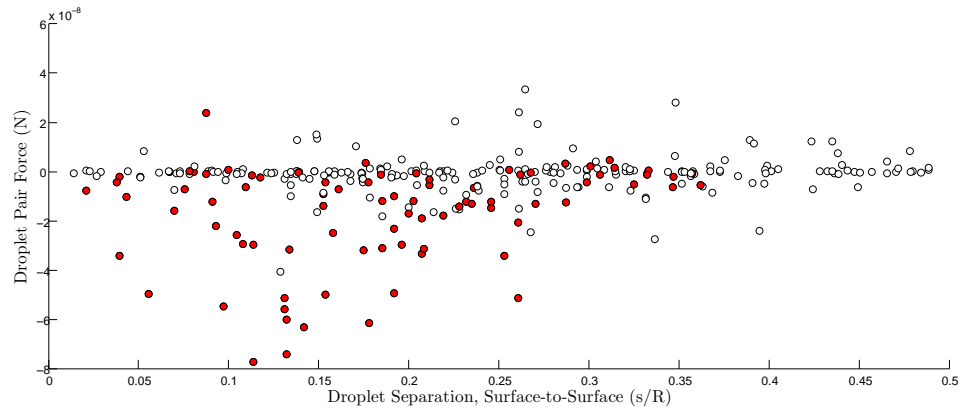
This net force is expected to predict the droplet motion upon application of the electric field. However, the close proximity of the droplets prior to the application of the field means that no significant motion between droplets is possible prior to coalescence. Therefore, the net force on each droplet must be deconstructed to identify the component of the force due to each adjacent droplet. In other words, the forces on the droplet must be calculated on a pairwise basis to identify which droplet pairs experience net attractive forces and are therefore likely to coalesce. This is done by simple vector projection using the net force of





(a)

(b)



(c)

Figure 6.5: (a) and (b) Two configurations of the droplets in the chamber and (c) plot of pairwise electrostatic force between droplet pairs versus their separation distance  $s$  normalized by the droplet radius  $a$  for these two configurations.

each droplet and the center to center vector between each droplet pair (Fig. 6.4(a)):

$$F_{pair} = \frac{[\mathbf{F}_2 - \mathbf{F}_1] \cdot [\mathbf{r}_2 - \mathbf{r}_1]}{|\mathbf{r}_2 - \mathbf{r}_1|} \quad (6.9)$$

With this definition, negative values of the pairwise force correspond to net attraction between the droplets (along their line of centers), and positive values to net repulsion. Because each droplet only has a certain number of nearest neighbors which block its potential coalescence with other droplets, an algorithm is employed to identify which droplet pairs are not obstructed by third droplets and are therefore potentially able to coalescence (Fig. 6.4(b)). Thus for example droplet 2 is an accessible neighbor of droplet 1 if the distance  $d$  from droplet 3 center to the line of centers from droplet 1 to droplet 2 is greater than the radius of droplet 3. Using these calculations, the resulting pairwise droplet forces are plotted as a function of the separation distance,  $s$  (edge to edge) between the droplets in the pair (normalized by the droplet radius  $a$ ) for two (instantaneous) configurations as given by Fig. 6.5(c) for two configurations as given by Fig. 6.5(a) and 6.5(b). The electric field is computed first in the oil phase from these configurations, and then eq. 6.8 is used to calculate the force.

To evaluate Fig. 6.5(c) for its ability to predict which droplets will coalesce from the mapping of the pairwise droplet-droplet forces for the configuration, we note that the coalescence of individual droplet pairs proceeds upon application of the external electric field. Due to the fact that the droplet configuration changes subsequent to the configuration depicted, only droplets pairs coalescing within the first 0.1 seconds, which are therefore assumed to be coalescing due to the forces calculated from this droplet configuration, are considered. These coalescing pairs are identified on the plot of pairwise droplet forces versus separation distance in red. As expected, droplet pairs with large negative (attractive) forces between them coalesce, while droplet pairs with positive (repulsive) forces between them do not coalesce. At larger separation distances, droplet pairs do not experience large forces and therefore do not coalesce due to the initial droplet configuration. As shown in 6.5(c), several droplet pairs with negative forces do not coalesce. This can be explained by the fact that one droplet in the pair is also half of a pair with a larger negative force, and therefore coalesces with the droplet with which it has the larger attractive force, as expected.

In conclusion, we have demonstrated accurate prediction of pairwise electrocoalescence of water droplets emulsified in a crude oil. The unique ability of microfluidic geometries to generate monodisperse emulsion droplets and observe them in a macroscopically opaque continuous phase such as crude oil should encourage further work using microfluidics to study

emulsion stability.

# Bibliography

- [1] J Bico, C Marzolin, and D. Quere, “Pearl drops”, *Europhysics Letters* **47**(6), pp. 743–744 (1999).
- [2] D Quere, “Fakir droplets”, *Nature Materials* **1**, pp. 14–15 (2002).
- [3] N. A. Patankar, “On the modeling of hydrophobic contact angles on rough surfaces”, *Langmuir* **19**(4), pp. 1249–1253 (2003).
- [4] Bo He, Neelesh A. Patankar, and Junghoon Lee, “Multiple Equilibrium Droplet Shapes and Design Criterion for Rough Hydrophobic Surfaces”, *Langmuir* **19**(12), pp. 4999–5003 (2003).
- [5] Alexander Otten and Stephan Herminghaus, “How plants keep dry: a physicist’s point of view.”, *Langmuir* **20**(6), pp. 2405–8 (2004).
- [6] N. A. Patankar, “Mimicking the lotus effect: Influence of double roughness structures and slender pillars”, *Langmuir* **20**, pp. 8209 (2004).
- [7] N. A. Patankar, “Transition between superhydrophobic states on rough surfaces.”, *Langmuir* **20**(17), pp. 7097–7102 (2004).
- [8] G. McHale, N. J. Shirtcliffe, and M. I. Newton, “Contact angle hysteresis on superhydrophobic surfaces”, *Langmuir* **20**, pp. 10146 (2004).
- [9] D Quere, “Wetting and roughness”, *Annu. Rev. Mater. Res.* **38**, pp. 71–99 (2008).
- [10] Quere D., “Non-sticking drops”, *Rep. Prog. Phys.* **68**, pp. 2495–2532 (2005).
- [11] P. Roach, J. Shirtcliffe, and M. Newton, “Progress in superhydrophobic surface development”, *Soft Matter* **4**, pp. 224–240 (2008).
- [12] C. Xue, S. Jia, J. Zhang, and J. Ma, “Large-area fabrication of superhydrophobic surfaces for practical applications: an overview”, *Sci. Technol. Adv. Mater.* **11**, pp. 033002 (2010).

- [13] M. Liu, Y. Zheng, J. Zhai, and L. Jiang, “Bioinspired super-antiwetting interfaces with special liquid-solid adhesion”, *Accounts of Chemical Research* **43**, pp. 368–377 (2010).
- [14] A. Nakagima, “Design of hydrophobic surfaces for liquid droplet control”, *NPG Asia Mater.* **3**, pp. 49–56 (2011).
- [15] K. Liu and L. Jiang, “Bio-inspired self-cleaning surfaces”, *Annual Review of Materials Research* **42**, pp. 231–263 (2012).
- [16] B. Bhushan, “Bioinspired structured surfaces”, *Langmuir* **28**, pp. 1698–1714 (2012).
- [17] S. Nishimoto and B. Bhushan, “Bioinspired self-cleaning surfaces with superhydrophobicity, superoleophilicity, and superhydrophilicity”, *RSC Adv.* **3**, pp. 671–690 (2013).
- [18] H. Butt, I. Roisman, M. Brinkmann, P. Papadopoulos, D. Vollmer, and C. Semperebon, “Characterization of super-repellent surfaces”, *Current Opinion in Colloid and Interface Science* **19**, pp. 343–354 (2014).
- [19] H. Butt, D. Vollmer, and P. Papadopoulos, “Super-repellent layers: the smaller the better”, *Advances in Colloid and Interface Science* **218**, pp. 48–68 (2015).
- [20] R. E. Johnson and R. H. Dettre, *Contact Angle, Wettability and Adhesion: Advances in Chemistry Series*, (1964).
- [21] P. G. De Gennes, “Wetting: Statics and dynamics”, *Rev. Mod. Phys.* **57**, pp. 827 (1985).
- [22] David Quere, “Wetting and roughness”, *Annual Review of Materials Research* **38**(1), pp. 71–99 (2008).
- [23] a Dupuis and J M Yeomans, “Modeling droplets on superhydrophobic surfaces: equilibrium states and transitions.”, *Langmuir* **21**(6), pp. 2624–9 (2005).
- [24] A. Dupuis and J M Yeomans, “Dynamics of sliding drops on superhydrophobic surfaces”, *Europhysics Letters* **75**, pp. 105–111 (2006).
- [25] H Kusumaatmaja and J M Yeomans, “Modeling contact angle hysteresis on chemically patterned and superhydrophobic surfaces.”, *Langmuir* **23**(11), pp. 6019–32 (2007).
- [26] H. Kusumaatmaja, M. L. Blow, A. Dupuis, and J. M. Yeomans, “The collapse transition on superhydrophobic surfaces”, *Europhysics Letters* **81**(3), pp. 36003 (2008).

- [27] Halim Kusumaatmaja and J. Yeomans, “Lattice boltzmann simulations of wetting and drop dynamics”, *Simulating Complex Systems by Cellular Automata* **10**, pp. 241–274 (2010).
- [28] B. Mognetti and J. Yeomans, “Modeling receding contact lines on superhydrophobic surfaces”, *Langmuir* **26**, pp. 18162–18168 (2010).
- [29] W. Barthlott and C. Neinhuis, “Purity of sacred lotus, or escape from contamination in biological surfaces”, *Planta* **202**(1), pp. 1–8 (1997).
- [30] H. Ernikat, P. Ditsche-Kuru, C. Neinhuis, and W. Barthlott, “Superhydrophobicity in perfection: The outstanding properties of the lotus leaf”, *Beilstein Journal of Nanotechnology* **2**, pp. 152–161 (2011).
- [31] F. Shi, J. Niu, J. Liu, F. Liu, Z. Wang, X. Feng, and X. Zhang, “Towards understanding why a superhydrophobic coating is needed by water striders”, *Adv. Mater.* **19**, pp. 2257–2261 (2007).
- [32] M. Ma and R. M. Hill, “Superhydrophobic surfaces”, *Current Opinion in Colloid & Interface Science* **11**(4), pp. 193–202 (2006).
- [33] Chang-Hwan Choi and Chang-Jin Kim, “Large slip of aqueous liquid flow over a nanoengineered superhydrophobic surface”, *Physical Review Letters* **96**(6), pp. 1–4 (2006).
- [34] J. P. Rothstein, “Slip on superhydrophobic surfaces”, *Annual Review of Fluid Mechanics* **42**(1), pp. 89–109 (2010).
- [35] Richard Truesdell, Andrea Mammoli, Peter Vorobieff, Frank van Swol, and C. Brinker, “Drag Reduction on a Patterned Superhydrophobic Surface”, *Physical Review Letters* **97**(4), pp. 1–4 (2006).
- [36] X. Zhang, F. Shi, J. Niu, Y. Jiang, and Z. Wang, “Superhydrophobic surfaces: from structural control to functional application”, *J. Mater. Chem.* **18**, pp. 621–633 (2008).
- [37] J. Genzer and K. Efimenko, “Recent developments in superhydrophobic surfaces and their relevance to marine fouling: a review”, *Biofouling* **22**(5), pp. 339–360 (2006).
- [38] A. B. D. Cassie and S. Baxter, “Wettability of porous surfaces”, *Trans. Faraday Soc.* **40**, pp. 546–551 (1944).

- [39] R. N. Wenzel, “Resistance of solid surfaces to wetting by water”, *Ind. Eng. Chem.* **28**(8), pp. 988–994 (1936).
- [40] L. Gao and T. J. McCarthy, “How Wenzel and Cassie were wrong.”, *Langmuir* **23**(7), pp. 3762–5 (2007).
- [41] M.V. Panchagnula and S. Vedantam, “Comment on how Wenzel and Cassie were wrong by Gao and McCarthy”, *Langmuir* **23**(26), pp. 13242 (2007).
- [42] L. Gao and T. J. McCarthy, “Reply to” Comment on How Wenzel and Cassie Were Wrong by Gao and McCarthy”, *Langmuir* **23**(26), pp. 13243 (2007).
- [43] A. Marmur, “Wetting on hydrophobic rough surfaces: to be heterogeneous or not to be?”, *Langmuir* **19**(20), pp. 8343–8348 (2003).
- [44] G. Fang, W. Li, X. Wang, and G. Qiao, “Droplet motion on designed microtextured superhydrophobic surfaces with tunable wettability.”, *Langmuir* **24**(20), pp. 11651–60 (2008).
- [45] W. Li and A. Amirfazli, “Microtextured superhydrophobic surfaces: a thermodynamic analysis”, *Advances in colloid and interface science* **132**(2), pp. 51–68 (2007).
- [46] M. Nosonovsky and B. Bhushan, “Patterned nonadhesive surfaces: superhydrophobicity and wetting regime transitions.”, *Langmuir* **24**(4), pp. 1525–33 (2008).
- [47] C. Ishino, K. Okumura, and D. Quéré, “Wetting transitions on rough surfaces”, *Europhysics Letters* **68**(3), pp. 419–425 (2004).
- [48] A. Dupuis and J. M. Yeomans, “Modeling droplets on superhydrophobic surfaces: Equilibrium states and transitions”, *Langmuir* **21**(2624-2629) (2005).
- [49] H. Kusumaatmaja and J. M. Yeomans, “Modeling contact angle hysteresis on chemically patterned and superhydrophobic surfaces”, *Langmuir* **23**, pp. 6019–6032 (2007).
- [50] N. Moradi, F. Varnik, and I. Steinbach, “Roughness-gradient-induced spontaneous motion of droplets on hydrophobic surfaces: A lattice Boltzmann study”, *Europhysics Letters* **89**(2), pp. 26006 (2010).
- [51] J. Zhang and D. Y. Kwok, “Contact line and contact angle dynamics in superhydrophobic channels”, *Langmuir* **22**(11), pp. 4998–5004 (2006).
- [52] C. Huh and L. E. Scriven, “Hydrodynamic model of steady movement of a solid/liquid/fluid contact line”, *J. Colloid Interface Sci.* **35**(1), pp. 85–101 (1971).

- [53] M. H. Eres, L. W. Schwartz, and R. V. Roy, “Fingering phenomena for driven coating films”, *Physics of Fluids* **12**(6), pp. 1278 (2000).
- [54] M. A. Spaid and G. M. Homsy, “Stability of Newtonian and viscoelastic dynamic contact lines”, *Physics of Fluids* **8**(2), pp. 460 (1996).
- [55] X. Wang, *On the Rolling Motion of Viscous Fluid on a Rigid Surface*, PhD thesis New Jersey Institute of Technology (2008).
- [56] H. P. Greenspan, “On the motion of a small viscous droplet that wets a surface”, *Journal of Fluid Mechanics* **84**(01), pp. 125–143 (1978).
- [57] A. Mazouchi, C. M. Gramlich, and G. M. Homsy, “Time-dependent free surface stokes flow with a moving contact line. i. flow over plane surfaces”, *Phys. Fluids* **16**(5), pp. 1647–1659 (2004).
- [58] T.-S. Jiang, S.-G. Oh, and J.C. Slattery, “Correlation for dynamic contact angle”, *Journal of Colloid and Interface Science* **69**, pp. 74 (1979).
- [59] A. A. Becker, *The Boundary Element Method in Engineering: a complete course*, McGraw-Hill (1992).
- [60] C. Pozrikidis, *Boundary integral and singularity methods for linearized viscous flow*, Cambridge University Press (1992).
- [61] “<http://www.microchem.com/products/pdf/su-82000datasheet2025thru2075ver4.pdf>”.
- [62] A. Scheludko, “Thin films”, *Advances in Colloid and Interface Science* **1**(391-464) (1967).
- [63] I. B. Ivanov, editor, *Thin Liquid Films*, Marcel Dekker (1988).
- [64] B. V. Derjaguin, *Theory of Stability of Colloids and Thin Films*, Plenum Press: Consultants Bureau, New York (1989).
- [65] S. Sjoblom, editor, *Encyclopedic Handbook of Emulsion Technology*, Marcel Dekker, New York (2001).
- [66] Charles N. Baroud, Francois Gallaire, and Remi Dangla, “Dynamics of microfluidic droplets”, *Lab on a Chip* **10**(16), pp. 2032–2045 (2010).
- [67] J. Israelachvili, *Intermolecular and Surface Forces*, Academic Press: New York 3rd edition (2011).



- [68] P.G. DeGennes, “Wetting: Statics and dynamics”, *Reviews of Modern Physics* **57**, pp. 827–863 (1985).
- [69] L. Leger and J. F. Joanny, “Liquid spreading”, *Reports on Progress in Physics* **55**, pp. 431–486 (1992).
- [70] D. Bonn, J. Eggers, J. Indekeu, J. Meunier, and E. Rolley, “Wetting and spreading”, *Reviews of Modern Physics* **81**, pp. 739–805 (2009).
- [71] M Mahe, M Vignes-Adler, and P.M Adler, “Adhesion of droplets on a solid wall and detachment by a shear flow: Iii. contaminated systems”, *Journal of Colloid and Interface Science* **126**(1), pp. 337 – 345 (1988).
- [72] M Mahe, M Vignes-Adler, and P.M Adler, “Adhesion of droplets on a solid wall and detachment by a shear flow: Ii. rough substrates”, *Journal of Colloid and Interface Science* **126**(1), pp. 329 – 336 (1988).
- [73] M Mahe, M Vignes-Adler, A Rousseau, C.G Jacquin, and P.M Adler, “Adhesion of droplets on a solid wall and detachment by a shear flow: I. pure systems”, *Journal of Colloid and Interface Science* **126**(1), pp. 314 – 328 (1988).
- [74] E. Lauga, M. Brenner, and H. Stone, “Microfluidics: The no-slip boundary condition”, In C. Tropea, A. Yarin, and J. Foss, editors, *Springer Handbook of Experimental Fluid Mechanics* chapter 19, , pp. 1219–1240. Springer (2007).
- [75] L. Bocquet and J. Barrat, “Flow boundary conditions from nano to micro scales”, *Soft Matter* **3**, pp. 685–693 (2007).
- [76] Chiara Neto, Drew R Evans, Elmar Bonaccorso, Hans-Jürgen Butt, and Vincent S J Craig, “Boundary slip in Newtonian liquids: a review of experimental studies”, *Reports on Progress in Physics* **68**(12), pp. 2859–2897 (2005).
- [77] T. Wong, S. Kang, S. Tang, Smythe E., B. Hatton, A. Grinthal, and J. Aizenberg, “Bioinspired self repairing slippery surfaces with pressure-stable omniphobicity”, *Nature* **477**(443-447) (2011).
- [78] J. Smith, R. Dhiman, S. Anand, E. Reza-Garduno, R. Cohen, G. McKinley, and K. Varanasi, “Droplet mobility on lubricated impregnated surfaces”, *Soft Matter* **9**, pp. 1772–1780 (2013).
- [79] E. Lauga, M. Brenner, and H. Stone, *Microfluidics: The No-slip Boundary Condition* chapter 19, , pp. 1219–1240, Springer (2007).

- [80] Roman S. Voronov, Dimitrios V. Papavassiliou, and Lloyd L. Lee, “Slip length and contact angle over hydrophobic surfaces”, *Chemical Physics Letters* **441**(4–6), pp. 273 – 276 (2007).
- [81] Christian Sendner, Dominik Horinek, Lyderic Bocquet, and Roland R. Netz, “Interfacial water at hydrophobic and hydrophilic surfaces: Slip, viscosity, and diffusion”, *Langmuir* **25**(18), pp. 10768–10781 (2009).
- [82] Chiara Neto, Drew R Evans, Elmar Bonaccorso, Hans-Jürgen Butt, and Vincent S J Craig, “Boundary slip in newtonian liquids: a review of experimental studies”, *Reports on Progress in Physics* **68**(12), pp. 2859–2897 (2005).
- [83] Olga I. Vinogradova and Gleb E. Yakubov, “Dynamic effects on force measurements. 2. lubrication and the atomic force microscope”, *Langmuir* **19**(4), pp. 1227–1234 (2003).
- [84] C. Cottin-Bizonne, B. Cross, A. Steinberger, and E. Charlaix, “Boundary slip on smooth hydrophobic surfaces: Intrinsic effects and possible artifacts”, *Phys. Rev. Lett.* **94**, pp. 056102 (2005).
- [85] P. Huang, J. Guasto, and K. Bruer, “Direct measurement of slip velocities using three dimensional total internal reflection velocimetry”, *Journal of Fluid Mechanics* **566**, pp. 447–464 (2006).
- [86] C. I. Bouzigues, P. Tabeling, and L. Bocquet, “Nanofluidics in the debye layer at hydrophilic and hydrophobic surfaces”, *Phys. Rev. Lett.* **101**, pp. 114503 (2008).
- [87] S.P. McBride and B.M. Law, “Viscosity dependent liquid slip at molecularly smooth hydrophobic surfaces”, *Phys. Rev. E* **80**, pp. 060601 (2009).
- [88] A.P. Bowles, C. Honig, and W. Ducker, “No-slip boundary condition for weak solid-liquid interactions”, *J. Phys. Chem. C* **115**, pp. 8613–8621 (2011).
- [89] Liwen Zhu, Chiara Neto, and Phil Attard, “Reliable measurements of interfacial slip by colloid probe atomic force microscopy. iii. shear-rate-dependent slip”, *Langmuir* **28**(7), pp. 3465–3473 (2012).
- [90] J. P. Rothstein, “Slip on superhydrophobic surfaces”, *Annual Review of Fluid Mechanics* **42**(1), pp. 89–109 (2010).
- [91] J.R.T. Sneddon and D. Lohse, “Nanobubbles and micropancakes: gaseous domains on immersed substrates”, *J. Phys.: Condens. Matter* **23**, pp. 133001 (2011).

- [92] Abdelhamid Maali and Bharat Bhushan, “Nanobubbles and their role in slip and drag”, *Journal of Physics: Condensed Matter* **25**(18), pp. 184003 (2013).
- [93] Derek C. Tretheway and Carl D. Meinhart, “A generating mechanism for apparent fluid slip in hydrophobic microchannels”, *Physics of Fluids* **16**(5), pp. 1509–1515 (2004).
- [94] Yingxi Zhu and Steve Granick, “Rate-dependent slip of newtonian liquid at smooth surfaces”, *Phys. Rev. Lett.* **87**, pp. 096105 (2001).
- [95] Derek C. Tretheway and Carl D. Meinhart, “Apparent fluid slip at hydrophobic microchannel walls”, *Physics of Fluids* **14**(3), pp. L9–L12 (2002).
- [96] J. Ou, B. Perot, and J. Rothstein, “Direct velocity measurements of the flow past drag-reducing ultrahydrophobic surfaces”, *Physics of Fluids A* **17**, pp. 103606 (2005).
- [97] C.-H. Choi and C.-Jin Kim, “Large slip of aqueous liquid flow over a nanoengineered superhydrophobic surface”, *Physical Review Letters* **96**(6), pp. 1–4 (2006).
- [98] P. Joseph, C. Cottin-Bizonne, J. Benpit, C. Ybert, C. Journet, P. Tabeling, and L. Bocquet, “Slippage of water past superhydrophobic carbon nanotube forests in microchannels”, *Physical Review Letters* **97**, pp. 156104 (2006).
- [99] A. Maali, Y. Pan, B. Bhusan, and E. Charlaix, “Hydrodynamic drag-force measurement and slip length on microstructured surfaces”, *Physical Review E* **85**, pp. 066310 (2012).
- [100] C. Cottin-Bizonne, E. Barentin, E. Charlaix, L. Bocquet, and J. Barrat, “Dynamics of simple liquids at heterogeneous surfaces: Molecular dynamics simulations and hydrodynamic description”, *Eur. Biophysics Journal E* **15**, pp. 427–438 (2004).
- [101] E. Lauga and A. Davis, “Hydrodynamic friction on fakir-like superhydrophobic surfaces”, *J. Fluid Mech.* **661**, pp. 402–411 (2010).
- [102] R. Seemann, M. Brinkmann, T. Pfohl, and S. Herminghaus, “Droplet based microfluidics”, *Rep. Prog. Phys.* **75**, pp. 016601 (2012).
- [103] J. Lee, C. Park, and G. M. Whitesides, “Solvent compatibility of poly(dimethylsiloxane)-based microfluidic devices”, *Anal. Chem.* **75**, pp. 6544–6554 (2003).
- [104] R. Dangla, F. Gallaire, and C. Baroud, “Microchannel deformations due to solvent induced pdms swelling”, *Lab on a Chip* **10**, pp. 2972–2978 (2010).

- [105] S. L. Anna, N. Bontoux, and H. A. Stone, “Formation of dispersions using ”flow focusing” in microchannels”, *Applied Physics Letters* **82**(3), pp. 364–366 (2003).
- [106] Eva Santini, Libero Liggieri, Linda Sacca, Daniele Clausse, and Francesca Ravera, “Interfacial rheology of span 80 adsorbed layers at paraffin oil–water interface and correlation with the corresponding emulsion properties”, *Colloids and Surfaces A: Physicochemical and Engineering Aspects* **309**, pp. 270 – 279 (2007).
- [107] R.G. Cox and H. Brenner, “The slow motion of a sphere through viscous fluid towards a plane surface - ii small gap widths including inertial effects”, *Chemical Engineering Science* **22**, pp. 1753–1777 (1967).
- [108] Y. Chang and H. Keh, “Slow motion of a slip spherical particle perpendicular to two plane walls”, *Journal of Fluids and Structures* **23**, pp. 647–661 (2006).
- [109] M. H. Davis, “Two charged spherical conductors in a unifrom electric field: Forces and field strength”, *Quarterly Journal of Mechanics and Applied Mathematics* **17**, pp. 499–511 (1964).
- [110] L. Pasol, M. Martin, M. L. Ekiel-Jezewska, E. Wajnryb, J. Blawdziewicz, and F. Feuillebois, “Motion of a sphere parallel to plane walls in a poiseuille flow. application to field-flow fractionation and hydrodynamic chromatography”, *Chemical Engineering Science* **66**(18), pp. 4078–4089 (2011).
- [111] J. McDonald and G. Whitesides, “Poly(dimethylsiloxane) as a material for fabricating microfluidic devices”, *Accounts of Chemical Research* **35**, pp. 491–499 (2002).
- [112] Krassimir D. Danov, Simeon D. Stoyanov, Nikolay K. Vitanov, and Ivan B. Ivanov, “Role of surfactants on the approaching velocity of two small emulsion drops”, *Journal of Colloid and Interface Science* **368**(1), pp. 342 – 355 (2012).
- [113] J.T. Groves, “Membrane array technology for drug discovery”, *Current Opinion in Drug Discovery and Development* **5**, pp. 606–612 (2002).
- [114] R.A. Kumar and D.S. Clark, “High-throughput screening of biocatalytic activity: Applications in drig discovery”, *Current Opinion in Chemical Biology* **10**, pp. 162–168 (2006).
- [115] Y. Fang, Y. Hong, B. Webb, and J. Lahiri, “Applications of biomembranes in drug discovery”, *MRS Bulletin* **31**, pp. 541–545 (2006).

- [116] D.V. Lim, J. M. Simpson, E. A. Kearns, and M. F. Kramer, “Current and developing technologies for monitoring agents of bioterrorism and biowarfare”, *Clinical Microbiology Reviews* **18**, pp. 583–607 (2005).
- [117] E. Castellana and P.S. Cremer, “Solid supported lipid bilayers: From biophysical studies to sensor design”, *Surface Science Reports* **61**, pp. 429–444 (2006).
- [118] J. Lazcka, Delcampo and F. Munoz, “Pathogen detection: A perspective of traditional methods and biosensors”, *Biosensors and Bioelectronics* **22**, pp. 1205–1217 (2007).
- [119] A. Chemburu, K. Fenton, G. Lopez, and R. Zeineldin, “Biomimetic silica microspheres in biosensing”, *Molecules* **15**, pp. 1932–1957 (2010).
- [120] Gerald Walter, Konrad Bassow, Dolores Cahill, Angelika Lueking, and Hans Lehrach, “Protein arrays for gene expression and molecular interaction screening”, *Current Opinion in Microbiology* (3), pp. 298–302 (2000).
- [121] T. Kodadek, “Protein microarrays: prospects and problems.”, *Chem Biology* **8**(2), pp. 105–115 (2001).
- [122] Heng Zhu and Michael Snyder, “Protein chip technology”, *Current Opinion in Chemical Biology* **7**(1), pp. 55 – 63 (2003).
- [123] M. Schena, *Microarray Analysis*, John Wiley and Sons, Inc. (2003).
- [124] D. Yeo, R. Panicker, L. Tan, and S. Yao, “Strategies for immobilization of biomolecules in a microarray”, *Combinatorial Chemistry and High Throughput Screening* **7**, pp. 213–221 (2004).
- [125] P. Predki, “Functional protein microarrays: Ripe for discovery”, *Current Opinion in Chemical Biology* **8**, pp. 8–13 (2004).
- [126] Joshua LaBaer and Niroshan Ramachandran, “Protein microarrays as tools for functional proteomics”, *Current Opinion in Chemical Biology* **9**(1), pp. 14 – 19 (2005), [jce:title;Proteomics and genomics;ce:title;.](#)
- [127] Claus Hultschig, Jürgen Kreutzberger, Harald Seitz, Zoltán Konthur, Konrad Büsow, and Hans Lehrach, “Recent advances of protein microarrays”, *Current Opinion in Chemical Biology* **10**(1), pp. 4 – 10 (2006), [jce:title;Proteomics and genomics;ce:title;.](#)
- [128] C. LaFratta and D.R. Walt, “Very high density sensing arrays”, *Chemical Reviews* **108**, pp. 614–637 (2008).

- [129] R. Wellhausen and H. Seitz, “Facing current quantification challenges in protein microarrays”, *Journal of Biomedicine and Biotechnology* **2012**, pp. 831347 (2012).
- [130] Wlad Kusnezow, Yana V. Syagailo, Sven Rüffer, Konstantin Klenin, Walter Sebald, Jörg D. Hoheisel, Christoph Gauer, and Igor Goychuk, “Kinetics of antigen binding to antibody microspots: Strong limitation by mass transport to the surface”, *PROTEOMICS* **6**(3), pp. 794–803 (2006).
- [131] Andrea Lionello, Jacques Josserand, Henrik Jensen, and Hubert H. Girault, “Protein adsorption in static microsystems: effect of the surface to volume ratio”, *Lab on a Chip* **5**(3), pp. 254–260 (2005).
- [132] C. Situma, M. Hashimoto, and S. Soper, “Merging microfluidics with microarray-based assays”, *Biomolecular Engineering* **23**, pp. 213–231 (2006).
- [133] T. Squires, R. Messinger, and S. Mannelis, “Making it stick: Convection, reaction and diffusion in surface-based biosensors”, *Nature Biotechnology* **26**, pp. 417–426 (2008).
- [134] Frances S. Ligler, “Perspective on optical biosensors and integrated sensor systems”, *Analytical Chemistry* **81**(2), pp. 519–526 (2009).
- [135] J. Mairhofer, K. Roppert, and P. Ertl, “Microfluidic systems for pathogen detection”, *Sensors* **9**, pp. 4804–4823 (2009).
- [136] W.-C. Tan and E. Finehout, editors, *Microfluidics for Biological Applications*, Springer (2009).
- [137] Alphonsus H. C. Ng, Uvaraj Uddayasankar, and Aaron R. Wheeler, “Immunoassays in microfluidic systems”, *Analytical and Bioanalytical Chemistry* **397**(3), pp. 991–1007 (2010).
- [138] I. Oita, H. Halewyck, B. Thys, B. Rombaut, Y. Heyden, and D. Mangelings, “Microfluidics in macro-biomolecules analysis: macro inside in a nanoworld”, *Anal. Bioanal. Chem.* **398**, pp. 239–264 (2010).
- [139] A. Foudeh, T.F. Didar, T. Veres, and M. Tabrizian, “Microfluidic designs and techniques using lab-on-a-chip devices for pathogen detection for point-of-care diagnostics”, *Lab on a Chip* **12**, pp. 3249–3266 (2012).
- [140] John Connelly and Antje Baeumner, “Biosensors for the detection of waterborne pathogens”, *Analytical and Bioanalytical Chemistry* **402**(1), pp. 117–127 (2012).

- [141] Andreas Janshoff and Stephanie Kunneke, “Micropatterned solid-supported membranes formed by micromolding in capillaries”, *European Biophysics Journal* **29**(7), pp. 549–554 (2000).
- [142] André Bernard, Bruno Michel, and Emmanuel Delamarche, “Micromosaic immunoassays”, *Analytical Chemistry* **73**(1), pp. 8–12 (2001).
- [143] Yali Gao, Guoqing Hu, Frank Y. H. Lin, Philip Sherman, and Dongqing Li, “An electrokinetically-controlled immunoassay for simultaneous detection of multiple microbial antigens”, *Biomedical Microdevices* **7**, pp. 301–312 (2005).
- [144] James A. Benn, Jenny Hu, Bradley J. Hogan, Rebecca C. Fry, Leona D. Samson, and Todd Thorsen, “Comparative modeling and analysis of microfluidic and conventional dna microarrays”, *Analytical Biochemistry* **348**(2), pp. 284 – 293 (2006).
- [145] E. Verpoorte, “Beads and chips: New recipes for analysis”, *Lab on a Chip* **3**, pp. 60N–68N (2003).
- [146] C.T. Lim and Y. Zhang, “Bead-based microfluidic immunoassays: The next generation”, *Biosensors and Bioelectronics* **22**, pp. 1197–1204 (2007).
- [147] S. Derveaux, B. Stubbe, K. Braeckmans, C. Roelant, K. Sato, J. Demeester, and S.C. De Smedt, “Synergism between particle-based multiplexing and microfluidics technologies may bring diagnostics closer to the patient”, *Analytical and Bioanalytical Chemistry* **391**, pp. 2453–2467 (2008).
- [148] D. Mark, S. Haeberle, G. Roth, F. Von Setten, and R. Zengerle, “Microfluidic lab-on-a-chip platforms: requirements, characteristics and applications”, *Chemical Society Reviews* **39**, pp. 1153–1182 (2010).
- [149] Dario Vignali, “Multiplexed particle-based flow cytometric assays”, *Journal of Immunological Methods* **243**(1-2), pp. 243–255 (2000).
- [150] John P. Nolan and Larry A. Sklar, “Suspension array technology: evolution of the flat-array paradigm”, *Trends in Biotechnology* **20**(1), pp. 9–12 (2002).
- [151] Kathryn L. Kellar and Marie A. Iannone, “Multiplexed microsphere-based flow cytometric assays”, *Exp. Hematol.* **30**, pp. 1227–1237 (2002).
- [152] F. X. Zhou, J. Bonin, and P. F. Predki, “Development of functional protein microarrays for drug discovery: Progress and challenges”, *Combinatorial Chemistry and High Throughput Screening* **7**(6), pp. 539–546 (2004).

- [153] David Holmes, Joseph K. She, Peter L. Roach, and Hywel Morgan, “Bead-based immunoassays using a micro-chip flow cytometer”, *Lab on a CHip* **7**(8), pp. 1048–1056 (2007).
- [154] John P. Nolan and Francis Mandy, “Multiplexed and microparticle-based analyses: Quantitative tools for the large-scale analysis of biological systems”, *Cytometry Part A* **69A**(5), pp. 318–325 (2006).
- [155] V.V. Krishhan, I.H. Khan, and P.A. Luciw, “Multiplexed microbead immunoassays by flow cytometry for molecular profiling: Basic concepts and proteomics applications”, *Crit. Rev. Biotechnol.* **20**, pp. 29–43 (2009).
- [156] Hsin-Yun Hsu, Thomas O. Joos, and Hisashi Koga, “Multiplex microsphere-based flow cytometric platforms for protein analysis and their application in clinical proteomics – from assays to results”, *Electrophoresis* **30**(23), pp. 4008–4019 (2009).
- [157] M. Nolte and A. Fery, “Coupling of individual polyelectrolyte capsules onto patterned substrates”, *Langmuir* **20**, pp. 2995–2998 (2004).
- [158] V. Sivagnanam, A. Sayah, C. Vandevyver, and M. A. M. Gijs, “Micropatterning of protein-functionalized magnetic beads on glass using electrostatic self-assembly”, *Sensors and Actuators B: Chemical* **132**(2), pp. 361–367 (2008).
- [159] Y. Moser, T. Lehnert, and M. A. M. Gijs, “On-chip immuno-agglutination assay with analyte capture by dynamic manipulation of superparamagnetic beads”, *Lab on a CHip* **9**(22), pp. 3261–3267 (2009).
- [160] P. Stevens and D. Kelso, “Imaging and analysis of immobilized particle arrays”, *Analytical Chem.* **75**, pp. 1147–1154 (2003).
- [161] P. Stevens, C. Wang, and D. Kelso, “Immobilized particle arrays: Coalescence of planar- and suspension array technologies”, *Analytical Chem.* **75**, pp. 1141–1146 (2003).
- [162] Cheuk W. Kan, Andrew J. Rivnak, Todd G. Campbell, Tomasz Piech, David M. Rissin, Matthias Mosl, Andrej Peterca, Hans-Peter Niederberger, Kaitlin A. Minnehan, Purvish P. Patel, Evan P. Ferrell, Raymond E. Meyer, Lei Chang, David H. Wilson, David R. Fournier, and David C. Duffy, “Isolation and detection of single molecules on paramagnetic beads using sequential fluid flows in microfabricated polymer array assemblies”, *Lab on a CHip* **12**(5), pp. 977–985 (2012).



- [163] W. Hampton Henley, P. Dennis, and J. Michael Ramsey, “Fabrication of microfluidic devices containing patterned microwell arrays”, *Analytical Chemistry* **84**, pp. 1776–1780 (2012).
- [164] Dino Di Carlo and Luke P. Lee, “Dynamic single-cell analysis for quantitative biology”, *Analytical Chemistry* **78**(23), pp. 7918–7925 (2006).
- [165] D. Di Carlo, Y. Wu, and L. Lee, “Dynamic single cell culture array”, *Lab on a CHip* **6**, pp. 1445–1449 (2006).
- [166] Shannon L. Faley, Mhairi Copland, Donald Wlodkowic, Walter Kolch, Kevin T. Seale, John P. Wikswo, and Jonathan M. Cooper, “Microfluidic single cell arrays to interrogate signalling dynamics of individual, patient-derived hematopoietic stem cells”, *Lab Chip* **9**, pp. 2659–2664 (2009).
- [167] Donald Wlodkowic, Shannon Faley, Joanna Skommer, Dagmara McGuinness, and Jonathan M Cooper, “Biological implications of polymeric microdevices for live cell assays”, *Analytical Chemistry* **81**(23), pp. 9828–9833 (2009).
- [168] Donald Wlodkowic, Joanna Skommer, Dagmara McGuinness, Shannon Faley, Walter Kolch, Zbigniew Darzynkiewicz, and Jonathan M. Cooper, “Chip-based dynamic real-time quantification of drug-induced cytotoxicity in human tumor cells”, *Analytical Chemistry* **81**(16), pp. 6952–6959 (2009).
- [169] Donald Wlodkowic, Shannon Faley, Michele Zagnoni, John P. Wikswo, and Jonathan M. Cooper, “Microfluidic single-cell array cytometry for the analysis of tumor apoptosis”, *Analytical Chemistry* **81**(13), pp. 5517–5523 (2009).
- [170] Donald Wlodkowic, Joanna Skommer, and Zbigniew Darzynkiewicz, “Cytometry in cell necrobiology revisited. recent advances and new vistas”, *Cytometry Part A* **77A**(7), pp. 591–606 (2010).
- [171] D. Wlodkowic, K. Khoshmanesh, J. Sharpe, Z. Darzynkiewicz, and J. Cooper, “Apoptosis goes on a chip: advances in the microfluidic analysis of programmed cell death”, *Analytical Chemistry* **2011**(6439-6446) (2011).
- [172] A. Huebner, D. Bratton, G. Whyte, M. Yang, A. deMello, C. Abell, and F. Hofflfelder, “Static microdroplet arrays: a microfluidic device for droplet trapping, incubation and release for enzymatic cell-based assays”, *Lab on a CHip* **9**(692-698) (2009).

- [173] X. Xu, P. Sarder, Z. Li, and A. Nehorai, “Finite element simulations of hydrodynamic trapping in microfluidic particle-trap array systems”, *Biomicrofluidics* **7**, pp. 054108 (2013).
- [174] X. Xu, P. Sarder, Z. Li, and A. Nehorai, “Optimization of microfluidic microsphere-trap arrays”, *Biomicrofluidics* **7**, pp. 014112 (2013).
- [175] K. Barbee and X. Huang, “Magnetic assembly of high-density dna arrays for genomic analysis”, *Analytical Chemistry* **80**, pp. 2149–2154 (2008).
- [176] Kristopher D. Barbee, Alexander P. Hsiao, Michael J. Heller, and Xiaohua Huang, “Electric field directed assembly of high-density microbead arrays”, *Lab on a CHip* **9**(22), pp. 3268–3274 (2009).
- [177] Kristopher D. Barbee, Alexander P. Hsiao, Eric E. Roller, and Xiaohua Huang, “Multiplexed protein detection using antibody-conjugated microbead arrays in a microfabricated electrophoretic device”, *Lab on a CHip* **10**(22), pp. 3084–3093 (2010).
- [178] Adrian Goodey, John J. Lavigne, Steve M. Savoy, Marc D. Rodriguez, Theodore Curey, Andrew Tsao, Glen Simmons, John Wright, Seung-Jin Yoo, Youngsoo Sohn, Eric V. Anslyn, Jason B. Shear, Dean P. Neikirk, and John T. McDevitt, “Development of multianalyte sensor arrays composed of chemically derivatized polymeric microspheres localized in micromachined cavities”, *Journal of the American Chemical Society* **123**(11), pp. 2559–2570 (2001).
- [179] Nick Christodoulides, Maiyen Tran, Pierre N. Floriano, Marc Rodriguez, Adrian Goodey, Mehnaaz Ali, Dean Neikirk, and John T. McDevitt, “A microchip-based multianalyte assay system for the assessment of cardiac risk”, *Analytical Chemistry* **74**(13), pp. 3030–3036 (2002).
- [180] Mehnaaz F. Ali, Romy Kirby, Adrian P. Goodey, Marc D. Rodriguez, Andrew D. Ellington, Dean P. Neikirk, and John T. McDevitt, “Dna hybridization and discrimination of single-nucleotide mismatches using chip-based microbead arrays”, *Analytical Chemistry* **75**(18), pp. 4732–4739 (2003).
- [181] Romy Kirby, Eun Jeong Cho, Brian Gehrke, Travis Bayer, Yoon Sok Park, Dean P. Neikirk, John T. McDevitt, and Andrew D. Ellington, “Aptamer-based sensor arrays for the detection and quantitation of proteins”, *Analytical Chemistry* **76**(14), pp. 4066–4075 (2004).

- [182] Nicolaos Christodoulides, Sanghamitra Mohanty, Craig S. Miller, M. Chris Langub, Pierre N. Floriano, Priya Dharshan, Mehnaaz F. Ali, Bruce Bernard, Dwight Romanovicz, Eric Anslyn, Philip C. Fox, and John T. McDevitt, “Application of microchip assay system for the measurement of c-reactive protein in human saliva”, *Lab on a Chip* **5**(3), pp. 261–269 (2005).
- [183] Shifeng Li, Pierre N. Floriano, Nicolaos Christodoulides, David Y. Fozdar, Dongbing Shao, Mehnaaz F. Ali, Priya Dharshan, Sanghamitra Mohanty, Dean Neikirk, John T. McDevitt, and Shaochen Chen, “Disposable polydimethylsiloxane/silicon hybrid chips for protein detection”, *Biosensors and Bioelectronics* **21**(4), pp. 574–580 (2005).
- [184] Young-Soo Sohn, Adrian Goodey, Eric V. Anslyn, John T. McDevitt, Jason B. Shear, and Dean P. Neikirk, “A microbead array chemical sensor using capillary-based sample introduction: toward the development of an “electronic tongue””, *Biosensors and Bioelectronics* **21**(2), pp. 303–312 (2005).
- [185] Jesse V. Jokerst, Archana Raamanathan, Nicolaos Christodoulides, Pierre N. Floriano, Amanda A. Pollard, Glennon W. Simmons, Jorge Wong, Carole Gage, Wieslaw B. Furmaga, Spencer W. Redding, and John T. McDevitt, “Nano-bio-chips for high performance multiplexed protein detection: Determinations of cancer biomarkers in serum and saliva using quantum dot bioconjugate labels”, *Biosensors and Bioelectronics* **24**(12), pp. 3622–3629 (2009).
- [186] Jesse V. Jokerst, James W. Jacobson, Bryon D. Bhagwandin, Pierre N. Floriano, Nicolaos Christodoulides, and John T. McDevitt, “Programmable nano-bio-chip sensors: Analytical meets clinical”, *Analytical Chemistry* **82**(5), pp. 1571–1579 (2010).
- [187] Nan Du, Jie Chou, Eliona Kulla, Pierre N. Floriano, Nicolaos Christodoulides, and John T. McDevitt, “A disposable bio-nano-chip using agarose beads for high performance immunoassays”, *Biosensors and Bioelectronics* **28**(1), pp. 251–256 (2011).
- [188] W. Xu, K. Sur, H. Zeng, A. Feinerman, D. Kelso, and J. Ketterson, “A microfluidic approach to assembling ordered microsphere arrays”, *Journal of Micromechanics and Microengineering* **18**, pp. 075027 (2008).
- [189] X. Chen, S. Shojaei-Zadeh, M.L. Gilchrist, and C. Maldarelli, “A lipobead microarray assembled by particle entrapment in a microfluidic obstacle course and used for the display of cell membrane receptors”, *Lab on a Chip* **13**, pp. 3041–3060 (2013).

- [190] B.K. Lok, Y.L. Cheng, and C.R. Robertson, “Protein adsorption on cross-linked polydimethylsiloxane using total internal-reflection fluorescence”, *Journal of Colloid and Interface Science* **9**, pp. 104–116 (1983).
- [191] Andrea Lionello, Jacques Josserand, Henrik Jensen, and Hubert H. Girault, “Dynamic protein adsorption in microchannels by stop-flow and continuous flow”, *Lab on a Chip* **5**, pp. 1096–1103 (2005).
- [192] Martin Zimmermann, Emmanuel Delamarche, Marc Wolf, and Patrick Hunziker, “Modeling and optimization of high-sensitivity, low-volume microfluidic-based surface immunoassays”, *Biomedical Microdevices* **7**(2), pp. 99–110 (2005).
- [193] Konstantin Lebedev, Salvador Mafe, and Pieter Stroeve, “Convection, diffusion and reaction in a surface-based biosensor: Modeling of cooperativity and binding site competition on the surface and in the hydrogel”, *Journal of Colloid and Interface Science* **296**(2), pp. 527–537 (2006).
- [194] T. Gervais and K. Jensen, “Mass transport and surface reactions in microfluidic systems”, *Chemical Engineering Science* **61**, pp. 1102–1121 (2006).
- [195] Guoqing Hu, Yali Gao, and Dongqing Li, “Modeling micropatterned antigen-antibody binding kinetics in a microfluidic chip”, *Biosensors and Bioelectronics* **22**(7), pp. 1403–1409 (2007).
- [196] H. Parsa, C. Chin, P. Mongkolwisetwara, B. Lee, J. Wang, and S. Sia, “Effect of volume- and time-based constraints on capture of analytes in microfluidic heterogeneous immunoassays”, *Lab on a Chip* **8**, pp. 2062–2070 (2008).
- [197] Hana Sipova, David Vrba, and Jiri Homola, “Analytical value of detecting an individual molecular binding event: The case of the surface plasmon resonance biosensor”, *Analytical Chemistry* **84**(1), pp. 30–33 (2011).
- [198] Kapil Subramaniam and Suman Chakraborty, “A semi-analytical model for species transport in combined electroosmotic and pressure driven microflows with surface adsorption–desorption reactions”, *Microfluidics and Nanofluidics* **10**(4), pp. 821–829 (2011).
- [199] Rasmus Hansen, Henrik Bruus, Thomas H. Callisen, and Ole Hassager, “Transient convection, diffusion, and adsorption in surface-based biosensors”, *Langmuir* **28**(19), pp. 7557–7563 (2012).

- [200] Jason A. Thompson and Haim H. Bau, “Microfluidic, bead-based assay: Theory and experiments”, *Journal of Chromatography B* **878**(2), pp. 228 – 236 (2010).
- [201] X. Jin, J. Talbot, and L. N.-H. Wang, “Analysis of steric hindrance effects on adsorption kinetics and equilibria”, *AIChE Journal* **40**, pp. 1685–1696 (1994).
- [202] W.M. Deen, *Analysis of Transport Phenomena*, Oxford University Press New York 2nd edition (2012).
- [203] R. W. Glaser, “Antigen-antibody binding and mass transport by convection and diffusion to a surface: A two-dimensional computer model of binding and dissociation kinetics”, *Analytical Biochemistry* **213**(1), pp. 152–161 (1993).
- [204] Peter Schuck and Allen P. Minton, “Analysis of mass transport-limited binding kinetics in evanescent wave biosensors”, *Analytical Biochemistry* **240**(2), pp. 262–272 (1996).
- [205] M.L. Yarmush, D.B. Patankar, and D.M. Yarmush, “An analysis of transport resistances in the operation of biacore(tm): Implications for kinetic studies of biospecific interactions”, *Molecular Immunology* **33**, pp. 1203–1214 (1996).
- [206] Lars L. H. Christensen, “Theoretical analysis of protein concentration determination using biosensor technology under conditions of partial mass transport limitation”, *Analytical Biochemistry* **249**(2), pp. 153–164 (1997).
- [207] D. Myszka, T. Morton, M. Doyle, and I. Chaiken, “Kinetic analysis of a protein antigen-antibody interaction limited by mass transport on an optical biosensor”, *Biophys Chem* **64**, pp. 127–137 (1997).
- [208] D. Myszka, X. He, M. Dembo, T. Morton, and B. Goldstein, “Extending the range of rate constants available from biacore: Interpreting mass transport-influenced binding data”, *Biophysical Journal* **75**, pp. 583–594 (1998).
- [209] T. Mason, A. Pineda, C. Wofsy, and B. Goldstein, “Effective rate models for the analysis of transport-dependent biosensor data”, *Mathematical Biosciences* **159**, pp. 123–144 (1999).
- [210] Byron Goldstein, Daniel Coombs, Xiaoyi He, Angel R. Pineda, and Carla Wofsy, “The influence of transport on the kinetics of binding to surface receptors: application to cells and biacore”, *Journal of Molecular Recognition* **12**(5), pp. 293–299 (1999).

- [211] C. Wofsy and B. Goldstein, “Effective rate models for receptors distributed in a layer above a surface: Applications to cells and biacore”, *Biophysical Journal* **82**, pp. 1743–1755 (2002).
- [212] F. Rusminin, Z. Zhong, and J. Feijen, “Protein immobilization strategies for biochips”, *Biomacromolecules* **8**, pp. 1775–1789 (2007).
- [213] D. Kim and A. Herr, “Protein immobilization techniques for microfluidic assays”, *Biomicrofluidics* **7**, pp. 041501 (2013).
- [214] Kevin L. Prime and George M. Whitesides, “Adsorption of proteins onto surfaces containing end-attached oligo(ethylene oxide): a model system using self-assembled monolayers”, *Journal of the American Chemical Society* **115**(23), pp. 10714–10721 (1993).
- [215] S. Lee and P. Laibinis, “Protein resistant coatings for glass and metal oxide surfaces derived from oligo(ethylene glycol)- terminated alkyltrichlorosilanes”, *Biomaterials* **19**, pp. 1669–1675 (1998).
- [216] H.A. Stone, A.D. Stroock, and A. Ajdari, “Engineering flows in small devices”, *Annual Review of Fluid Mechanics* **36**(1), pp. 381–411 (2004).
- [217] Todd M. Squires and Stephen R. Quake, “Microfluidics: Fluid physics at the nanoliter scale”, *Reviews of Modern Physics* **77**(3), pp. 977–1026 (2005).
- [218] Shia-Yen Teh, Robert Lin, Lung-Hsin Hung, and Abraham P. Lee, “Droplet microfluidics”, *Lab on a Chip* **8**(2), pp. 198–220 (2008).
- [219] N.G. Green and H. Morgan, “Separation of submicrometers particles using a combination of dielectrophoretic and electrodynamic forces”, *J. Phys. D. Apply. Phys.* **31**, pp. 25–30 (1998).
- [220] R. Pethig, “Review article - dielectrophoresis: Status of the the theory, technology and applications”, *Biomicrofluidics* **4**, pp. 022811 (2010).
- [221] L.C. Waterman, “Electrocoalescers”, *Chemical Engineering Progress* **61**, pp. 51–57 (1965).
- [222] C.P. Galvin, “Design principles for electrocoalescers”, *ICHEME Symp. Ser.* **88**, pp. 101–113 (1986).

- [223] T.Y. Chen, R.A. Mohammed, A.I. Bailey, P.F. Luckham, and S.E. Taylor, “Dewatering of crude oil emulsions. 4. emulsion resolution by the application of an electric field”, *Colloids and Surfaces A -Physicochemical and Engineering Aspects* **83**, pp. 273–284 (1994).
- [224] J.S. Eow, M. Ghadiri, A.O. Sharif, and T. Williams, “Electrostatic enhancement of coalescence of water droplets in oil: A review of the current understanding”, *Chemical Engineering Journal* **84**, pp. 173–192 (2001).
- [225] J.S. Eow and M. Ghadiri, “Electrostatic enhancement of coalescence of water droplets in oil: a review of the technology”, *Chemical Engineering Journal* **85**, pp. 357–368 (2002).
- [226] M. Chiesa, J.A. Melheim, A. Pedersen, S. Ingebrigtsen, and G. Berg, “Forces acting on water droplets falling in oil under the influence of an electric field: numerical predictions versus experimental observations”, *Eur. J. Mech. B-Fluids* **24**, pp. 717–732 (2006).
- [227] M. Chiesa, J. Melheim, A. Pedersen, S. Ingebrigtsen, and G. Berg, “Forces acting on water droplets falling in oil under the influence of an electric field: Numerical predictions versus experimental observations”, *European Journal of Mechanics B/Fluids* **24**, pp. 717–732 (2005).
- [228] M. Chiesa, S. Ingebrigtsen, J.A. Melheim, P.V. Hemmingsen, E.B. Hansen, and O. Hestad, “Investigation of the role of viscosity on electrocoalescence of water droplets in oil”, *Sep. Purif. Technol.* **50**, pp. 267–277 (2006).
- [229] P. Atten, L. Lundgaard, and G. Berg, “A simplified model of electrocoalescence of two close water droplets in oil”, *Journal of Electrostatics* **64**, pp. 550–554 (2006).
- [230] L. Lundgaard, G. Berg, S. Ingebrigtsen, and P. Atten, *Electrocoalescence for Oil-Water Separation: Fundamental Aspects*, pp. 549–592, Taylor and Francis (2006).
- [231] Abdou R. Thiam, Nicolas Bremond, and Jerome Bibette, “Breaking of an emulsion under an ac electric field”, *Physical Review Letters* **102**(18), pp. 188304 (2009).
- [232] Piotr Garstecki, Irina Gitlin, Willow DiLuzio, George M. Whitesides, Eugenia Kumacheva, and Howard A. Stone, “Formation of monodisperse bubbles in a microfluidic flow-focusing device”, *Applied Physics Letters* **85**(13), pp. 2649–2651 (2004).
- [233] S. L. Anna and H. C. Mayer, “Microscale tipstreaming in a microfluidic flow focusing device”, *Physics of Fluids* **18**, pp. 12 (2006).